PERMEABILITY, CLAY MINERALOGY, AND MICROFABRIC OF FINE-GRAINED SEDIMENTS FROM THE NANKAI TROUGH AND SHIKOKU BASIN, OFFSHORE SOUTHWEST JAPAN

-

A Thesis

presented to

the Faculty of Graduate School

at the University of Missouri-Columbia

-

In Partial Fulfillment

of the Requirements for the Degree

Master of Science

-

by

MEHMET KORAY EKINCI

Dr. Michael B. Underwood, Thesis Supervisor

MAY 2012

The undersigned, appointed by the Dean of the Graduate School, have examined the thesis entitled

PERMEABILITY, CLAY MINERALOGY, AND MICROFABRIC OF FINE-GRAINED SEDIMENTS FROM THE NANKAI TROUGH AND SHIKOKU BASIN, OFFSHORE SOUTHWEST JAPAN

Presented by Mehmet Koray Ekinci

a candidate for the degree of Master of Geological Science

and hereby certify that in their opinion it is worthy of acceptance.

-

Professor Michael B. Underwood

-

Professor William J. Likos

-

Professor Martin Appold

ACKNOWLEDGMENTS

The study was supported by Turkish Petroleum Corporation (scholarship to M.K. Ekinci), the National Science Foundation (grant OCE-0751819 to Underwood and Likos), and the Consortium for Ocean Leadership (grants T315A58, T315B58, and T315C58 to Underwood and Likos). Samples were provided by the Integrated Ocean Drilling Program (IODP). I thank the crew, technicians, and shipboard scientists aboard the Chikyu D/V for their assistance in acquisition of samples during IODP Expeditions 314, 315, 316, 322 and 333. Also, I would like to thank all professors and graduate students in Department of Geological Sciences and Department of Civil and Environmental Engineering, especially to my academic advisor Dr. Michael B. Underwood, Dr. William J. Likos, Martin Appold, Savas and Gina Ceylan, Junhua Guo, Brooke Nicholson, Mark Grzovic, Matias Callieri, Tuba Budak, and my family.

TABLE OF CONTENTS

ABSTRACT

The Nankai Trough, a convergent plate boundary between the subducting Philippine Sea plate and overriding Eurasian plate, is located off the coast of southwest Japan. This study covers the central portion of the Kumano transect, eastern province of the Nankai Trough, which consists of six morphotectonic zones, such as, from southeast to northwest, subduction inputs in the Shikoku Basin, trench zone, frontal thrust zone, imbricated thrust zone, megasplay fault zone, and Kumano forearc basin. The objectives of this study are: (1) to show how permeability varies as a function of burial depth, lithostratigraphy, and structural position within the Nankai Trough subduction zone; and (2) to document the permeability anisotropy and consider how it changes with microfabric and mineralogy. Constant-flow permeability tests were executed to measure permeability for vertical (along-core) and horizontal (cross-core) sections of twenty-one core samples collected during Integrated Ocean Drilling Program (IODP) Expeditions 316 and 333. Comparison of the horizontal (k_h) to the vertical (k_v) permeability defines the anisotropy (k_h/k_v). Environmental scanning electron microscopy (ESEM) was used to image the fabric of samples in horizontal and vertical sections. The images were analyzed to compute the standard deviations and the indexes (i) of microfabric orientation. The relative clay mineral percentages in bulk sediment were calculated using previously analyzed X-ray diffraction data.

Samples from megasplay fault zone (IODP Sites C0004 and C0008) came from ~51 to 381 meters below the sea floor (mbsf). The vertical permeability ranges between 1.61E-17 m^2 and 1.86E-18 m^2. Samples from frontal thrust zone (IODP Sites C0006 and C0007), were taken from ~35 to 564 mbsf. The vertical permeability varies from 1.63E-

15 m^2 to 2.68E-19 m^2. The values of horizontal permeability range between 2.11E-15 m^2 and 3.32E-19 m^2. Samples from Shikoku Basin (IODP Site C0011) came from ~36 to 362 mbsf. The values of vertical permeability differ between 1.34E-17 m^2 and 2.83E-19 m^2, whereas the values of horizontal permeability show variations between 1.80E-17 m^2 and 5.15E-19 m^2. The ratio of horizontal to vertical permeability (k_h/k_v) ranges between 0.02 and 19.90. The permeability and porosity values decrease as burial depth increases. However, the permeability doesn't show a statistically significant correlation with porosity. The vertical cut face shows better preferred orientation of grains than microfabric on the horizontal cut, which helps explain the anisotropy of permeability. Ratio of index of microfabric orientation does not show a significant correlation with permeability either direction or the anisotropy value. Vertical permeability values decrease as smectite and total clay minerals increase in abundance. Thus, the permeability and the anisotropy of permeability are not controlled by any single parameter.

LIST OF TABLES

LIST OF ILLUSTRATIONS

LIST OF ILLUSTRATIONS (continued)

Figure Page

LIST OF ILLUSTRATIONS (continued)

Figure Page

LIST OF ILLUSTRATIONS (continued)

Figure Page

1. INTRODUCTION

The greatest seismic activities around the world are observed within subduction zones. These highly active plate boundaries have caused catastrophes with disastrous effects on highly populated coastal areas (Lay et al., 2005). Knowing the architectures and behaviors of such plate boundaries is important for hazard mitigation. The Nankai Trough, offshore southwest Japan (Fig. 1), is a subduction zone between the Philippine Sea (PSP) and Eurasian Plates (Seno, 1977). Great earthquakes, magnitude >8, occur with an average frequency of ~180 years in Nankai Trough (Ando, 1975), and the region has a 1300 year written history of great earthquakes (Ando, 1975; Ichinose et al., 2003; Hori et al., 2004). This area has been selected for multidisciplinary investigation of seismogenic processes because of its history of large earthquakes, well-confined rupture area, and accessibility by ocean drilling (Tobin et al., 2009). The Nankai Trough Seismogenic Zone Experiment (NanTroSEIZE) is a complex drilling project that has been underway for several years, with multiple expedition teams of scientists from all around the world. One of the NanTroSEIZE project's goals is to understand the relations among physical, mechanical, and hydrogeological properties of the accretionary wedge and subducting sediments. Previous drilling within the region included Deep Sea Drilling Project (DSDP) Legs 31, 58 and 87 (Karig et al., 1975; Kagami et al., 1986), Ocean Drilling Project (ODP) Legs 131, 190 and 196 (Taira et al., 1991; Moore et al., 2001; Mikada et al., 2002). The Integrated Ocean Drilling Program (IODP) added NanTroSEIZE Expeditions 314, 315, 316 (Screaton et al., 2009), 322 (Underwood et al., 2010) and 333 (Expedition 333 Scientists, 2011) (Fig. 1).

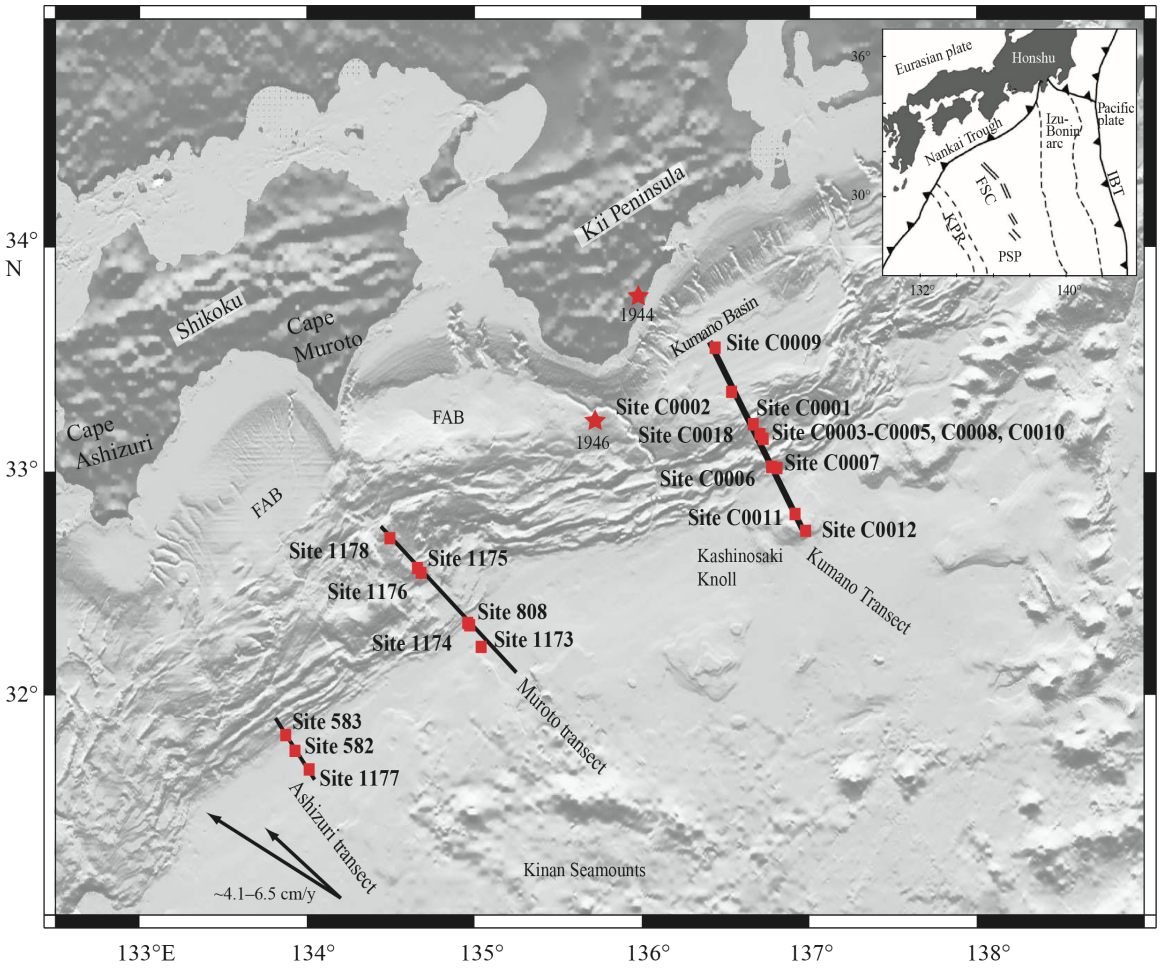

Figure 1. Regional bathymetry of northern Shikoku Basin and Nankai Trough region showing previous DSDP/ODP and IODP drilling transects. FAB = forearc basin. Inset = tectonic map showing plate tectonic setting of the region. IBT = Izu-Bonin Trench, KPR = Kyushu-Palau Ridge, FSC = fossil spreading center, PSP = Philippine Sea plate. Stars = epicenter locations of last two large subduction earthquakes (1944 and 1946) (Karig et al., 1975; Taira et al., 1991; Moore et al., 2001; Screaton et al., 2009; Underwood et al., 2010; Expedition 333 Scientists, 2011).

There are two types of convergent margins: (1) accretionary margins such as Nankai Trough, which are associated with thick sequences of sedimentary rocks that are transferred from the subducting oceanic plate to the overriding plate and (2) erosive margins (Clift and Vannucchi, 2004). Accretion is a result of the transfer of material by frontal offscraping near the trench axis or underplating of the forearc wedge at greater depths (Clift and Vannucchi, 2004). Accretionary wedges behave like a wedge of snow in front of a bulldozer, or shovel. In cross section, the zone of active accretion near the trench involves imbricate thrust faults that build the wedge, above a basal detachment or décollement fault that dips toward the volcanic arc; the seafloor topography slopes toward the toe or deformation front of the wedge (Dahlen, 1990; Morgan and Karig, 1993) (Fig. 2).

Stratigraphic architecture creates three-dimensional variations in permeability and fluid flow through subduction zones (Underwood, 2007; Saffer, 2010). Bulk permeability can have a direct effect on pore pressure within accretionary prisms because of its relation with sediment consolidation (Moore and Vrolijk, 1992; Saffer and Bekins, 2002, 2006). Compaction, tectonic consolidation, and mineral dehydration can result in pore pressure disequilibrum (Saffer and Tobin, 2011). Disequilibrium is driven by geological mechanisms such as tectonic loading and thermal expansion. Such mechanisms regulate fluid escape by altering intrinsic permeability through faulting and deformation (Raleigh et al., 1976; Saffer and Bekins, 2002; Saffer and Tobin, 2011). Fluids produced by dehydration reactions can also outpace fluid escape and thus lead to build up of overpressure.

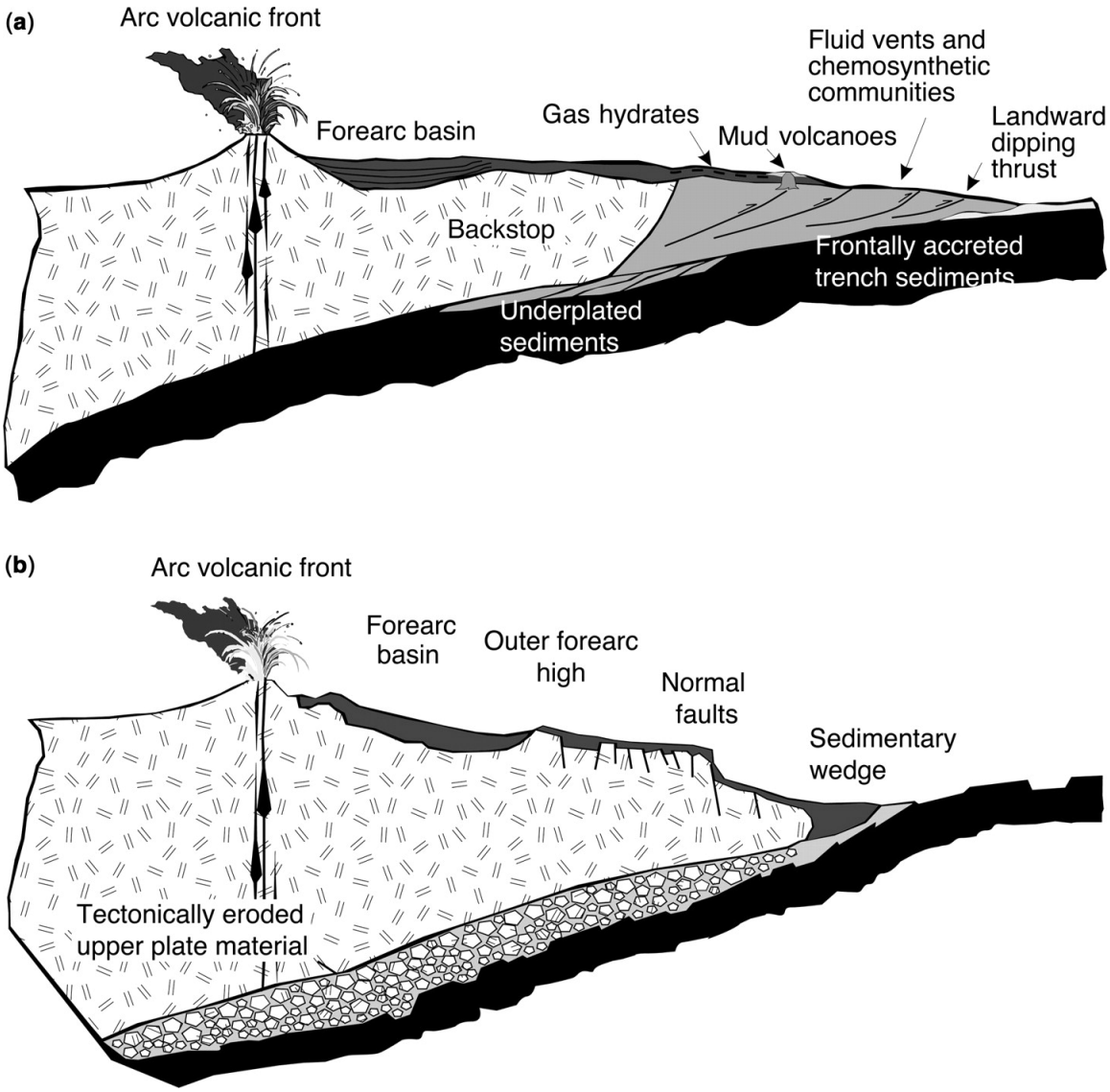

Figure 2. Schematic illustration of the features common to the two basic types of active margin; a) accretionary, and b) erosive margins (Clift and Vannucchi, 2004).

In subduction zones, the higher permeability of fractures, fault zones, and sandy layers drives drainage patterns and flow rates (Moore, 1989; Carson and Screaton, 1998), whereas lower permeability of compacted fine-grained sediments retards the ability of fluids to reach drainage pathways (Neuzil, 1995; Saffer and Bekins, 2002). Saffer and Tobin (2011) describe excess pore pressure as fluid pressure above the hydrostatic value.

The hydrological properties of sediments and sedimentary rocks within subduction zones such as Nankai Trough are tied with many factors inherited from the time of deposition, including grain size and shape, sorting, particle arrangement, the forces between particles, and different scales of fabric elements (Moon and Hurst, 1984; Bennett et al., 1989; Mitchell, 1993). The type and amount of fine-grained particles are particularly influential (Saffer and Bekins, 2002; Underwood, 2007). Hydrological properties are important because they influence the fluid flow, consolidation, and dewatering (Bennett et al., 1989; Neuzil, 1994, 1995; Bolton et al., 1998; Dewhurst et al., 1999; Gamage et al., 2011; Saffer et al., 2011).

Porosity is defined as the fraction of the total volume of material that consists of pore space (Schwartz and Zhang, 2003). A medium can be highly porous but low in permeability. Only if the pore spaces are connected and allow the fluid to pass through can permeability increase. The permeability-porosity relationship for fine-grained siliciclastic sediments can be applied to subduction zones (Gamage et al., 2011). Consolidation of fine-grained sediments controls changes in their particle orientation and pore size distribution as porosity and permeability decrease in response to increasing effective normal stress (Moon and Hurst, 1984; Anandarajah and Kuganenthira, 1995; Aplin et al., 2006). Diagenetic processes, plastic deformation of the solid skeleton, and

mineral dissolution can have profound effects on the porosity; the proportion of solid components changes by conversion to fluids (e.g. smectite dewatering and petroleum generation from solid kerogen) and collapse of the porous structure (Neuzil, 1995).

The microstructure is another property that influences the sediment's physical and mechanical properties and behavior under static and dynamic stresses. Fundamental properties of sediments such as porosity, permeability, and strain-stress behavior are tightly interconnected (Bennett et al., 1977; Bennett et al., 1989; Bennett et al., 1991). Clay fabric is defined as the orientation and arrangement or spatial distribution of the solid particles and the particle-to-particle geometry (e.g., face-to-face, face-to-edge) (Bennett et al., 1991). Microstructure (fabric) of sediments is influenced by mechanisms such as physicochemical flocculation, bioorganic aggregation, and burial diagenesis (Fig. 3) (Bennett et al., 1991). Moon and Hurst (1984) discussed three sedimentation stages of clays during the microfabric development: sedimenting clay; freshly sedimented clay; and compacted clay. The microfabric of sedimenting clay is due to complex electrochemistry of clay particles and their immediate surroundings that result flocculation that is associated with cardhouse structures. Whitehouse et al. (1958) concluded that the flocculation characteristics of sediment depend on its mineralogy. The hemipelagic sediments have greater degree of preferred orientation of clay particles than the turbiditic sediments. Hemipelagic sediments are associated with a slower sedimentation rate in the dispersed state, and turbidites are characterized by rapid deposition. Moon and Hurst (1984) discussed that sediments in organic-rich conditions (e.g., marine environment) have relatively parallel oriented microfabric due to dispersing agents. Moreover, Bennet et al. (1991) discuss that sediment fabric is altered

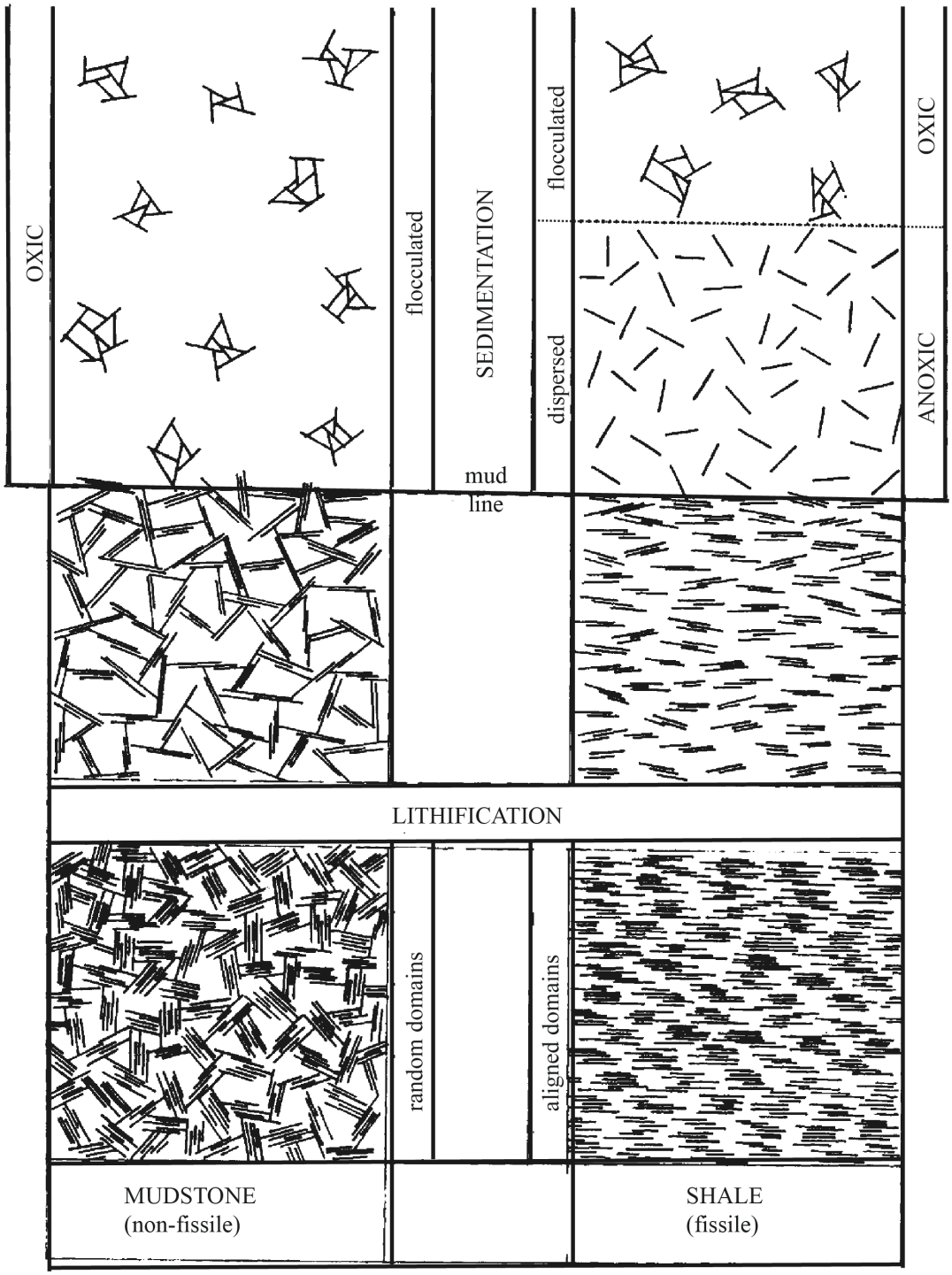

Figure 3. Schema depicting the major microstructural changes in clay sediments (Moon and Hurst, 1984).

mechanically by not only aggregation that takes place in water column, such as ingestion and reorientation of particles as fecal pellets, but also by bioturbation after deposition (burrows, tracks, trails).

Preferred grain orientation at small scales and sedimentary layering at the formation scale cause permeability anisotropy (Anandarajah and Kuganenthira, 1995; Clennel et al., 1999; Bolton et al., 2000; Saffer and Tobin, 2011). Arranging of clay particles normal to an axial load, causes decreasing flow path tortuosity parallel to the particle alignment (Olsen, 1960). Burial loading and chemical diagenesis align platy clay minerals perpendicular to maximum principal effective stress. Permeability becomes more anisotropic as a result of heavily compacted grain fabric because fluids physically follow the easiest flow path, which is usually along rather and across the direction of strongly preferred grain alignment (Sintubin, 1994; Clennel et al., 1999; Dewhurst et al., 1999; Kim et al., 1999).

Aplin et al. (2006) discussed how mechanical compaction and clay mineral diagenesis affect the alignment of phyllosilicates (sheet silicates). They documented mechanical compaction caused decrease in porosity from ~75 to 15%. However, the alignment of phyllosilicates is driven by diagenetic processes, such as the alteration of volcanic glass/ash to smectite, and the illitization of smectite and/or mixed-layered clays (I-S) (Aplin et al., 2006; Spinelli et al., 2007).

Smectite is a hydrated clay mineral that retains variable amounts of water in the interlayer region, and the amount of water retained is a function of temperature, pressure, interlayer cation species, and salinity (Brown and Ransom, 1996). Smectite is often the main component of sediments entering a subduction zone. Vrojlik (1990) suggested that

smectite originates by the alteration of volcanic ash within sediment. Presence of smectite in clay-rich sediments has profound effects on porosity and fluid flow (Gamage et al., 2011) because smectite-rich strata are structurally weak, retain water, and are highly porous (Vrojlik, 1990). The volumetric significance of interlayer water increases with burial (Colten-Bradley, 1987), and with increasing temperature and effective stress, the hydration state changes as smectite is transformed to illite. Dehydration during the smectite-to-illite transition introduces fresh water into the pore system (Kastner et al., 1993; Bekins et al., 1995; Saffer et al., 2008), which can influence pore pressure if drainage cannot keep pace with fluid production.

The focus of this thesis is on the interconnections among permeability, clay mineralogy, and microfabric of sediments from the Nankai Trough and Shikoku Basin, offshore southwest Japan. The objectives are two-fold: 1) to show how permeability varies as a function of burial depth, lithostratigraphy, and structural position within the Nankai Trough subduction zone; 2) to document the permeability anisotropy and consider how it changes with microfabric and mineralogy of fine-grained marine sediments. Multi-direction constant flow permeation was used to measure the values of hydraulic conductivity and intrinsic permeability.

2. GEOLOGICAL SETTINGS

2.1. Nankai Trough

The Nankai Trough is the convergent plate boundary between the subducting Philippine Sea plate (PSP) and overriding Eurasian plate. It extends 700 km from the Suruga Trough, which marks a collision zone between the Izu-Bonin island arc and the Honshu arc, to the northern tip of the Kyushu-Palau Ridge. Investigations of the Nankai Trough have consisted of drilling and coring several boreholes penetrating the incoming sediment section and accretionary prism along three transects: (west to east) Ashizuri Transect offshore Cape Ashizuri, Muroto Transect offshore Cape Muroto and Kumano Transect off Kii Peninsula (Fig. 1; Fig. 4).

This study covers the central portion of the Kumano transect, which has been probed during NanTroSEIZE Stages 1 and 2 (Screaton et al., 2009; Underwood et al., 2010; Expedition 333 Scientists, 2011). The accretionary prism in the Kumano transect has been divided into six morphotectonic zones, which are, from southeast to northwest, trench zone, frontal thrust zone (FTZ), imbricated thrust zone (ITZ), megasplay fault zone (MSFZ), Kumano Basin edge fault zone (KBEFZ), and the Kumano forearc basin (Fig. 5) (Moore et al., 2009).

In the trench zone, younger trench deposits overlie the igneous oceanic crust and Shikoku Basin facies. There is a well developed protothrust zone (PTZ), which is blanketed by a slice of trench strata previously accreted into the prism. A trench-fill turbidite unit dominates the upper part of this zone. The lower part is characterized by hemipelagic mud interval that thickens by ductile deformation (Kagami, 1986). The frontal thrust zone is

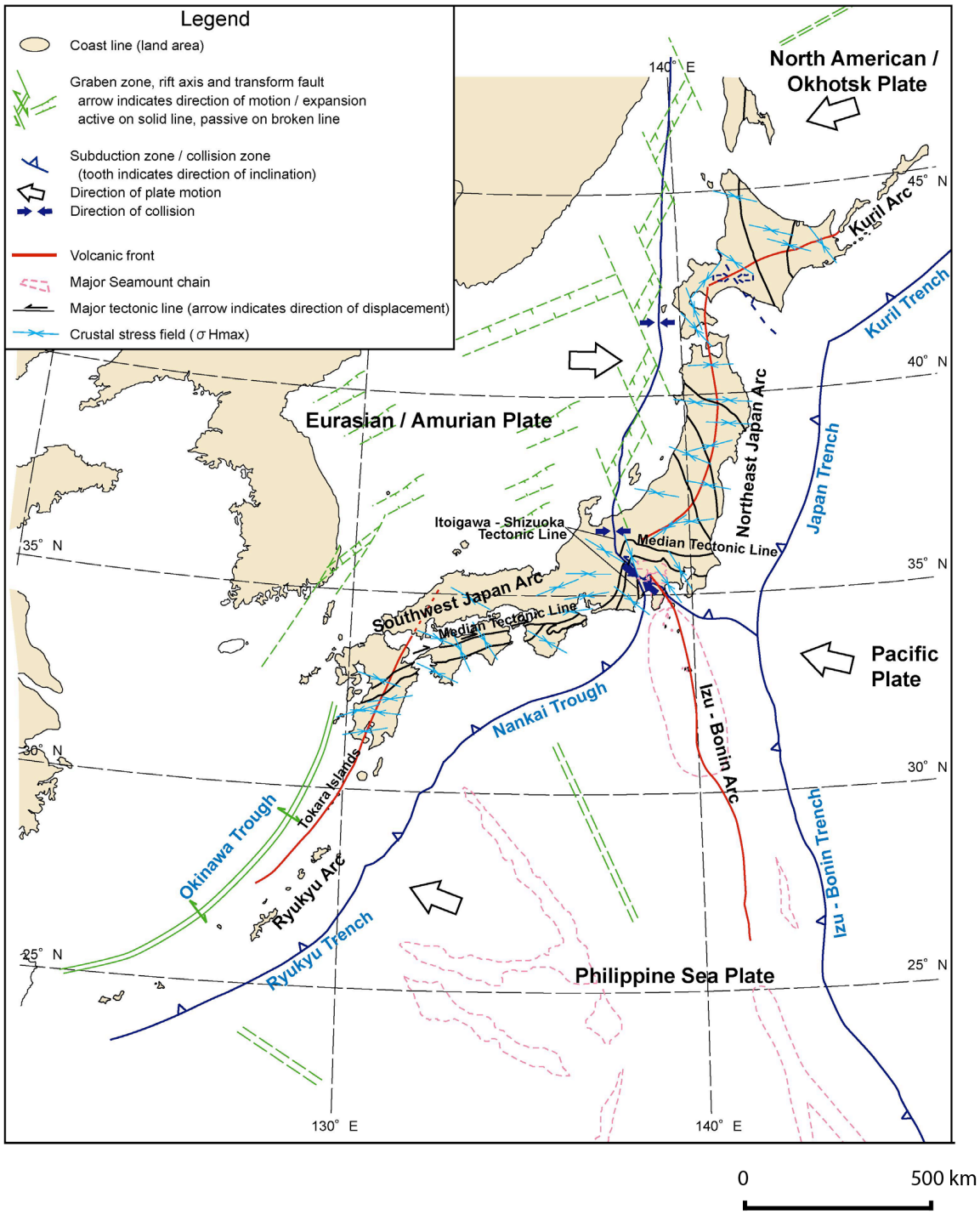

Figure 4. Current tectonic situation of Japan and key tectonic features (Seno, 1993).

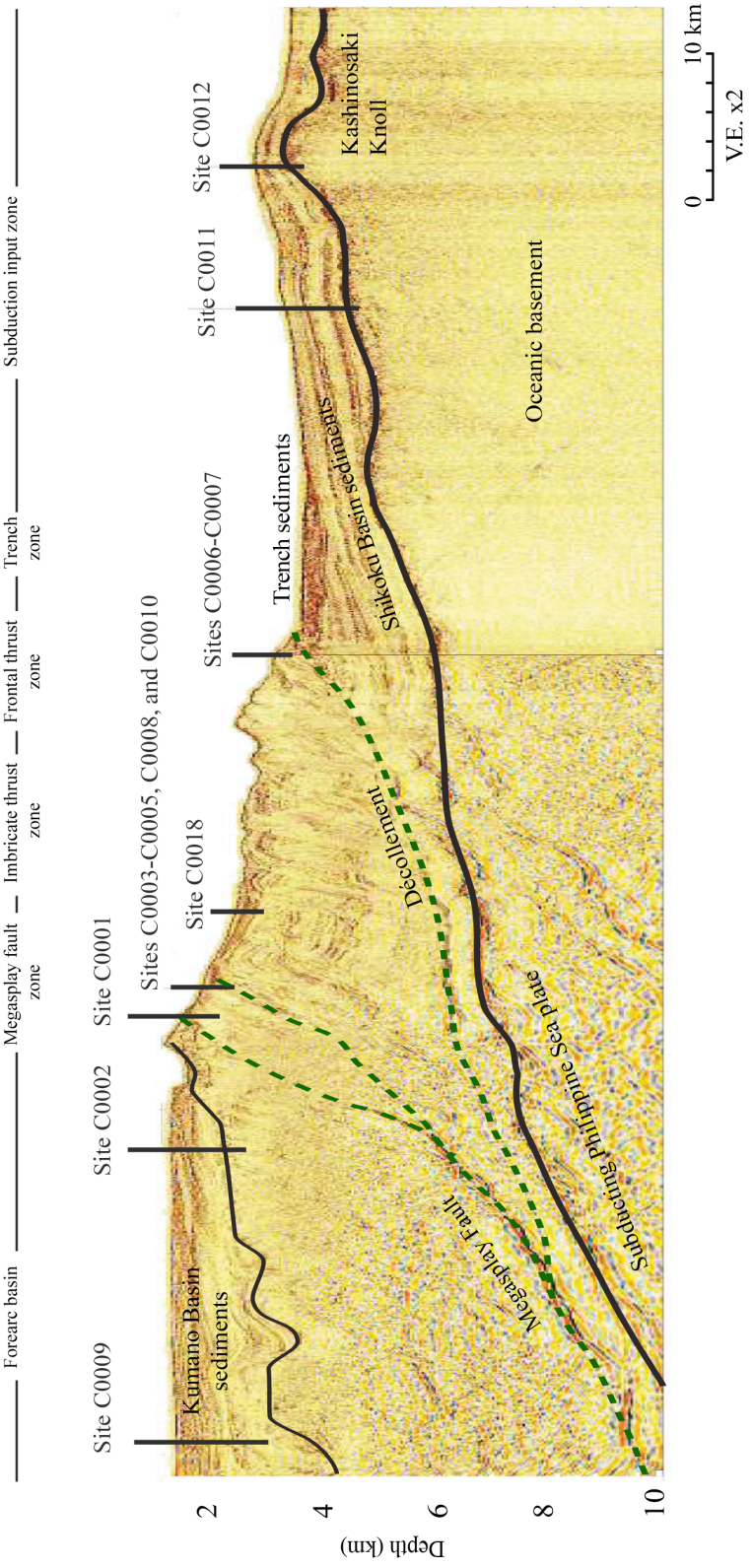

Figure 5. Seismic profile of Kumano Transect, offshore southwest Japan with drilling sites IODP Expeditions 314/315/316, 322,and 333 (Expedition 333 Scientists, 2011).

highly complex with a very steep slope at the seaward edge of the prism (Moore et al., 2009). Landward of the trench is the imbricated thrust zone, a series of thrust packages made up of a thick highly reflective sequence that are probably accreted trench sediments (Moore et al., 2009). Slope sediments that are increasingly deformed with burial depth overlie it. The megasplay fault zone or out-of-sequence-thrust, beneath the trench upper slope and Kumano Basin, is defined by a splay fault system (Park et al., 2002). The shallow part of the MSFZ is a complex thrust system with backward breaking branches that truncate the imbricate thrust faults within the accretionary prism and override younger slope basin sediments (Moore et al., 2009; Stresser et al., 2009). The KBEFZ is comprised by combination of normal and strike-slip faults between the Kumano forearc basin and the MSFZ (Martin et al., 2010). More than 2 km of sediment is imaged in the Kumano forearc basin.

2.2. Shikoku Basin

The PSP subducts beneath the Eurasian plate at a rate that varies along the Nankai Trough, from ~5cm/year at N52ºW in the west to ~ 4 cm/year at N48ºW in the east (Seno, 1977; Seno et al., 1993). Changes in volcanic activity in western Japan show that the subduction either stopped or was very slow (<1 cm/year) during 4-12 Ma, and increased to about 4-5 cm/year since about 4 Ma (Taira, 2001; Kimura et al., 2008). The subducting lithosphere of the Shikoku Basin was formed by backarc spreading at 15-25 Ma, and the current phase of subduction initiated ~6 Ma. Analysis of magnetic anomalies suggests multiple episodes of Shikoku Basin spreading during the late Oligocene to middle Miocene (Kobayashi and Nakada, 1978; Shih, 1980). The history of the opening is mainly divided into two episodes: east-west spreading during 27-19 Ma; and north-

south spreading during 14-12 Ma (Chamot-Rooke et al., 1987). Kobayashi and Nakada (1978) pointed out that the basement structure of the Shikoku Basin was formed by the complex back-arc spreading history in the Izu-Bonin Island Arc. The basement relief in the Shikoku Basin averages approximately 600 meters (Chamot-Rooke et al., 1987).

Northern Shikoku Basin has been divided into three provinces based on its basement relief and associated sediment cover (Fig. 6) (Ike et al., 2008). The Eastern Province of the Shikoku Basin is characterized by relatively rough basement relief, both lineated and isolated, associated with Kashinosaki Knoll (basement amplitude <1500 m) and another unnamed topographic highs (<600 m). The half-wavelength of the basement highs, parallel to the trench, ranges from about 10 to 20 km. The basement highs are generally about one half to one third as wide as the intervening basement lows. The Central Province has approximately 10-20 km wide, NW-trending basement lows that are about 1-2 km deeper than adjacent horst blocks along the Kinan Seamount Chain (Fig. 6). Le Pichon et al. (1987) and Ike et al. (2008) suggested that the formation of large basement relief in the Central Province may be related to the major change in seafloor spreading to NE-SW, accompanied by a decrease in spreading rate, and young seamount eruption. The basement lows in Central Province have 3-5 times greater relief than those in the Western Province, which is characterized by relatively smooth basement relief (<200-400 m) associated with a few isolated basement highs. The basement relief that is the smoothest is about 170 m perpendicular to the trench and 200-400 m parallel to the trench. The trench perpendicular basement relief on the Western Province has lower amplitude than the Eastern Province. The basement relief in the Eastern Province is less than 600 m, midway in between Western and Central Province (Fig. 6).

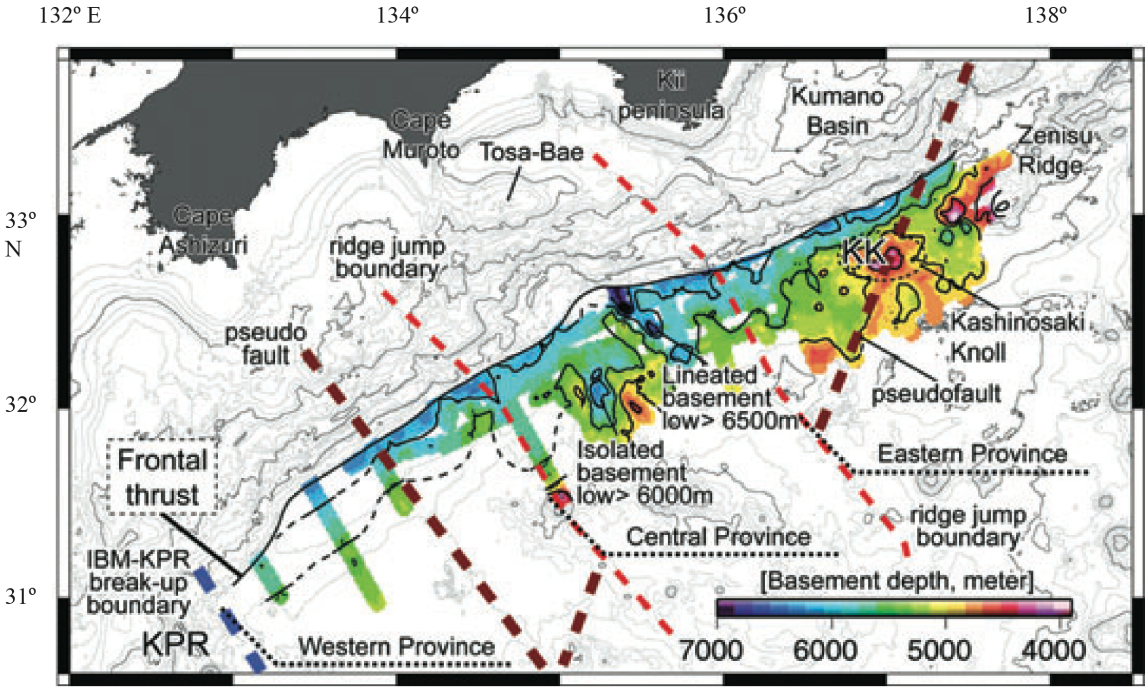

Figure 6. Basement depth contour map along the northern Shikoku Basin. Solid lines are thickness contours at 500 m intervals, Dashed lines indicated boundaries of Magnetic Zones. IBM-KPR break-up boundaries; ridge jump boundaries. Regional basement/sediment provinces are also shown (Ike et al., 2008).

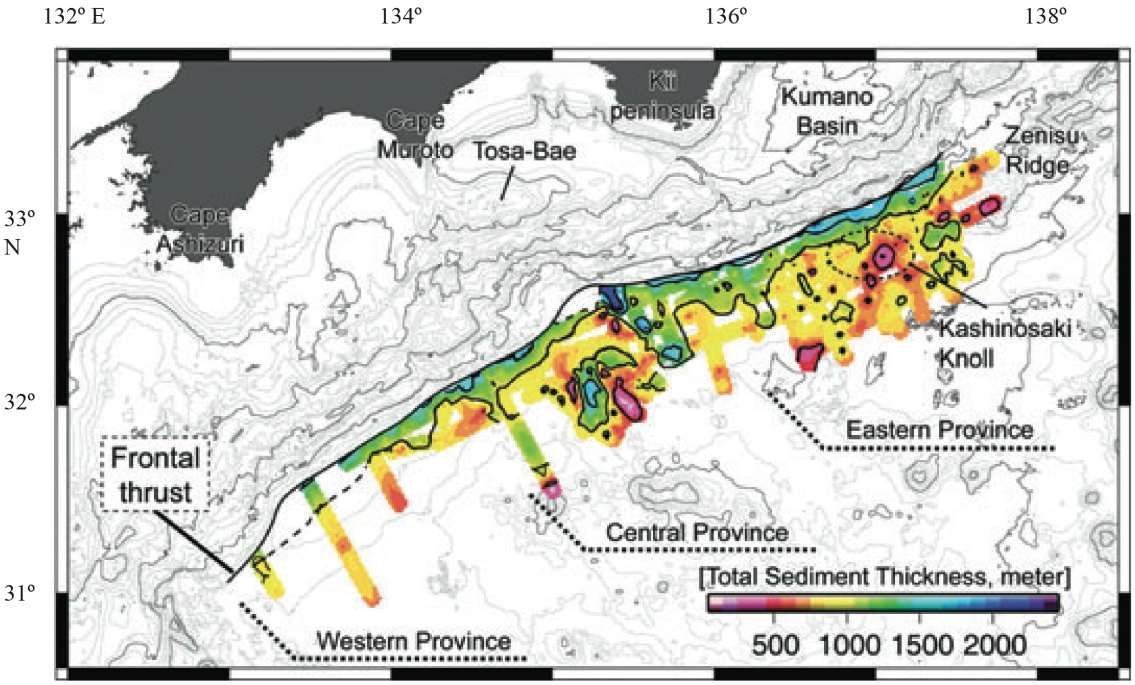

Figure 7. Total sediment isopach map along the northern Shikoku Basin (Ike et al. 2008).

The maximum total sediment thickness seaward of the deformation front is approximately 2000-2200 m in the central Shikoku Basin, whereas the minimum thickness is less than 300 m over the topographic highs, such as the Kashinosaki Knoll and the Kinan Seamount Chain (Fig. 7) (Ike et al., 2008; Expedition 322 Scientists, 2010a, b). The total sediment thickness generally increases toward the trench and the Izu-Bonin arc (Ludwig and Houtz, 1979; Nemoto, 1995; Ike et al., 2008). The sediment thickness ranges mostly between 500 and 750 m in the Western Province, in the basement lows seaward of the Nankai Trough. In the Central and Eastern Provinces, the sediment thickness exceeds 1000 m in the basement lows seaward of Nankai Trough (Fig. 7) (Ike et al., 2008). Also, the prism architecture varies remarkably along-strike, from Ashizuri transect (Western Province) to Muroto transect (Central Province) to Kumano transect (Eastern Province) (Fig. 8) (Saffer, 2010, Moore et al., 2009).

2.3. Sedimentation

Deep-marine sedimentation is generally considered in two main groups, such as pelagic sediments and turbidites. Pelagic sediments, which are deposited from suspension, include biogenic debris, clay and silt, volcanic ash, eolian dust, ice-rafted sediments, and extra-terrestrial dust. Hemipelagic sediments are those in which >25% of the >5 μm size fraction is detrital, volcanic, and/or neritic. Turbidites, which are deposited by bottom-flowing density currents, are generally detrital (land derived). They display features such as erosional bases, graded bedding, ripple cross-laminae, and plane-parallel laminae.

The Shikoku Basin and the trench wedge are supplied by sediment from rapid uplift and erosion of a collision zone between the Honshu arc and Izu-Bonin arc, and a

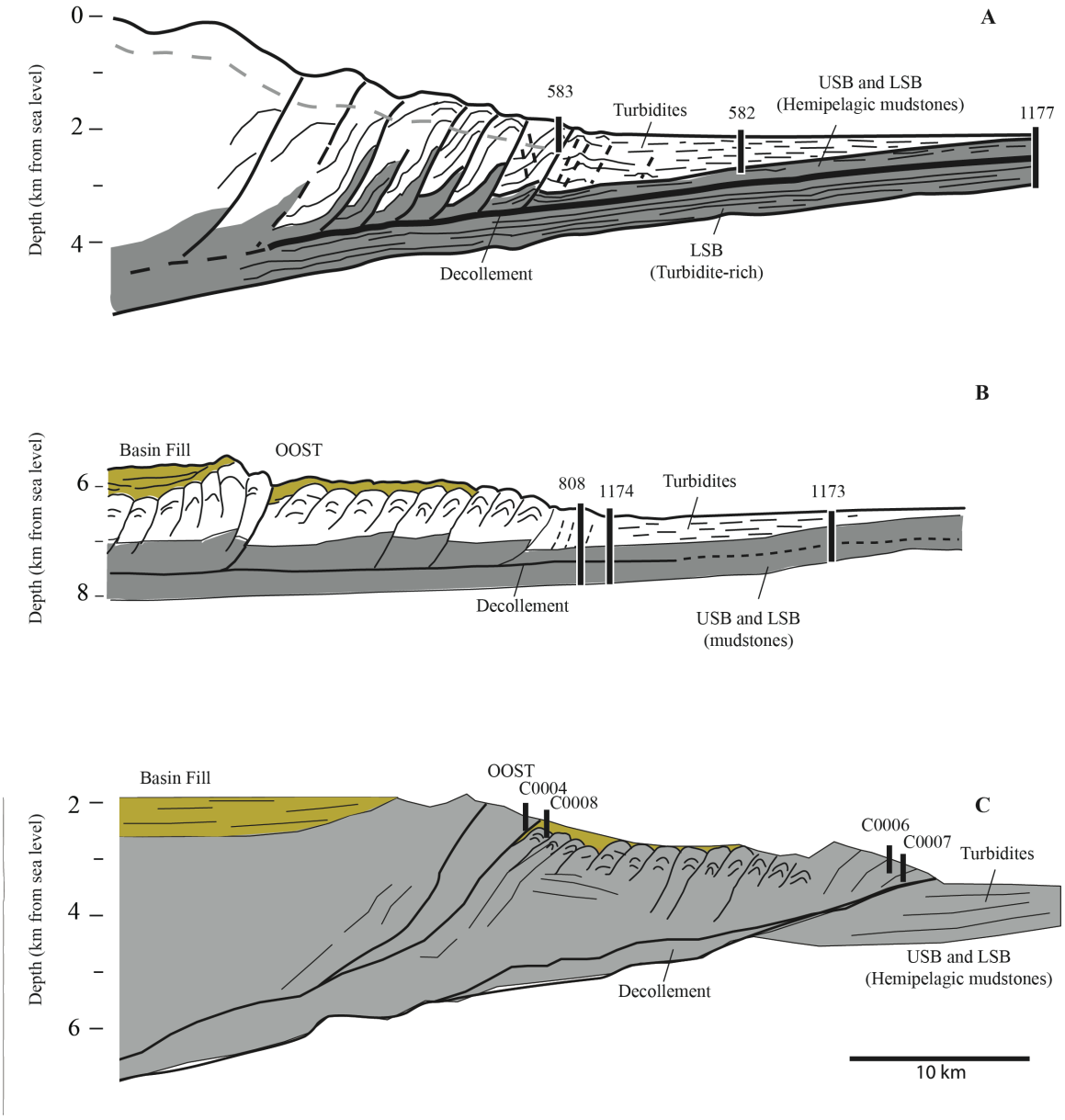

Figure 8. Interpreted cross-section based on seismic reflection lines, (A) Ashizuri transect, (B) Muroto transect, and (C) Kumano transect. LSB = Lower Shikoku Basin. USB = Upper Shikoku Basin. OOST = out-of-sequence-thrust (Saffer, 2009; Simpson, 2009).

system of submarine canyons that are located offshore Shikoku Island, Kii Peninsula, and Honshu; such as Suruga Trough, Tenryu Canyon, Shiono-misaki Canyon, and Ashizuri Canyon (Fig. 9). The Suruga Trough is associated by a canyon system that begins near the shoreline with many small channels and slope gullies of the Fiji River fan-delta (Shimamura, 1989). Most of the coarse-grained detritus was funneled initially through Suruga Trough before moving southwest down the axial trench gradient (Taira and Niitsuma, 1986; De Rosa et al. 1986; Marsaglia et al., 1992; Underwood et al., 1993a; Itoh and Nagasaki, 1996; Kamata and Kodama, 1999).

The Nankai accretionary prism on the landward side of the Nankai Trough, mainly consists of offscraped and underplated materials from the trough fill turbidites and the Shikoku Basin hemipelagic sediments (Hill et al., 1993). A large amount of terrigenous sediment is currently being channeled down the trench axis from the Izu-Honshu collision zone (Fig. 9) (Taira and Niitsuma, 1986; Aoike, 1999). These trench strata overlie the hemipelagic strata deposited on the Shikoku Basin crust before it reached the trench (Ike et al., 2008). Likewise, Piper et al. (1973) suggests that generic sedimentary facies model for trenches shows upward thickening and coarsening trends, such as from basalt at the base through pelagic ooze, hemipelagic mud, silty turbidites, and sand turbidites. Additionally, volcanic sediments and turbidites may be interstratified within this sediment package.

Lithologies exposed on the Japanese Islands are diverse and include the following fundamental units: accreted sedimentary and volcanic rocks of the Shimanto Belt, ophiolitic rocks of early Tertiary age, Neogene sedimentary rocks composed of fine-grained tuffaceous and terrigenous debris; quartz diorite bodies that intruded

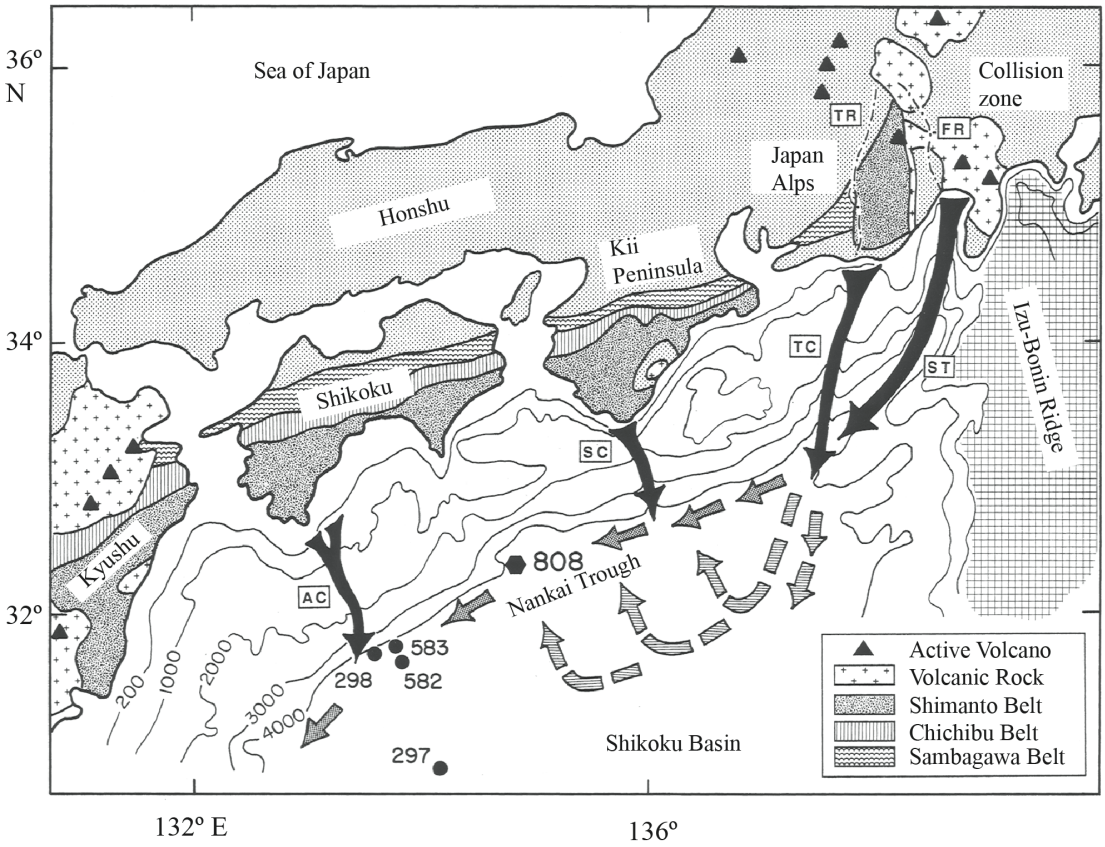

Figure 9. Index map showing the regional geography, geology, and bathymetry (in meters) of the southwest Japan. Numbers refer to DSDP and ODP site localities. Large black arrows symbolize major submarine canyons. Key: ST = Suruga Trough; TC = Tenryu Canyon; SC = Shino-misaki Canyon; AC = Ashizuru Canyon. Smaller arrows represent inferred pathways for turbidity currents within the trench, including flow-reflection trajectories off the seaward slope (Pickering et al., 1992; Underwood et al., 1993a). Major drainage basins in the Izu-Honshu collision zone including the Tenryu River (TR) and the Fuji River (FR) (Underwood and Pickering, 1996).

the Miocene volcaniclastic units, and Quaternary volcanic centers (including Mt. Fuji). Simultaneous volcanism and rapid uplift of accreted rocks during collision are responsible for a mixed detrital provenance signature. The rocks provide the main supply of terrigenous sediment.

2.4. Previous Studies

2.4.1. Clay Mineralogy

Cook et al. (1975), Chamley (1980), and Chamley and Cadet (1986) previously analyzed the clay minerals from the Nankai Trough (DSDP Sites 298, 582, 583) and Shikoku Basin (DSDP Sites 297, 442, 443 and 444). Chamley and Cadet (1986) pointed out that the Pleistocene turbidite section was dominated by mainly illite and chlorite. Also, an increase in abundance of smectite and mixed-layer clays down-section of the Shikoku Basin was reported. Previous studies of clay mineralogy in the vicinity of the Nankai Trough and Shikoku Basin demonstrated that the hemipelagic mud(stones) vary in composition largely as function of depositional age (Fagel et al., 1992; Underwood et al., 1993b; Streurer and Underwood, 2003; Underwood and Streurer, 2003). Miocene strata contain higher percentages of smectite, while Pliocene and Pleistocene deposits are dominated by illite and chlorite. The Nankai trough is dominated by 10-35% smectite, 20-35% chlorite, 30-50% illite, and a minor amount of kaolinite and mixed layer illite/smectite clays. The Shikoku Basin is characterized by 25-40% smectite, 20-35% illite, and 10-25% chlorite. Results from ODP Leg 190 Sites 1175 and 1176 show that relative mineral abundances for two slope basin sites average 36-37% illite, 25% smectite, 22-24% chlorite, and 15-16% quartz.

Underwood and Pickering (1996) summarize that illite is the most abundant clay mineral in the Nankai accretionary prism, and relative percentages of the major mineral components (illite, chlorite and smectite) are apparently uniform within the trench turbidite wedge. Smectite content increases within the upper Shikoku Basin facies as a result of alteration of disseminated volcanic ash. The smectite content decreases, relative

to other clay minerals, beginning at a depth of about 800 mbsf. The decrease in smectite content was resulted from by either lesser amounts of detrital smectite and volcanic ash transported into Shikoku Basin early in its history or burial temperatures great enough to initiate the transformation of smectite to illite at depths below 550 to 600 mbsf (Underwood and Pickering, 1996).

2.4.2. Permeability

Taylor and Fisher (1993) documented the results of permeability measurements that were made on samples of ODP Site 808 cores. Coring at ODP Leg 131 Site 808 recovered a sequence of accreted and subducted sediments from the toe of the Nankai convergent margin along the Muroto Transect (Hill et al., 1993). Coefficient of permeability ranges between 10^{-14} and 10^{-19} m^2 in horizontal and vertical directions. The coefficient of permeability of the upper two sedimentary units at Site 808 (Unit I and II), extend from 0 to ~556 mbsf, is quite variable and locally high, ranging between 10^{-14} and 10^{-15} m^2 because of uncemented sand layers. However, values gradually decrease from 10^{-16} m^2 at 320 mbsf to 10^{-17} m^2 above the décollement. Below the décollement, both k_v and k_h, generally increasing with depth, are about 5 x 10^{-17} m^2. The lowest coefficient of permeability is 10^{-19} m^2 for a sample from 1014 mbsf.

Gamage and Screaton (2003) and Adatia et al. (2004) documented results of permeability measurements that were made on samples from ODP Sites 1173 and 1174. Coring at ODP Sites 1173 and 1174 recovered a sequence of upper and lower Shikoku Basin facies along the Muroto Transect (Mikada et al., 2002). Gamage and Screaton (2003) reported that the measured samples from Site 1173 ranged in depth from 199.9 to 428.6 mbsf with lithologies consisting of silty claystone with moderate bioturbation.

Samples from Site 1174 ranged in depth from 538.2 to 941.8 mbsf with lithologies consisting of silty and siliceous claystone. The highest coefficient of permeability was 10^{-17} m^2 for a sample corresponding with an initial porosity of 66% from the upper Shikoku Basin facies. The lowest coefficient of permeability was 10^{-19} m^2 for a sample with an initial porosity of 35% from lower Shikoku Basin facies.

Gamage et al. (2011) focus on the permeability-porosity relationship of sediments from different subduction zones, such as northern Barbados, Costa Rica, Nankai, and Peru (Fig. 10). The Barbados accretionary complex is dominated by clay and claystone (Taylor et al., 1990), the Middle American Trench (Costa Rica) consists of siliceous hemipelagic sediments overlying pelagic carbonates (Silver et al., 2000), the Nankai accretionary complex is characterized by silty clays, and the Peru accretionary complex sediments vary between nannofossil and chalk diatom oozes (Gamage et al., 2005). For siliciclastic sediments and diatom oozes, permeability decreases with an increase in the percentage of clay-sized material. But nannofossil oozes have higher permeability values by 1.5 orders of magnitude than siliciclastic sediments of the same porosity, and show poor correlation between permeability and porosity. For compacted calcareous sediments and nannofossil chalks, the permeability trend overlaps the permeability trend for siliciclastic sediments. Neuzil (1994) suggested that siliciclastic sediments vary in permeability by nine orders of magnitude, while Spinelli et al. (2004) suggested five orders of magnitude for carbonate-rich sediments. Additionally, Neuzil (1994) pointed out a log-linear relationship between permeability and porosity by using data from compilations for argillaceous sediments (Fig. 10).

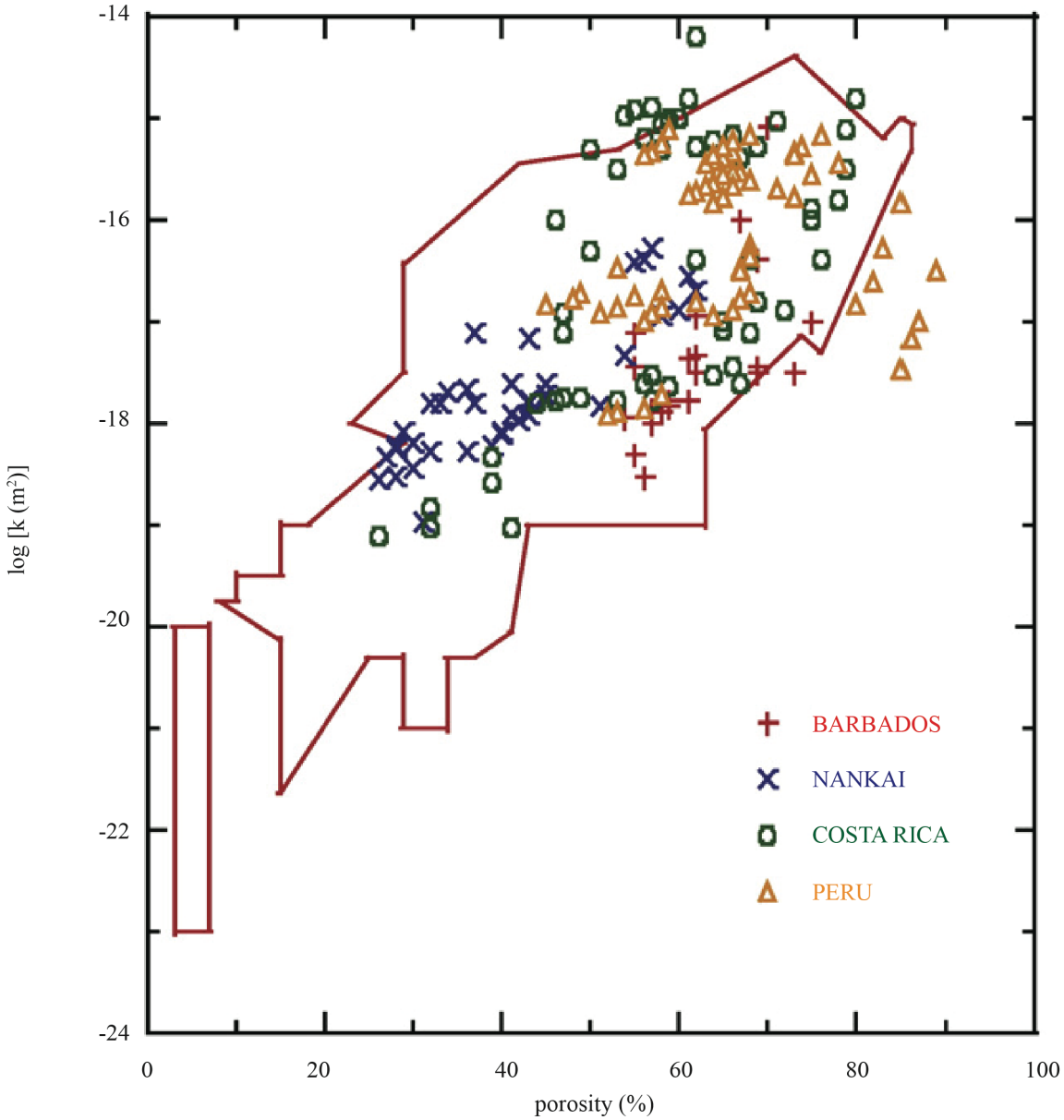

Figure 10. Plot of laboratory-derived permeability measurements as a function of porosity from Barbados, Costa Rica, Nankai, and Peru subduction zones superimposed on outline of Neuzil (1994) plot for argillaceous sediments (Gamage et al., 2011).

2.5. NanTroSEIZE Stage 1 and 2 Drilling Results

2.5.1. Lithostratigraphy of Megasplay Fault Zone

Drilling at Site C0004 reached the megasplay fault near its up-dip intersection with the seafloor. The fault zone is characterized by thin hemipelagic mudstone and volcanic ash layers (Expedition 316 Scientists, 2009d). The hanging wall of the fault consists of deformed hemipelagic mudstone and mass transport deposits with bent clasts of mudstone and silty clay layers. An unconformity exists between breccia and overlying slope-apron facies, with a hiatus that lasted from 2.0 Ma to 1.6 Ma. Four lithologic units were defined at Site C0004. Unit I is dominated by hemipelagic nannofossil-rich mud with rare volcanic ash and thin sand. Unit II, middle to early Pliocene in age, was divided into two subunits. Subunit IIA is dominated by sedimentary breccia and hemipelagic mud. Subunit IIB is dominated by hemipelagic mud with rare turbidite sands and volcanic ash. Unit III is fault-bounded interval of ash-bearing hemipelagic mud with abundant interface of volcanic ash. Unit IV is dominated by hemipelagic mud with turbidite sand and rare volcanic ash. Unit IV is interpreted to be underthrust slope sediments in the footwall of the megasplay (Fig. 11).

Site C0008 was drilled seaward of the shallow tip of the megasplay fault (Expedition 316 Scientists, 2009c). Site C0008 was defined in two lithologic units (Fig. 12). Unit I, Pleistocene in age, is characterized by slope basin facies. Subunit IA consists of nannofossil-rich silty clay, thin sand, and volcanic ash. Subunit IB, mass transport deposit, is characterized by silty clay and interbedded mudclast gravels. Unit II, Pliocene in age, is dominated by sand and minor silty clay. It is interpreted to be accreted trench wedge (Expedition 316 Scientists, 2009d).

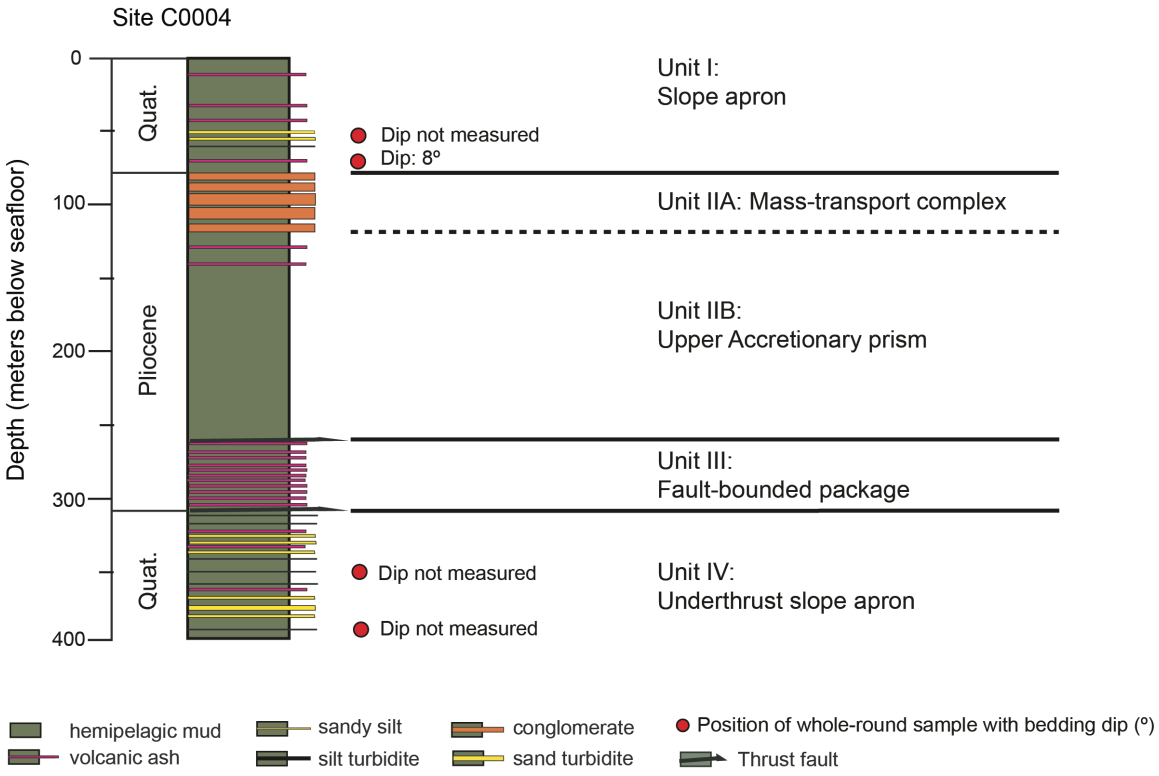

Figure 11. Stratigraphic column of Site C0004 with positions of samples used for permeability tests. Bedding dips are closest nearby intervals and taken from IODP Exp. 316 Site C0004 (Expedition 316 Scientists, 2009d). Vertical scale, 2 cm = 100 meters

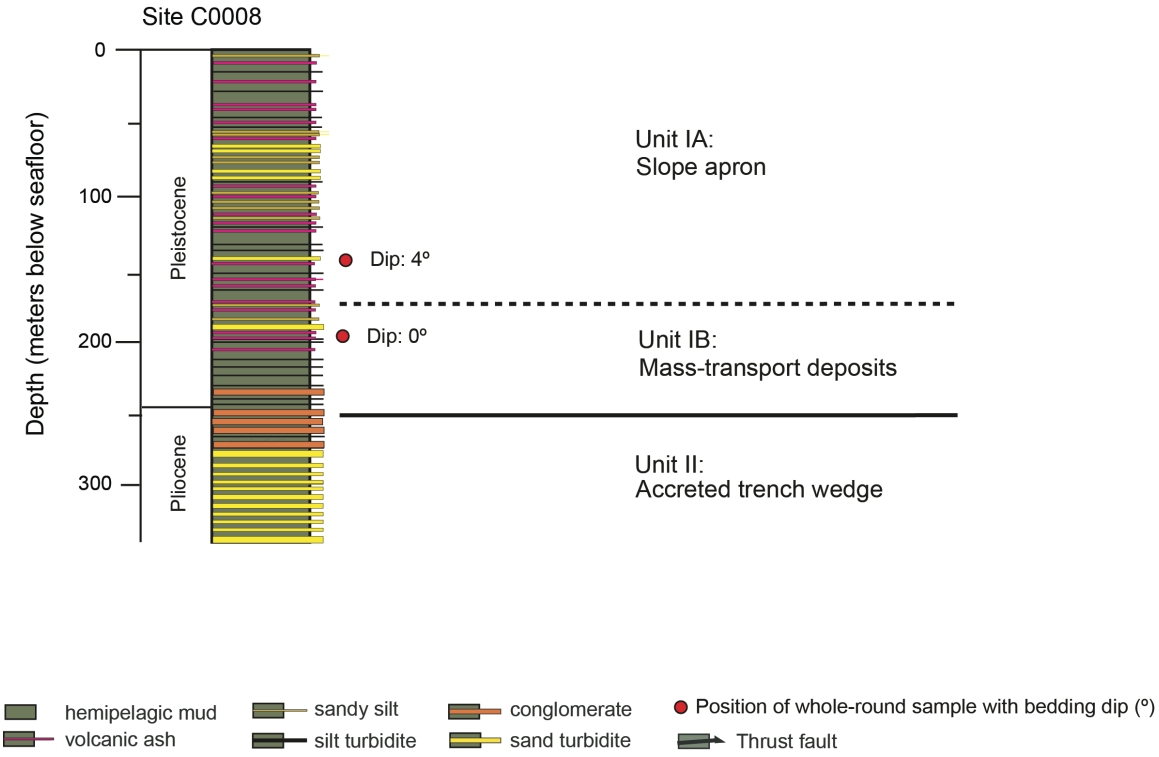

Figure 12. Stratigraphic column of Site C0008 with positions of samples used for permeability tests. Bedding dips are closest nearby intervals and taken from the IODP Exp. 316 Site C0008 (Expedition 316 Scientists, 2009c). Vertical scale, 2 cm = 100 meters.

2.5.2. Lithostratigraphy of Frontal Thrust Fault Zone

Drilling at Sites C0006 and C0007 documented frontal accretion from transfer of trench wedge and upper Shikoku Basin deposits into a complicated system of imbricate thrust slices (Expedition 316 Scientists, 2009a; Expedition 316 Scientists, 2009b). The boundary between Miocene-Pliocene hemipelagic/pyroclastic facies and the younger trench-wedge deposits within the hanging wall to the frontal thrust is an unconformity.

Three lithologic units were defined at this site (Fig. 13). Unit I, late Pleistocene in age, is dominated by hemipelagic mud with sand and silt turbidites. It is defined as trench-slope transition. Unit II, early to middle Pleistocene in age, consists of hemipelagic mud and sand turbidites with interbedded silt turbidites, and rare volcanic ash. It is interpreted as accreted trench-wedge facies. Unit III, early Pliocene in age, is dominated by hemipelagic mud with rare volcanic ash and interbedded silt turbidites. It is correlated with upper Shikoku basin facies (Expedition 316 Scientists, 2009a). The comparable hiatus at C0007 lasted from 3.65 Ma to either 2.06 or 1.46 Ma. The hiatus at the top of Unit III lasted from 2.87 Ma to 1.46 Ma. The accreted trench-wedge facies ranges in age from 1.46 Ma to 0.44 Ma.

Site C0007 was drilled on the main frontal thrust at the seaward edge of the accretionary prism (Fig. 14). Moderately consolidated clastic rocks are thrust over unlithified late Quaternary trench sediments; a thrust is observed in the seismic section at 200 mbsf. As parallel to observations of the Site C0006, four lithologic units were defined. Unit I is dominated by hemipelagic mud with sand silt layers and rare volcanic ash. Unit II consists of hemipelagic mud with thick silt turbidite interbedded, sand silt

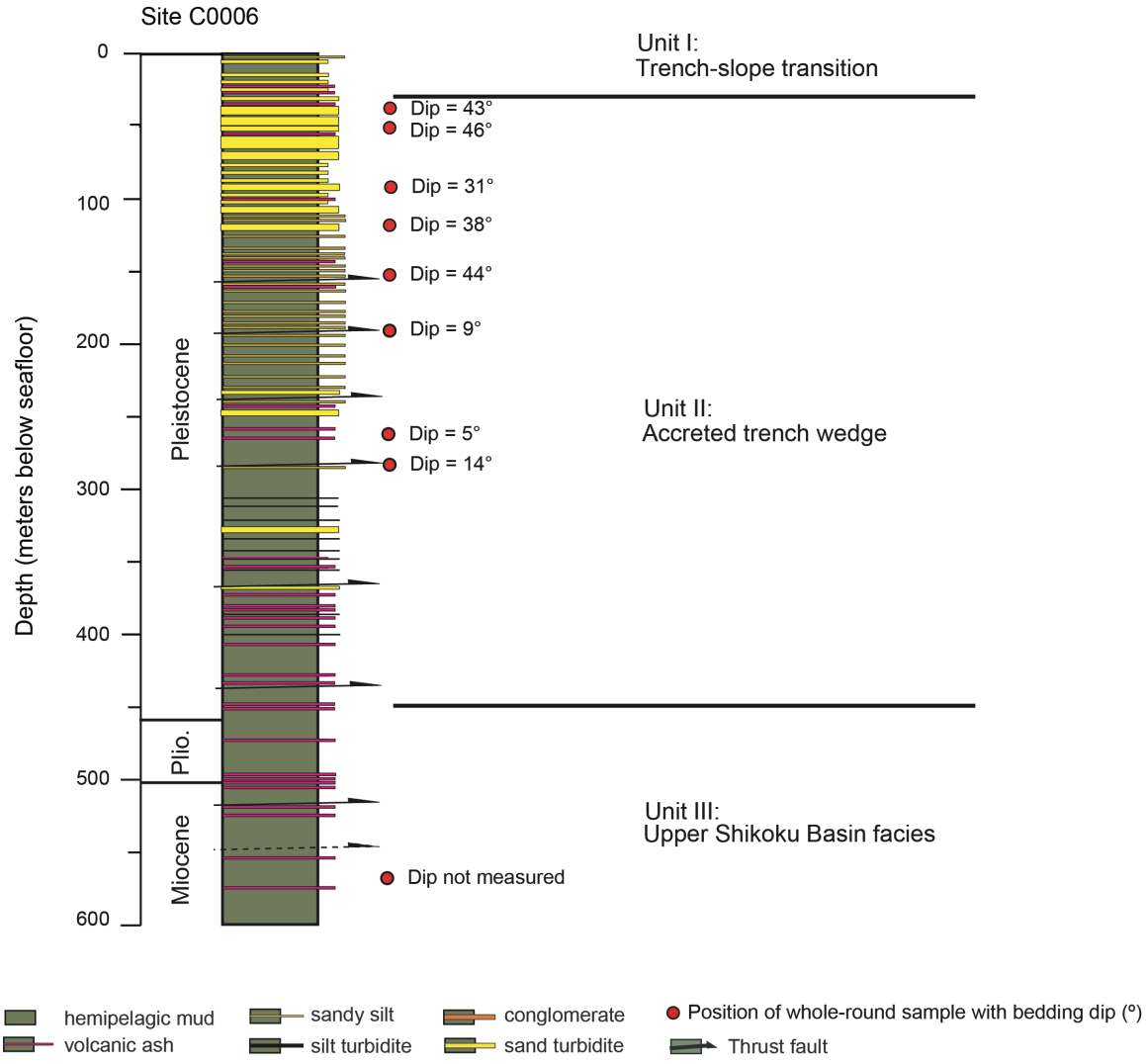

Figure 13. Stratigraphic column of Site C0006 with positions of samples used for permeability tests. Bedding dips are closest nearby intervals and taken from the IODP Exp. 316 (Expedition 316 Scientists, 2009a). Vertical scale, 2 cm = 100 meters.

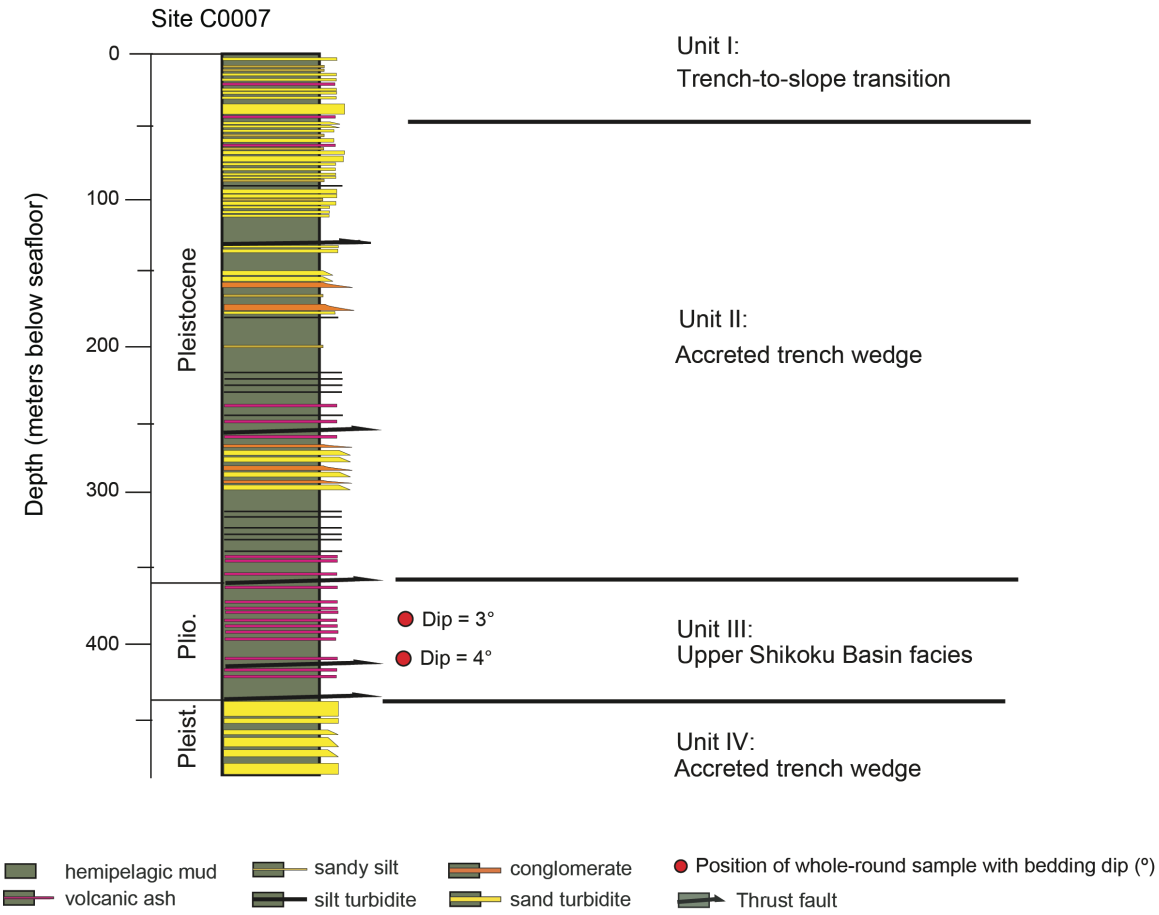

Figure 14. Stratigraphic column of Site C0007 with positions of samples used for permeability tests. Bedding dips are closest intervals and taken from the IODP Exp. 316 Site C0007 (Expedition 316 Scientists, 2009b). Vertical scale, 2 cm = 100 meters.

layers, rare volcanic ash, and mudclast gravels. Unit III is dominated by hemipelagic mud with volcanic ash and silt turbidites. The frontal thrust fault is located at ~440 m below sea floor and acts as boundary between Units III and IV. Unit IV, Pleistocene in age, is characterized by subducted trench wedge with hemipelagic mud and sand turbidites (Expedition 316 Scientists, 2009b)

2.5.3. Lithostratigraphy of Subduction Inputs of Shikoku Basin

Site C0011 is located on the northwest flank of the Kashinosaki Knoll in the Shikoku Basin. The main goal of drilling at this location was to recover a complete section of sedimentary strata and uppermost igneous basement as subduction inputs to the Nankai Trough. Site C0011 Holes A and B were drilled during the IODP Expedition 322. However, the lithostratigraphy from the upper part, extends from 0 to 350 meter below sea floor, could not be confirmed because that interval was logged but not cored. One of goals of the IODP Expedition 333 was to recover a complete section of sedimentary strata. Site C0011 Holes C and D were drilled during the IODP Expedition 333 (Fig. 15). Five lithologic units were defined at this site. Unit I is dominated by hemipelagic mud and air-fall volcanic ash. Early Pliocene defines this unit in age. Unit II, volcanic turbidite facies, is characterized by tuffaceous sandstone, volcaniclastic sandstone, chaotic (mass transport deposits), turbidite mudstone, and hemipelagic mudstone. Unit III consists of heavily bioturbated hemipelagic mudstone. Unit IV is dominated by laminated silt/mud turbidites, fine sand turbidites, and hemipelagic mudstone. Unit V is a tuffaceous facies. Depth to igneous basement at ~1050 mbsf is interpreted from seismic reflection data (Expedition 322 Scientists, 2010a).

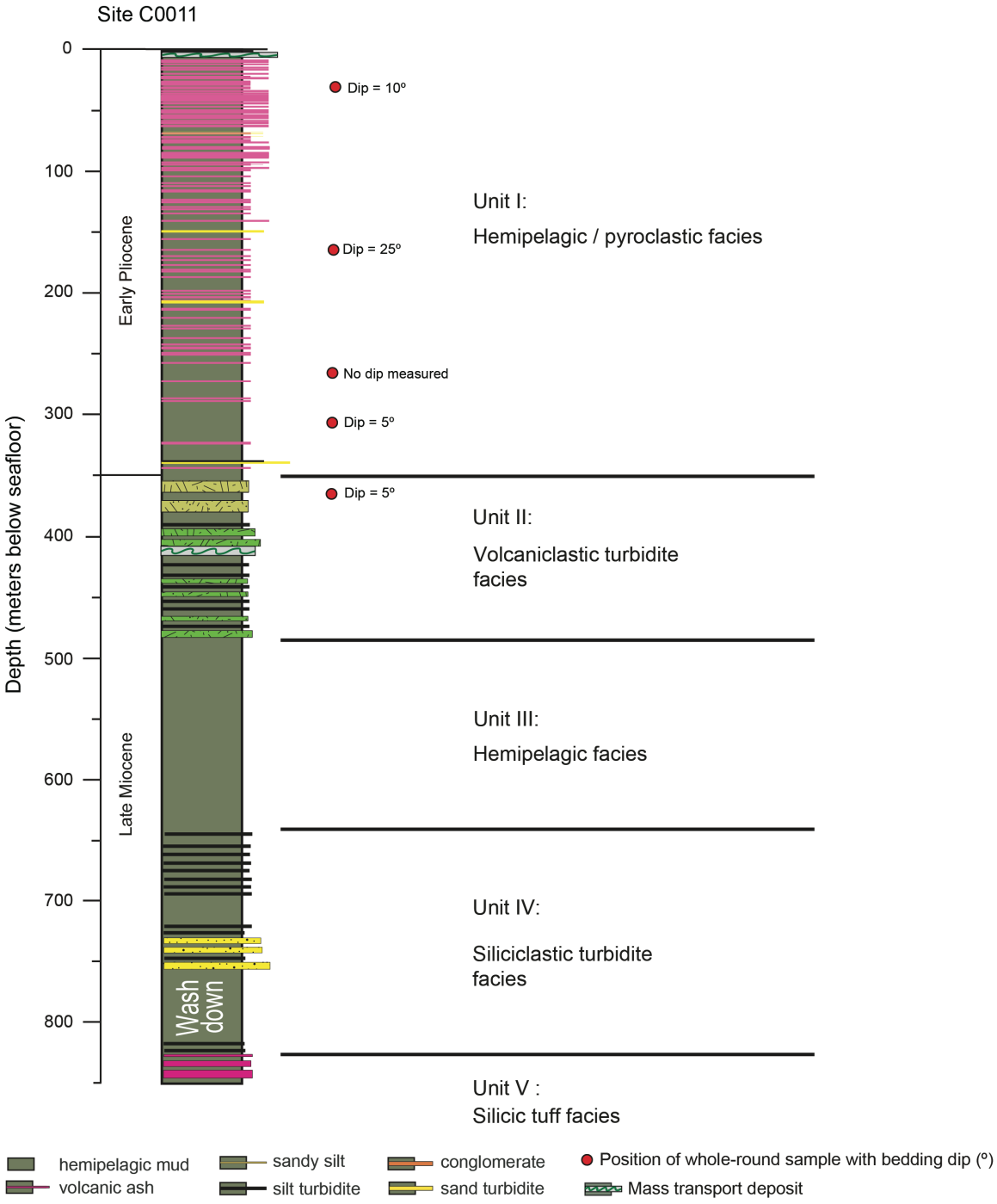

Figure 15. Stratigraphic column of Site C0011 with positions of samples used for permeability tests. Bedding dips are closest nearby intervals and taken from the IODP Exp 333 (Expedition 322 Scientists, 2010a; Expedition 333 Scientists, 2011). Vertical scale, 2 cm = 100 meters.

3. METHODS

3.1. Sample Recovery

Samples from the Kumano transect were recovered by D/V Chikyu during Expeditions 315, 316, 322 and 333. Each hole drilled at a given site was named in order (A, B, C, etc.). Coring techniques include hydraulic piston core (H), extended core barrel (X), and rotary core barrel (R). The depth of core is measured in meters below seafloor (mbsf). The cores are generally 9.5 meters long, and the sections are cut every 1.5 meters and labeled successively from top to bottom. Each interval is measured in centimeters from top of the section. A sample identification number of "333-C0011D-19H-5, 99 cm" would indicate the following:

333	C0011	D	19	H	5	99
(Expedition)	(Site)	(Hole)	(Core)	(Technique)	(Section)	(Interval)

3.2. Sample Preparation for Multi-direction Constant Flow Test

The whole-round core samples were capped and taped in their plastic core liners onboard D/V Chikyu, sealed with wet sponges in aluminum vacuum bags to prevent moisture loss, and stored at 4°C until immediately prior to trimming. To extract each specimen, the plastic core liner was cut lengthwise along two lines 180º apart using a hacksaw. The core liner was then removed to extrude the sample. Cylindrical specimens were trimmed for permeability tests in the vertical (along-core) direction were trimmed using a wire saw and soil lathe (Fig. 16). Specimen length after trimming ranged from

approximately 4.4 to 5.9 cm and averaged 5.3 cm. Specimen diameter ranged from approximately 3.4 to 4.1 cm and averaged 3.8 cm. These dimensions were measured at several points using a caliper to a resolution of 0.03 cm and averaged to obtain the values used for subsequent calculations. Specimens for tests in the horizontal (cross-core) direction were trimmed from material immediately below the specimen for vertical (along-core) testing. These specimens were trimmed perpendicular to the core axis (Fig. 16). Bedding dip with respect to the core axis was not taken into account during trimming. Initial specimen porosity was estimated from gravimetric water content of the specimen trimmings by assuming 100% pore water saturation. Specific gravities of the mineral solids were exported from shipboard data for intervals adjacent to each whole round sample. Gravimetric water content of the specimen trimmings was determined by measuring the ratio of the mass of water to the mass of mineral solids determined by oven-drying the trimmings at 105˚C until constant mass was reached (generally within 24 hours) in accordance with shipboard measurements. Salt correction (eq. 1) has been applied for all gravimetric water content and porosity calculations.

$$W_c\ (\%\ \text{dry wt}) = (M_t - M_d)/(M_d - r\,M_t) \qquad (1)$$

where

M_t = total mass of the saturated sample,

M_d = mass of the dried sample, and

r = salinity (per mil).

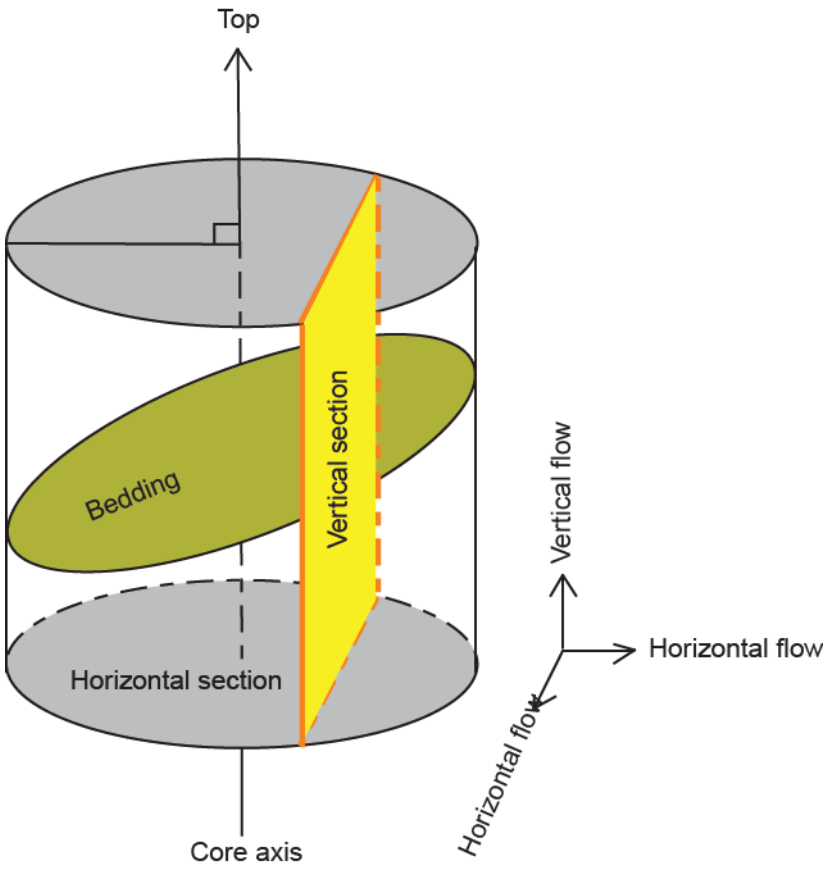

Figure 16. Illustration representing the horizontal and vertical section of core.

3.3. Constant-Flow Apparatus

Constant-flow, flow-through permeability tests were used to determine hydraulic conductivity in the vertical and horizontal core directions. A withdrawal-infuse syringe pump (KDS Scientific, Model 260) is used at University of Missouri to simultaneously inject and extract pore fluid from the top and bottom of the specimen (Fig. 17). The system consists of an acrylic confining cell to contain the specimen and provide isotropic effective confining stress, a constant flow syringe pump, one differential pressure transducer to measure hydraulic head difference between the specimen top cap and bottom cap, and an air/water interface panel for regulating the confining fluid pressure and pore fluid backpressure (Fig. 18). Signals from the differential pressure transducer are acquired to obtain hydraulic head difference through the specimen at a precision of ±1 cm H_2O over a range spanning ±1000 cm H_2O. A digital interface is used for readout and storage of values of effective isotropic confining stress (σ'), hydraulic head difference (Δh), and time duration measurements made during each test run. The flow pump holds two syringes (Hamilton GasTight Series 1000) and has the capability to cycle continuously back and forth in a push-pull action. As one syringe is infusing pore fluid into the specimen the other withdraws an equal volume of fluid from the other end of the specimen at the same rate. Volumetric flow rate (Q) for the series of tests described here ranged from a minimum of 7.0E-05 cm^3/min to a maximum of 8.0E-03 cm^3/min.

Figure 17. Pictures of constant-flow permeability testing system at University of Missouri-Columbia.

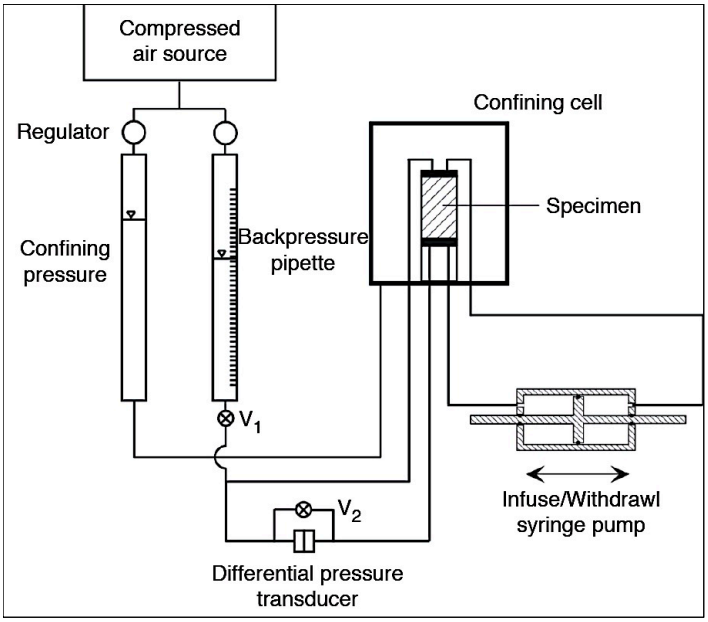

Figure 18. Schematic of constant-flow permeability testing system at University of Missouri-Columbia.

3.4. Backpressure Saturation

Prior to testing, all permeant lines and porous stones are saturated with simulated seawater (25 g NaCl to 1 L tap water). A specimen is placed on the pedestal, the top cap applied, and a latex membrane placed on the specimen using a vacuum membrane expander. The confining chamber is then sealed and the cell is filled with tap water. Saturation of the specimen was achieved by ramping pore fluid backpressure to 70 psi (0.48 MPa) using the panel board (air/water interface) while also ramping the confining pressure to maintain an effective isotropic confining stress of 5 psi (0.034 MPa). Elevated backpressure was maintained for at least 24 hours. Skempton's *B*-value was computed to check saturation of the specimen by increasing the confining pressure (σ) from 75 to 80 psi and measuring the corresponding pore pressure (υ) response. Pressure difference between top and bottom of specimen, resulted by increased confining pressure, was considered as pore pressure response.

$$B = \Delta\upsilon / \Delta\sigma \qquad (2)$$

Specimens were considered saturated if $B \geq 0.95$ (eq. 2). Once saturation was achieved, the cell pressure was increased to consolidate the specimen at isotropic effective stress of 0.55 MPa. Pore water was allowed to drain during consolidation from both the top and bottom of the specimen by opening top and bottom valves on the confining cell system. The volume of pore water expelled was measured using the backpressure pipette and monitored for equilibrium to calculate the corresponding volume change of the specimen.

3.5. Constant Flow Permeation

During this study, constant-flow tests on 36 specimens (21 trimmed vertically, or parallel to the core axis, and 15 trimmed horizontally, or perpendicular to the core axis)

were completed at effective confining stress of 80 psi (0.55 MPa). Only 15 horizontal tests could be conducted because of limited sample size. Tests at this effective stress were run using four flow rates; two tests were conducted with a top-to-bottom flow direction (denoted subsequently as a negative flow value), and two tests were conducted with a bottom-to-top flow direction (denoted as a positive flow value) to obtain replicate permeability values. During each test, transient response from the differential pressure transducer was monitored for steady state head difference (Δh_s). Values of applied discharge velocity (v) and steady state hydraulic gradient (i_s) were plotted to assess consistency among the four test runs and linearity in their relation. Coefficient of determination (R^2) calculated by least-squared linear regression of these relations were not less than 0.9835, indicating good repeatability among the four flow tests conducted at each flow rate and the applicability of Darcy's Law for calculating hydraulic conductivity (Fig. 19).

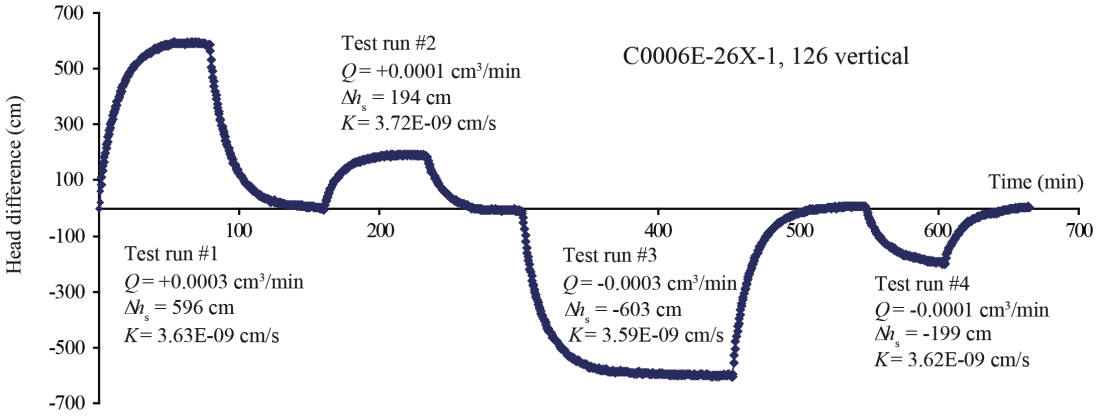

Figure 19. Plot of responses of transient head difference (Δh_s) during flow-through testing. Q = volumetric flow rate, K = hydraulic conductivity. Positive (bottom to top) and negative (top to bottom) values indicate the direction of flow during the testing.

3.6. Constant-Flow Test Data Analysis

Hydraulic conductivity (K) is defined by Darcy's Law as the ease with which fluid will flow through a porous medium. The value of K (units = cm/s) is a function of both matrix and fluid properties (eq. 3):

$$Q = -K \times A \times (\Delta h_s / \Delta L) \quad (3)$$

where

Q = applied volumetric flow rate ($L^3 T^{-1}$),

K = hydraulic conductivity ($L T^{-1}$),

A = cross sectional flow area (L^2),

Δh_s = steady-state difference in head across the specimen (L), and

ΔL = the length over which head difference occurs, taken as the initial height of the specimen (L).

Intrinsic permeability (k) is also defined as the ease with which fluid flows through a porous medium, but it is a function of only matrix, not fluid properties. Permeability (units = m^2) relates to the size and degree of interconnection of pore space (Schwartz and Zhang, 2003). Hydraulic conductivity values are converted to intrinsic permeability using the following equation (eq. 4):

$$k = (K \times \mu) / (\rho \times g) \quad (4)$$

where

μ = viscosity of pore fluid (0.001 Pa.s at 25°C),

ρ = density of pore fluid (1027 kg/m^3), and

g = gravitational acceleration (9.81 m/s^2).

3.7. Bulk Mineralogy

Shipboard analyses of bulk sediment samples by X-ray diffraction (XRD) have been a routine part of measurements by the IODP, the ODP and the DSDP. All such data described in this study are from clusters of subsamples next to whole round samples. Clusters include several types of co-located subsamples cut from top or bottom part of all whole round samples. The objective is to estimate relative weight percentages of total clay minerals, quartz, plagioclase, and calcite. The presence of a specific detrital and/or authigenic minerals in a bulk powder can be detected easily through visual recognition of characteristic peak positions (Table 1). Samples are freeze-dried, crushed with a ball mill, and mounted as random bulk powders. The instrument settings, PANalytical CubiX PRO (PW3800), are as follows: Generator = 45 kV and 40 mA; tube anode = Cu; wavelength = 1.54060 Å (Kα1) and 1.54443 Å (Kα2); step spacing = 0.005°2θ; scan step time = 0.648 s; divergent slit = automatic; irradiated length = 10 mm; scanning range = 2°2θ to 60°2θ; spinning = yes. MacDiff version 4.2.5. software is used on D/V Chikyu to analyze the peak positions, and compute peak areas (www.ccp14.ac.uk/ccp/ccp14/ftp-mirror/krumm/Software/macintosh/ macdiff/MacDiff.html).

Table 1. Characteristic X-ray diffraction peaks for semiquantative area analysis.

Mineral	Reflection	d-value (Å)	Peak Position (°2θ)
Total clay	Multiple	4.478	19.4–20.4
Quartz	101	3.342	26.3–27.0
Plagioclase	002	3.192	27.4–28.2
Calcite	104	3.035	29.1–29.7

It is more problematic, however, to estimate the relative abundance of a mineral in bulk sediment with meaningful accuracy (Moore, 1968; Cook et al., 1975a; Heath and Pisias, 1979; Johnson et al., 1985; Fisher and Underwood, 1995; Underwood et al., 2003). Calculations of relative mineral abundance utilize a matrix of normalization factors (Table 2) derived from integrated peak areas and singular value decomposition (SVD). These factors are unique for each diffractometer and are computed after analyzing standard mineral mixtures, such as quartz (Saint Peter sandstone), feldspar (Ca-rich albite), calcite (Cyprus chalk), smectite (Ca-montmorillonite), illite (Clay Mineral Society IMt-2, 2M1 polytype), and chlorite (Clay Mineral Society CCa-2) (Underwood et al., 2003).

Calculated values of a mineral's weight percent should only be regarded as relative percentages within a four-component system of clay minerals + quartz + plagioclase + calcite. How close those estimates are to their absolute percentages within the mass of total solids will depend on the abundance of amorphous solids (e.g., biogenic opal and volcanic glass), as well as the total of all other minerals that occur in minor or trace quantities. For most natural samples, the absolute errors are probably between 5% and 10%. Thus, the primary value of bulk powder XRD data should be to identify spatial and temporal trends in sediment composition and to assist with core-log integration.

Table 2. Normalization factors for calculaion of relative mineral abundance using bulk powder X-ray diffraction analysis (Expedition 316 scientists, 2009e).

Influencing mineral	Affected mineral in standard mixture			
	Total clay	Quartz	Plagioclase	Calcite
Total clay	9.8956702E–03	–1.5889532E–04	–2.8855808E–04	–7.3842803E–04
Quartz	–4.7221169E–05	5.8782392E–04	–4.7869325E–05	–3.1098843E–05
Plagioclase	7.2794763E–04	–4.2840613E–05	1.3719777E–03	–3.6005495E–05
Calcite	4.2042411E–05	3.3021188E–06	–4.1329499E–06	1.3071455E–03

3.8. Sample Preparation for Clay Mineralogy

Sample preparation for X-ray diffraction (XRD) analyses at University of Missouri consists of seven main steps. First, ~5 g specimens of mud or mudstone must be gently crumbled and placed in a glass beaker with 3% H_2O_2 for at least 24 hours until digestion of organic matter stops. The second step is adding a solution of 250 mL of 4 g sodium hexametaphosphate to 1 L deionized H_2O to disperse the clays. The third step is immersion of breaker into an ultrasonic bath to disaggregate for 10 min. The fourth step is washing the sample to dilute the salt and dispersant that was added before. Samples must be washed via centrifugation (using six 60 mL tubes per sample at 8200 rpm for 25 min), re-suspended in 360 mL of deionized distilled water, washed again, and transferred in suspension to a 125 mL plastic bottle. The fifth step is using an ultrasonic cell disruptor for ~5 min. The sixth step is to separate the <2 μm fraction using a centrifuge at 1000 rpm for 2 min, 24 s. The last step is transferring the 2 μm fractions to glass slides using the filter-peel method (Moore and Reynolds, 1989) with a 0.45 μm membrane. Slides are solvated in an ethylene glycol atmosphere overnight at 60°C to expand the smectite. The time elapsed between removals from the ethylene glycol chamber and scanning is <80 min to minimize the effects of glycol evaporation on peak position.

3.9. X-Ray Diffraction Analysis

A Scintag PAD V X-ray diffractometer was used to scan slides from 3°to 26.5°2θ, at range of 1°2θ/min, step size 0.01°2θ at the following parameters: radiation = CuKα; scan rate = 1°/min; step size = 0.01; voltage = 40 kV; current = 30 mA; and slits = 0.5 mm (divergence) and 0.2 mm (receiving). MacDiff software (version 4.2.5) was used to process the digital data (Petschick, 2001) to establish a baseline of intensity, smooth

counts, and correct peak positions (using the quartz (100) peak at 20.85°2θ; d-value = 4.24 Å), and calculate integrated peak areas (total counts) (Fig. 20).

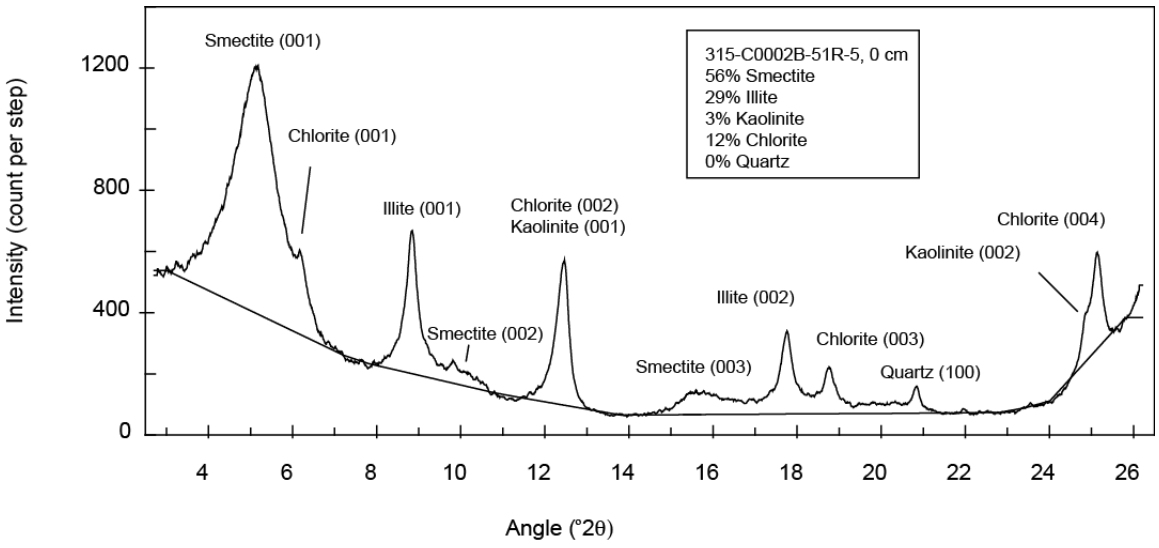

Figure 20. An example of X-ray diffraction results for sample 315-C0002B-51R-5, 0 cm. Labeled clay-size minerals with their Miller Indices.

3.10. Calculating Relative Clay Mineral Abundances

The integrated peak areas for basal reflections of smectite, illite, kaolinite, chlorite, and quartz are measured to calculate their relative abundances in the clay-sized fraction by weight. The targeted peaks are shown in Figure 20: smectite (001) at ~17 Å; illite (001) at ~10 Å; chlorite (002) at ~7 Å; and quartz (100) at 4.26 Å; some flaws with this method arise from peak overlap. The chlorite (001) peak occurs on the shoulder of the glycol-solvated smectite (001) peak at ~14 Å. To overcome this problem, we adjusted the limits for peak area to subtract the counts generated by chlorite. More problematic is the complete overlap of chlorite (002) and kaolinite (001) peaks at ~7 Å. We calculated the ratio of those minerals using the kaolinite (002) and chlorite (004) reflections and the method described by Guo and Underwood (2011b). Interlayers of illite also affect the

geometry of the smectite (001) peak, and illite (001) / smectite (002) peak merges into the illite (001) peak as the percent illite in I/S increases. This interference can add counts from mixed-layer clay to peak area values for both smectite and illite.

Another challenge in determining relative clay-mineral abundance in natural sediments is selection of accurate weighting factors. One common method (Biscaye, 1965) multiplies the peak area of smectite (001) by 1x, illite (001) by 4x, and chlorite (002) by 2x, regardless of each mineral's abundance. The peak area generated by a given phase and reflection increases with that mineral's abundance, but each additional phase in a mixture also affects the intensity of all other reflections differently. Results are also affected by differences in sample disaggregation technique, chemical treatments, particle size separation, and the degree of preferred orientation of clay mounts (Moore, 1968; McManus, 1991). Thus, to improve the accuracy, singular value decomposition (SVD) can be used (Fisher and Underwood, 1995) to compute a matrix of normalization factors for clays, using the results from standard mineral mixtures with known weight percentages. SVD factors for the clay-size fraction are shown on Table 3.

Table 3. XRD normalization factors for clay-size fraction (Underwood et al., 2003). C/K = Chlorite (002)-Kaolinite (001) overlap.

<2 micron fraction	Influencing Mineral	Affected mineral in standard mixture			
		Smectite	Illite	C/K	Quartz
	Smectite	3.7398559E-04	-2.8994615E-05	-3.4377535E-05	-7.4421238E-05
	Illite	4.2720105E-05	1.2499784E-03	-2.8363880E-05	3.3838456E-05
	C/K	-6.7662186E-05	-2.0084190E-07	7.6974847E-04	5.2408810E-05
	Quartz	2.4368789E-03	9.2311541E-04	8.1951090E-04	3.7061975E-03

3.11. Imaging of Grain Fabric

Specimens for imaging of grain fabric were cut from the whole round core samples while trimming cylinders for the flow-through tests, using a razor blade at vertical orientation and horizontal orientation relative to the axis of the core. Grain fabric of wet, uncoated, and unfixed specimens was imaged using an FEI Quanta 600 FEG scanning electron microscope (SEM). The instrument operates in environmental mode (ESEM) at 30 kV, with the specimen chamber pressure set at 700 Pa. Water vapor (~98% humidity) from a built-in reservoir keeps the specimen from losing moisture. The temperature of the cooling stage was set to 2ºC. The specimens were imaged with a gaseous backscattered electron detector, spot 3.0 at a working distance of around 10 mm. This combination generates an imaging resolution of approximately 4 nm, and the dimensions of the field of view are about 145 μm by 130 μm with 2000X magnification. Specimens were placed in the holder on the stage with the imaged surface facing upward. "Center stage" and "Tilt" commands of the ESEM controlling software were used to manually adjust the imaging face to an orientation as close to perpendicular as possible to the imaging beam. All the image files were saved with color grey mode in tiff format (Fig. 21).

Digital images were processed using software known as ImageJ (available at http://rsbweb.nih.gov/ij/index.html). Processing steps adhere to the following: (1) contrast enhancement, by linear stretching of the grey level histogram in order to use 256 grey level values (Fig. 21A); (2) median filter, by moving each pixel value to the median values of 9 closest pixels (to reduce noise); (3) mean filter, by replacing each pixel with the neighborhood mean. The size of the neighborhood is specified by entering its radius

in the dialog box (to preserve subtle details); (4) median hybrid filter, by moving each pixel to the median values of the middle horizontal 3 pixels, center vertical 3 pixels and center pixel of those 9 closest pixels (to reduce noise while preserving linear features); (5) threshold, by adjusting and picking up one point of grey level histogram (to select objects); (6) make binary, to transform the grey image to white and black image (Fig. 21B); (7) overlap the image onto the original image and set its alpha value (transparency) to 60% in Adobe Photoshop CS5 software, then separate objects that touch, by manual adjustment with eraser tool (Fig. 21C); (8) median filter with ImageJ, to remove objects less than 9 pixels in size (because measurements on small objects are mostly biased); (9) fill the holes on the objects (Fig. 21D); (10) measure automatically, to obtain the long-axis and short-axis dimensions and long-axis orientation of an object. The software can automatically determine the long or short axis (apparent dimensions) of the objects in the 2-D image. The results are saved in a text file automatically after the measurement.

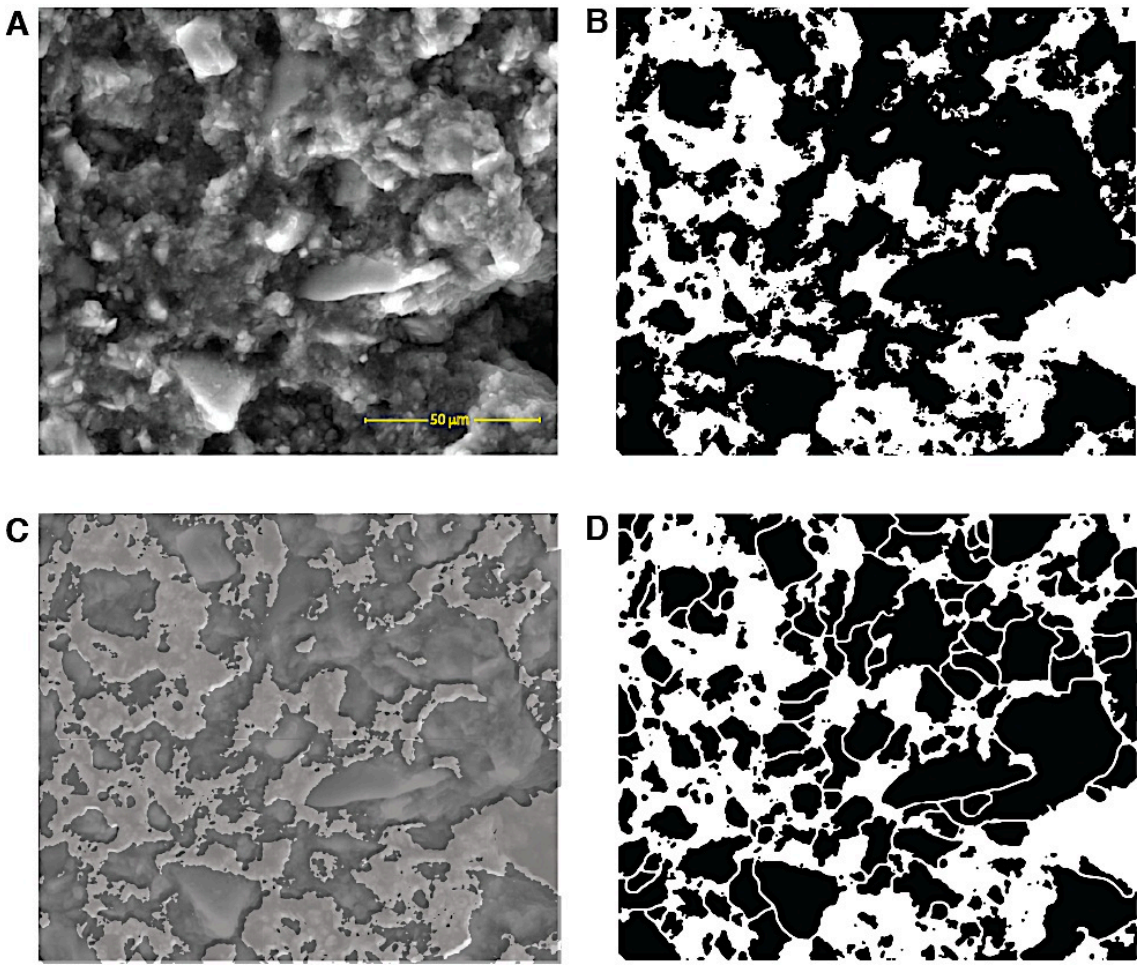

Figure 21. Illustrations of steps used during image analysis of microfabric, 316-C0006E-5H-1, 128 cm. (A) ESEM image, (B) Binary image obtained with ImageJ software, (C) Binary image (transparency = 60%) overlying the original ESEM image, (D) Binary image after particle separation using the eraser tool in Photoshop CS5 software.

3.12. Characterization of Microfabric Anisotropy

Grain fabric was characterized statistically using rose diagrams to depict orientations of the apparent long particle axes. In petrography, SEM, and TEM studies, most investigators measure between 100 and 500 grains per thin or ultrathin section (Krumbein, 1935; Friedman, 1958; van der Plas, 1962; Griffiths, 1967; Chiou et al., 1991) and generally between 100 and 500 grains were counted. Each particle orientation (apparent long axis) was assigned to an angle between 0º and 180º. For the vertical section, the core axis is oriented at 90º. Rose diagrams were constructed using software known as Rozeta (available online at http://www.softpedia.com/get/Science-CAD/Rozeta.shtml). This software automatically counts the number of particles according to their orientation and combines data into bins of 10º intervals. In addition to the rose diagram, the number of values in each bin was summed and normalized to 100%. Cumulative frequency curves of the normalized bin percentages were constructed to show the distribution of grain orientation and calculate graphical statistics (Fig. 22). Various statistical methods can be used to characterize the degree of preferred grain orientation (Folk and Ward, 1957; Martinez-Nistal et al., 1991; Zaniewski and van der Meer, 2005). The Folk and Ward (1957) formula was developed originally to graphically compute values of sorting (standard deviation) for grain size data. The equivalent equation for standard deviation of grain orientation (d) equals:

$$d = [(\varphi_{84} - \varphi_{16}) / 4] + [(\varphi_{95} - \varphi_{5}) / 6.6] \quad (5)$$

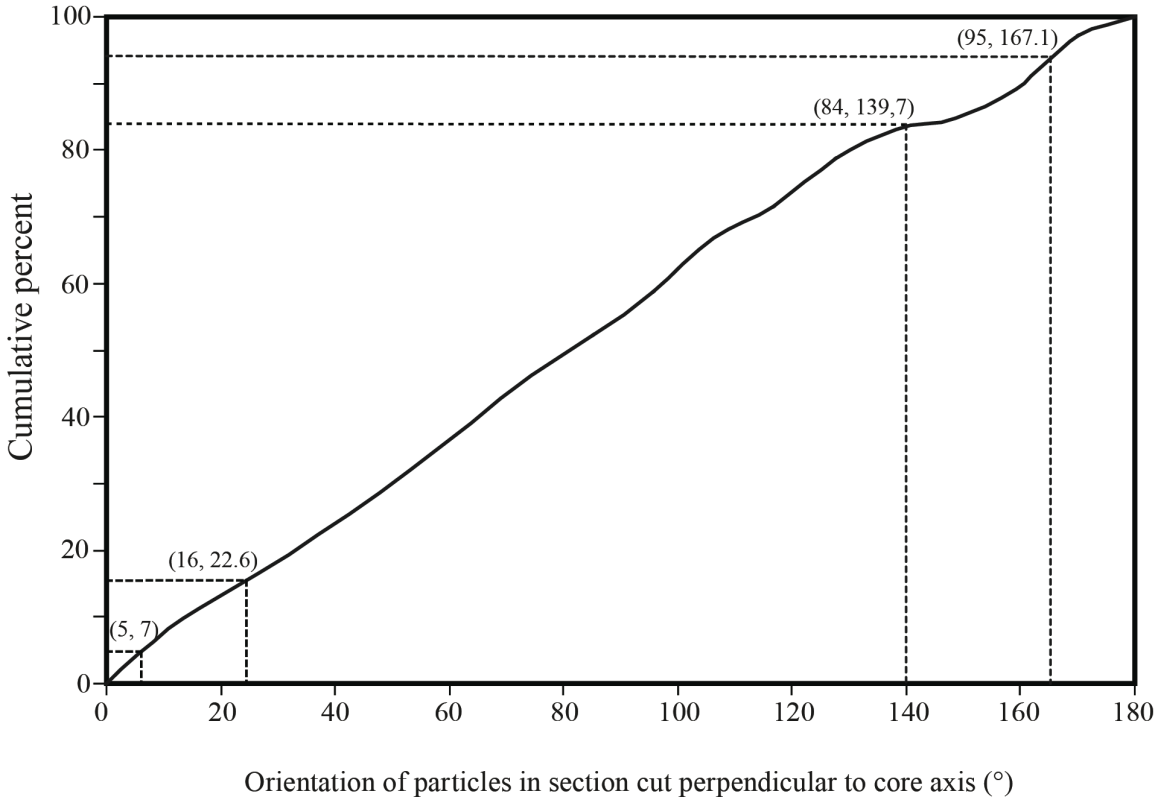

Figure 22. An illustration showing the distribution of grain orientation by one representative cumulative frequency curve, sample 316-C0006E-5H-1, 128 cm.

Where; φ_{84}, φ_{16}, φ_{95}, and φ_5 represent the angle of orientation (in degrees) of a particle's apparent long axis at the 84th, 16th, 95th, and 5th percentiles, respectively, on the cumulative frequency curve. This graphical technique avoids the laborious calculations required by moment statistics (Chiou et al., 1991). If the fabric of sediment shows strong preferred orientation, then the sorting of orientation angles will be more tightly clustered and the cumulative frequency curve will be steeper around the median. Numerically, the largest value of *d* is 72.3° (i.e., a case in which φ_{16} and $\varphi_5 = 0°$, φ_{84} and $\varphi_{95} = 180°$). Each standard deviation was normalized to this maximum standard deviation by calculating the "index of microfabric orientation" *(i)* as shown in the following formula:

$$i = 1 - (d / 72.3) \qquad (6)$$

The closer the value of *i* is to 1, the more the particles are aligned in a preferred direction. For a highly random arrangement of particles, the cumulative curve generally has a slope less than 0.75 near the median, the standard deviation of orientation is greater than 35°, and the index of orientation is smaller than 0.51. For well oriented clay particles, the slope of the cumulative curve is steep near the median, the standard deviation of grain orientation is smaller than 25°, and the index of micro-fabric orientation is greater than 0.65. To compare *i* values from imaging surfaces that were cut parallel and perpendicular to the core axis, I calculated the anisotropy of orientation as the ratio of i_h / i_v.

4. RESULTS

Table 4 summarizes the values of gravimetric water content and porosity for trimmings measured before and after each constant flow-through test. It also includes the average height (units = cm) and diameter (units = cm), and Skempton's *B*-value of each specimen, shipboard measurements of grain density (units = g/cm^3) and porosity. Table 5 summarizes the results of the constant flow-through tests that were conducted at effective stress of 0.55 MPa (80 psi). It includes each specimen's original depth, bedding dip, horizontal and vertical hydraulic conductivity, horizontal and vertical intrinsic permeability, and ratio of horizontal to vertical permeability. Table A1 (Appendix) contains the results from each individual test, including volumetric flow rate, discharge velocity, steady-state head difference, steady-state hydraulic gradient, hydraulic conductivity, and intrinsic permeability for each test. Figures A1 to A22 (Appendix) show the relation between steady stead hydraulic gradient and discharge velocity for each test. Table 6 summarizes the results from each microfabric analysis with number of counted grains, standard deviation of orientation, and index of microfabric orientation. Figure A23 (Appendix) contains all environmental SEM images. Table 7 includes the results of shipboard bulk sediment powder X-ray diffraction analyses that were performed during IODP Expeditions 316 (Sites C0004, C0006, C0007, and C0008), and 333 (Site C0011). Table 8 summarizes relative weight percentages of clay minerals in clay-size fraction and bulk for intervals next to permeability and fabric samples.

Table 4. Summary of specimen properties before and after permeability test, Sites C0004, C0008, C0006, C0007 and C0011. Horz = horizontal sample orientation, Vert = vertical sample orientation, Ht = height, Dia = diameter, *B* = Skempton's *B*-value, n = porosity, Wt = water content (Table 4 continues next page).

						Shipboard		Pre-test		Post-test	
			Sample Average (cm)								
Core, Section interval (cm)	Smpl Ori.	Depth mbsf	Ht.	Dia.	*B*	Grain Density (g/cm^3)	n	Wt. (%)	n	Wt. (%)	n
316-C0004C-											
6H-7, 16	Horz.	51.75	-	-	-	2.58	0.61	62.2	-	-	-
	Vert.		6.07	3.70	0.98			62.2	0.63	57.0	0.61
8H-5, 92	Horz.	68.75	4.93	4.81	0.98	2.36	0.56	67.2	0.65	53.1	0.59
	Vert.		5.36	3.98	0.99			60.3	0.62	54.2	0.59
316-C0004D-											
44R-2, 72	Horz.	343.60	-	-	-	2.74	0.47	37.9	-	-	-
	Vert.		3.33	4.14	0.96			37.9	0.51	37.5	0.50
52R-3, 112	Horz.	381.41	-	-	-	2.70	0.42	31.8	-	-	-
	Vert.		3.25	3.88	0.98			31.8	0.46	33.1	0.47
316-C0008A-											
17H-8, 25	Horz.	137.97	-	-	-	2.62	0.53	41.9	-	-	-
	Vert.		6.42	4.02	1.01			41.9	0.53	37.6	0.50
27H-2, 25	Horz.	211.95	-	-	-	2.74	0.50	46.5	-	-	-
	Vert.		5.50	4.10	0.97			46.5	0.56	45.1	0.55
316-C0006E-											
5H-1, 128	Horz.	34.49	5.06	4.21	1.00	2.65	0.48	28.1	0.43	28.0	0.43
	Vert.		4.91	6.95	0.95			28.0	0.43	28.0	0.43
7H-2, 117	Horz.	41.20	-	-	-	2.46	0.54	-	-	-	-
	Vert.		5.10	4.10	1.02			30.9	0.43	63.6	0.61
16X-1, 113	Horz.	89.95	4.32	3.91	0.95	2.72	0.45	24.4	0.40	25.5	0.41
	Vert.		5.27	6.36	0.94			23.9	0.39	22.0	0.37
20X-3, 1	Horz.	128.20	5.24	3.69	0.97	2.73	0.45	34.8	0.49	30.4	0.45
	Vert.		5.68	4.22	0.92			37.2	0.50	29.3	0.44
22X-6, 5	Horz.	150.19	3.54	3.78	0.97	2.71	0.40	28.6	0.44	24.2	0.40
	Vert.		5.56	4.01	0.94			28.2	0.43	23.7	0.39
26X-1, 126	Horz.	183.69	4.45	3.51	0.95	2.59	0.38	31.8	0.45	31.2	0.45
	Vert.		6.08	4.23	0.96			31.1	0.45	27.0	0.41
34X-3, 95	Horz.	262.09	4.17	4.21	0.95	2.64	0.40	22.9	0.38	22.6	0.37
	Vert.		7.96	6.33	0.99			28.8	0.43	24.9	0.40
39X-3, 48	Horz.	300.00	4.89	3.88	0.95	2.68	0.43	31.0	0.45	27.0	0.42
	Vert.		4.81	4.02	0.97			31.8	0.46	27.3	0.42
316-C0006F-											
19R-2, 61	Horz.	563.50	3.93	4.25	0.99	2.75	0.39	27.7	0.43	25.3	0.41
	Vert.		4.22	4.12	0.95			23.2	0.39	24.7	0.40

(Table 4 cont'd)

Core, Section interval (cm)	Smpl Ori.	Depth mbsf	Sample Average (cm) Ht.	Sample Average (cm) Dia.	*B*	Shipboard Grain Density (g/cm^3)	Shipboard n	Pre-test Wt. (%)	Pre-test n	Post-test Wt. (%)	Post-test n
316-C0007D-											
23R-2, 97	Horz.	382.00	3.64	3.79	0.95	2.68	0.49	38.6	0.51	40.8	0.52
	Vert.		6.71	5.73	1.01			29.5	0.44	39.2	0.51
25R-2, 66	Horz.	400.53	4.19	4.14	0.95	2.73	0.49	35.3	0.49	38.0	0.51
	Vert.		8.56	5.72	1.01			35.3	0.49	38.0	0.51
333-C0011D-											
2H-7, 0	Horz.	36.23	5.37	3.67	0.95	2.49	0.61	67.3	0.65	56.7	0.61
	Vert.		5.83	3.84	0.96			74.3	0.67	62.2	0.63
19H-5, 99	Horz.	172.32	5.39	3.77	0.95	2.73	0.67	74.2	0.67	74.4	0.67
	Vert.		6.50	4.01	0.96			68.3	0.65	71.9	0.66
32X-6, 24	Horz.	246.03	-	-	-	3.05	0.69	-	-	-	-
	Vert.		-	-	-			-	-	-	-
41X-6, 121	Horz.	317.99	3.15	4.00	0.87	2.72	0.52	46.0	0.55	41.8	0.53
	Vert.		6.98	3.84	0.95			45.5	0.55	40.1	0.52
49X-4, 51	Horz.	362.58	3.49	4.12	0.89	2.68	0.52	48.5	0.57	38.3	0.51
	Vert.		7.03	5.84	0.96			49.1	0.57	37.8	0.51

Table 5. Average values of permeability and hydraulic conductivity, Sites C0004, C0008, C0006, C0007 and C0011.

Core, Section interval (cm)	Depth (mbsf)	Bed Dip (°)	Hydraulic Conductivity (cm/s)		Intrinsic Permeability (m^2)		Permeability Ratio (H/V)
			Horizontal	Vertical	Horizontal	Vertical	
316-C0004C-							
6H-7, 16	51.75	-	-	1.11E-08	-	1.13E-17	-
8H-5, 92	68.75	8	1.00E-08	1.58E-08	1.02E-17	1.61E-17	0.63
316-C0004D-							
44R-2, 72	343.60	-	-	9.32E-09	-	9.51E-18	-
52R-3, 112	381.41	-	-	1.82E-09	-	1.86E-18	-
316-C0008A-							
17H-8, 25	137.97	4	-	6.56E-09	-	6.69E-18	-
27H-2, 25	211.95	0	-	1.10E-08	-	1.12E-17	-
316-C0006E-							
5H-1, 128	34.49	43	8.25E-07	4.33E-07	8.42E-16	4.42E-16	1.91
7H-2, 117	41.20	46	-	7.79E-08	-	7.95E-17	-
16X-1, 113	89.95	31	2.07E-06	1.04E-07	2.11E-15	1.06E-16	19.90
20X-3, 1	128.20	38	3.20E-09	1.71E-09	3.27E-18	1.74E-18	1.87
22X-6, 5	150.19	44	3.72E-08	1.60E-06	3.80E-17	1.63E-15	0.02
26X-1, 126	183.69	9	4.29E-09	3.64E-09	4.38E-18	3.71E-18	1.18
34X-3, 95	262.09	14	2.20E-09	1.24E-09	2.24E-18	1.27E-18	1.77
39X-3, 48	300.00	5	1.46E-07	2.34E-08	1.49E-16	2.39E-17	6.24
316-C0006F-							
19R-2, 61	563.50	-	3.25E-10	2.63E-10	3.32E-19	2.68E-19	1.24
316-C0007D-							
23R-2, 97	382.00	3	1.15E-09	9.54E-10	1.17E-18	9.73E-19	1.21
25R-2, 66	400.53	4	8.09E-10	1.24E-09	8.26E-19	1.27E-18	0.65
333-C0011D-							
2H-7, 0	36.43	10	1.76E-08	1.31E-08	1.80E-17	1.34E-17	1.34
19H-5, 99	172.48	25	1.11E-08	1.07E-08	1.13E-17	1.09E-17	1.04
32X-6, 24	246.32	-	-	-	-	-	-
41X-6, 121	318.19	5	6.57E-10	3.70E-10	6.70E-19	3.78E-19	1.78
49X-4, 51	362.74	5	5.05E-10	2.77E-10	5.15E-19	2.83E-19	1.82

Table 6. Fabric orientation statistics calculated from analyses of environmental SEM images, Sites C0004, C0008, C0006, C0007 and C0011. SD = standard deviation.

Core, section interval (cm)	Depth mbsf	Horizontal Section			Vertical Section		
		Grains counted	SD of orientation (°)	Index of orientation	Grains counted	SD of orientation (°)	Index of orientation
316-C0004C-							
6H-7, 16	51.75	562	53.7	0.27	706	49.1	0.32
8H-5, 92	68.75	269	56.4	0.22	154	56.1	0.22
316-C0004D-							
44R-2, 72	343.60	115	58.5	0.19	192	57.8	0.20
52R-3, 112	381.41	125	53.5	0.26	133	59.6	0.18
316-C0008A-							
17H-8, 25	137.97	89	57.9	0.20	113	51.8	0.28
27H-2, 25	211.95	173	57.5	0.20	131	56.9	0.21
316-C0006E-							
5H-1, 128	34.49	252	53.5	0.26	232	53.5	0.26
7H-2, 117	41.20	200	53.1	0.27	341	30.5	0.58
16X-1, 113	89.95	391	50.3	0.30	258	38.8	0.46
20X-3, 1	128.20	433	54.6	0.25	217	38.3	0.47
22X-6, 5	150.19	192	49.4	0.32	500	43.1	0.40
26X-1, 126	183.69	393	55.8	0.23	423	59.4	0.18
34X-3, 95	262.09	293	51.4	0.29	212	52.7	0.27
39X-3, 48	300.00	640	56.5	0.22	275	50.1	0.31
316-C0006F-							
19R-2, 61	563.50	361	51.1	0.29	500	54.4	0.25
316-C0007D-							
23R-2, 97	382.00	315	51.6	0.29	290	50.1	0.31
25R-2, 66	400.53	264	48.8	0.32	450	43.0	0.40
333-C0011D-							
2H-7, 0	36.43	230	59.8	0.17	154	56.5	0.22
19H-5, 99	172.48	128	56.0	0.23	224	55.7	0.23
32X-6, 24	246.32	162	57.6	0.20	139	58.0	0.20
41X-6, 121	318.19	131	56.8	0.22	179	57.8	0.20
49X-4, 51	362.74	113	56.6	0.22	117	53.3	0.26

Table 7. Shipboard analysis of bulk sediment's relative weight percentages of total clay, quartz, plagioclase, and calcite. Imported data belong the samples that were used in this study. tr = trace mineral (Expedition 316 Scientists, 2009a; Expedition 316 Scientists, 2009b; Expedition 316 Scientists, 2009c; Expedition 316 Scientists, 2009d; Expedition 333 Scientists, 2011).

		Relative abundances (wt%)			
Core, Section, interval (cm)	Depth mbsf	Total clay minerals	Quartz	Plagioclase	Calcite
316-C0004C-					
6H-7, 15	51.76	52.5	17.6	13.3	16.7
8H-5, 91	68.76	47.9	18.0	23.2	10.9
316-C0004D-					
44R-2, 71	343.61	47.0	20.7	28.1	4.2
52R-3, 110.5	381.41	55.2	20.3	24.5	tr
316-C0008A-					
17H-8, 23.5	137.97	51.2	26.6	21.7	0.4
27H-2, 35	212.05	49.1	21.0	27.8	2.2
316-C0006E-					
5H-1, 126.5	34.49	50.6	22.3	27.1	tr
7H-2, 115.5	41.25	29.3	26.2	44.5	tr
16X-1, 96.5	89.80	44.5	23.1	32.4	tr
20X-3, 0	128.16	49.4	26.1	24.5	tr
22X-6, 20	150.20	38.9	26.6	34.4	tr
26X-1, 147.5	183.81	46.8	24.0	29.2	tr
34X-3, 94	262.09	48.8	24.2	27.0	tr
39X-3, 71	309.36	52.8	22.8	24.4	tr
316-C0006F-					
19R-2, 78.5	563.69	62.7	21.5	15.9	tr
316-C0007D-					
23R-2, 113	382.04	67.0	18.4	14.5	tr
25R-2, 80	400.73	63.1	18.0	18.9	tr
333-C0011D-					
2H-7, 20	36.43	49.0	17.0	17.0	17.0
19H-5, 119	172.48	65.0	20.0	15.0	tr
32X-6, 23	246.32	64.0	20.0	15.0	tr
41X-6, 120	318.19	70.0	16.0	9.0	5.0
49X-4, 50	362.74	71.0	16.0	12.0	tr

Table 8. Relative weight percentages of clay minerals in clay-size fraction and bulk (Guo and Underwood, 2011a). S = Smectite, I = Illite, K = Kaolinite, C = Chlorite.

Core, Section, interval (cm)	Depth (mbsf)	Relative abundance in clay-size (wt%)				Total clay minerals	Relative abundance in bulk (wt%)			
		S	I	K	C	(Bulk)	S	I	K	C
316-C0004C-										
6H-7, 15	51.76	44	31	5	17	53	45	32	5	18
8H-5, 91	68.76	34	34	5	17	48	38	37	6	19
316-C0004D-										
44R-2, 71	343.61	36	32	2	20	47	40	35	3	23
52R-3, 110.5	381.41	41	32	5	18	55	43	33	5	19
316-C0008A-										
17H-8, 23.5	137.97	27	38	7	20	51	30	41	8	21
27H-2, 35	212.05	33	32	6	20	49	36	35	7	22
316-C0006E-										
5H-1, 126.5	34.49	28	33	2	28	51	31	37	2	31
7H-2, 115.5	41.25	22	36	3	30	29	24	40	3	33
16X-1, 96.5	89.80	23	37	3	30	45	24	40	4	32
20X-3, 0	128.16	16	45	0	30	49	17	49	0.3	33
22X-6, 20	150.20	23	35	4	31	39	25	38	4	34
26X-1, 147.5	183.81	30	32	5	26	47	32	34	5	28
34X-3, 94	262.09	35	33	3	23	49	37	35	4	25
39X-3, 71	309.36	26	34	2	30	53	28	37	2	33
316-C0006F-										
19R-2, 78.5	563.69	33	39	5	16	63	35	42	6	17
316-C0007D-										
23R-2, 113	382.04	41	37	5	14	67	41	38	5	15
7H-2, 115.5	400.73	38	34	9	14	63	40	36	9	15
333-C0011D-										
2H-7, 20	36.43	29	40	7	16	49	31	44	8	17
19H-5, 99	172.48	29	38	6	17	65	32	42	7	19
32X-6, 23	246.32	38	37	8	12	64	40	39	9	12
41X-6, 120	318.19	45	30	2	17	70	48	32	2	18
49X-4, 50	362.74	40	40	3	9	71	43	44	3	10

4.1. Results from Megasplay Fault Zone

Samples from Site C0004 were taken from depths between 51.75 m and 381.41 m below the sea floor (Fig. 23); they include lithostratigraphic Unit I (slope sediments) and Unit IV (underthrust slope sediments). The highest value of vertical hydraulic conductivity is 1.58E-08 cm/s, whereas the highest value of vertical permeability is 1.61E-17 m^2. This sample (316-C0004C-8H-5, 91 cm) from Unit I (slope apron) was taken at depth of 68.75 mbsf. According to shipboard measurement, it has 56% porosity. However, the post-test water content measurement shows that its porosity is 59%. It is associated with 8º bedding dip. 154 grains were counted from its environmental SEM image, corresponding with standard deviation of orientation and index of orientation of 56.1º and 0.22 respectively. Expedition 316 Scientists (2009d) reported it includes 48% total clay, 18% quartz, 23% plagioclase, and 11% calcite by weight in bulk powder sediment. Clay mineralogy analyses show that it has 38% smectite, 37% illite, 6% kaolinite, and 19% chlorite in bulk sediment.

The lowest value of vertical hydraulic conductivity is 1.82E-09 cm/s, and the lowest value of vertical permeability is 1.86E-18 m^2. This sample (316-C0004D-52R-3, 112 cm) from Unit IV (underthrust slope sediments) was taken at depth of 381.41 mbsf. According to shipboard measurement, it has 42% porosity. But, the post-test water content measurement shows that its porosity is 47% (Table 4). There is no such datum shows its bedding dip. 133 grains were counted from its environmental SEM image, corresponding with standard deviation of orientation and index of orientation of 59.6º and 0.18 respectively (Table 6). Expedition 316 Scientists (2009d) reported it includes 55% total clay, 20% quartz, and 25% plagioclase by weight, whereas calcite was reported as

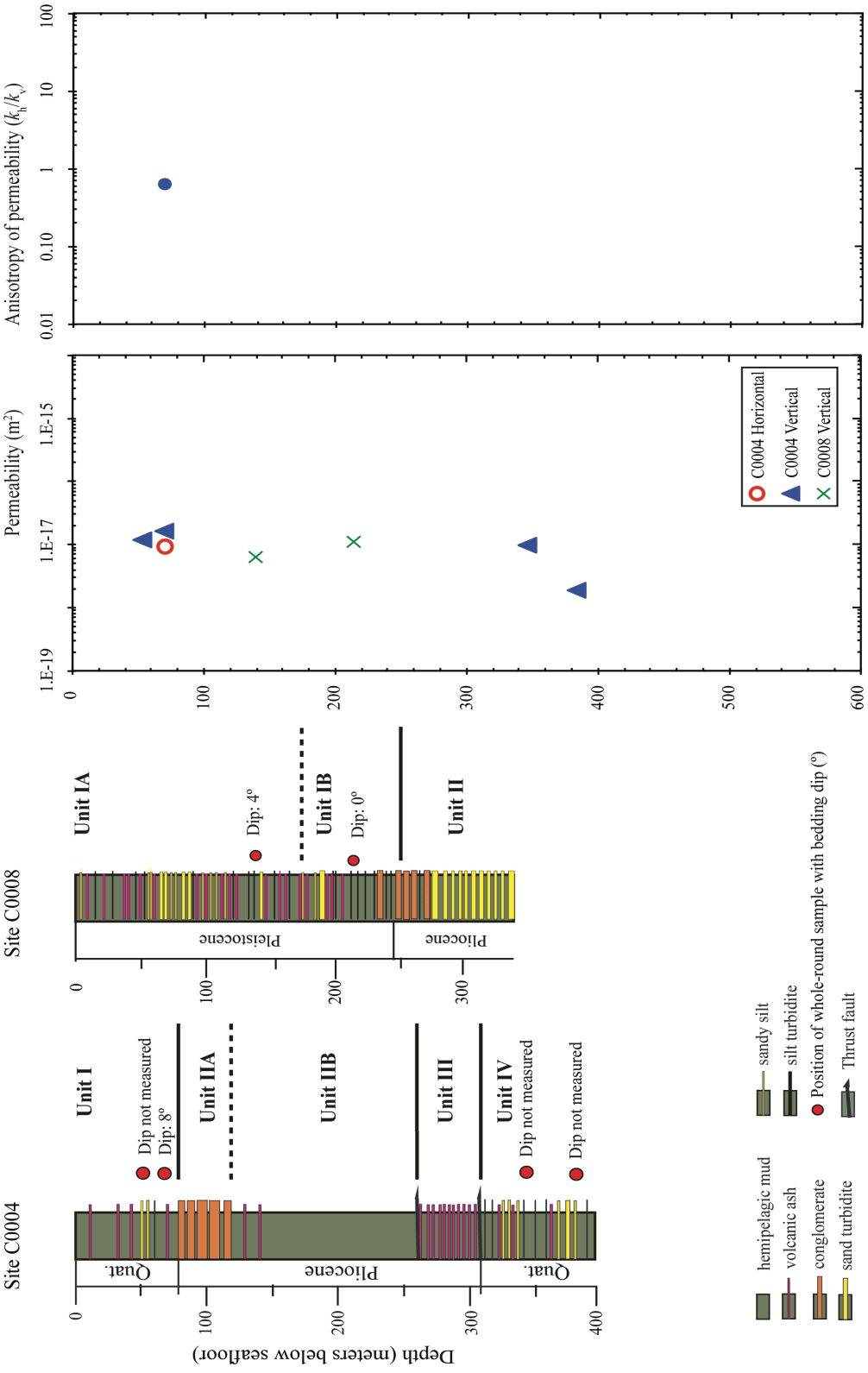

Figure 23. Values of vertical and horizontal permeability, and anisotropy of intrinsic permeability versus depth, Sites C0004 and C0008, measured at an effective stress of 0.55 MPa. Vertical scale, 2 cm = 100 meters.

trace mineral in bulk powder sediment (Table 7). Clay mineralogy analyses show that it has 43% smectite, 33% illite, 5% kaolinite, and 19% chlorite in bulk sediment (Table 8).

Only one specimen (316-C0004C-8H-5, 91 cm) could be trimmed for horizontal flow-through test because of insufficient sample size. The measured horizontal hydraulic conductivity is 1.00E-08 cm/s, whereas the corresponding permeability value is 1.02E-17 m^2. The ratio of horizontal to vertical permeability is 0.63 (Table 5). Figure 22 shows how vertical and horizontal permeability values, together with the corresponding k_h/k_v ratio, change as the sampling depth increases. Values of vertical permeability decrease with increasing depth. Porosity values also decrease with burial depth.

Standard deviations of orientation and the indexes of orientation are consistent with highly random arrangements of particles. Indexes of orientation are typically greater for the vertical section than for the horizontal section. The illustrations that shows relations between permeability anisotropy, microfabric orientation index and orientation index ratio were omitted because of the number of samples tested. Interpretation of these results, however, needs to take the dip of bedding into account. For one sample from Site C0004, the bed dips at angle of 8º.

Samples from Site C0008 came from 137.97 and 211.95 m below sea floor; both are from lithostratigraphic Unit I, slope apron facies. The highest value of vertical hydraulic conductivity is 1.10E-08 cm/s, and the highest value of vertical permeability is 1.12E-17 m^2. This sample (316-C0008A-27H-2, 25 cm) was taken at depth of 211.95 mbsf. According to shipboard measurement, its porosity is 50%. However, the post-test water content measurement shows that its porosity is 55% (Table 4). It is associated with 0º bedding dip. 131 grains were counted from its environmental SEM image,

corresponding with standard deviation of orientation and index of orientation of 56.9º and 0.21 respectively (Table 6). Expedition 316 Scientists (2009c) reported it includes 49% total clay, 21% quartz, 28% plagioclase, and 2% calcite by weight in bulk powder sediment (Table 7). Clay mineralogy analyses show that it has 36% smectite, 35% illite, 7% kaolinite, and 22% chlorite in bulk sediment (Table 8).

The lowest value of vertical hydraulic conductivity is 6.56E-09 cm/s, whereas the lowest value of vertical permeability is 6.69E-18 m^2. This sample (316-C0008A-17H-8, 23.5 cm) was taken at depth of 137.97 mbsf. According to shipboard measurement, it has 53% porosity. However, the post-test water content measurement shows that its porosity is 50% (Table 4). It is associated with 4º bedding dip. 113 grains were counted from its environmental SEM image, corresponding with standard deviation of orientation and index of orientation of 51.8º and 0.28 respectively (Table 6). Expedition 316 Scientists (2009c) reported it includes 51% total clay, 27% quartz, 22% plagioclase, and 0.4% calcite by weight in bulk powder sediment (Table 7). Clay mineralogy analyses show that it has 30% smectite, 41% illite, 8% kaolinite, and 21% chlorite in bulk sediment (Table 8). Figure 22 displays how the vertical permeability value increases a small amount as the sampling depth increases. Porosity values also decrease with burial depth.

The standard deviation of orientation and the indexes of orientation are consistent with highly random arrangements of particles. Indexes of orientation and steep of cumulative slopes are greater for both of the two vertical sections. The beds dip at angles of 4º and 0º (Fig. 24; Fig. 25).

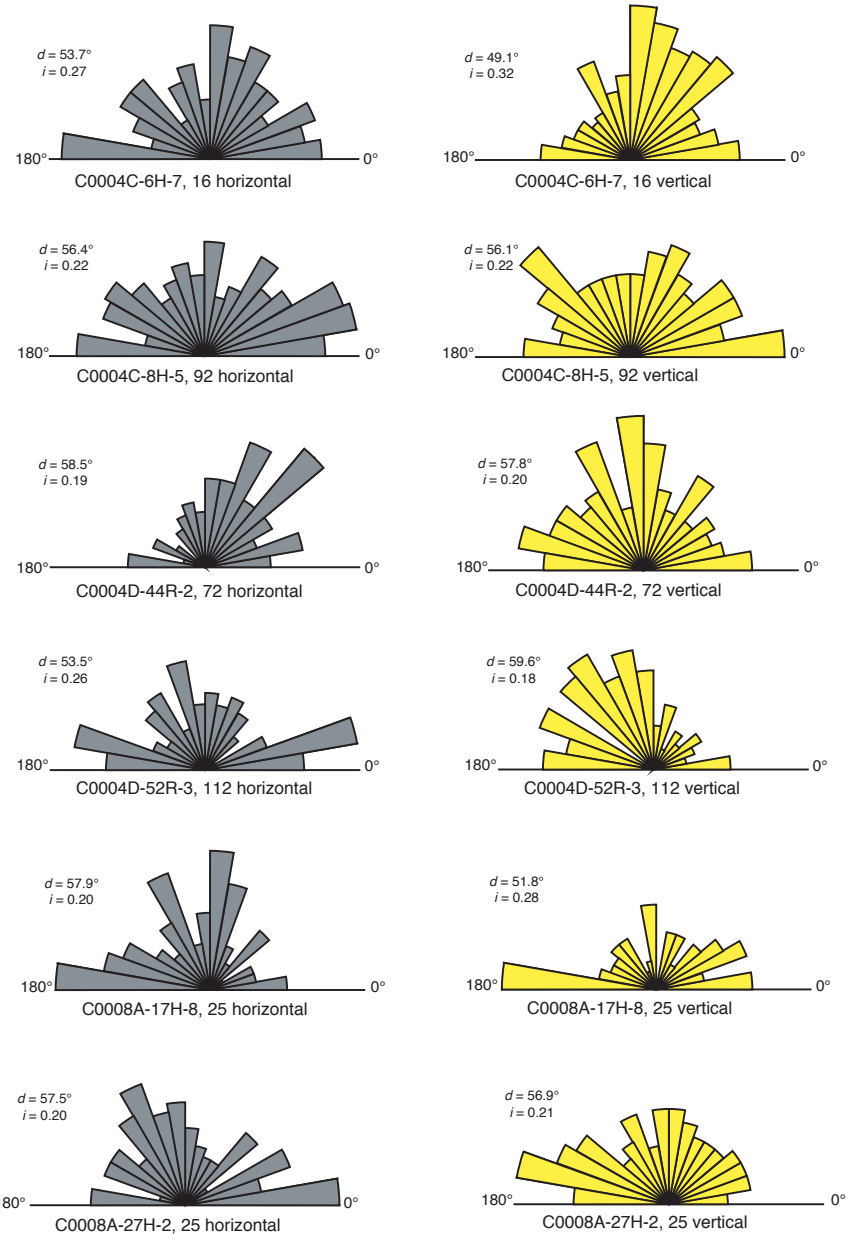

Figure 24. Rose diagrams showing orientation of grains (apparent long axis) measured on environmental scanning electron microscopy images from cut parallel (vertical) and perpendicular (horizontal) to the core axis. Values of standart deviation (*d*) for grain orientation and microfabric orientation index (*i*) are shown.

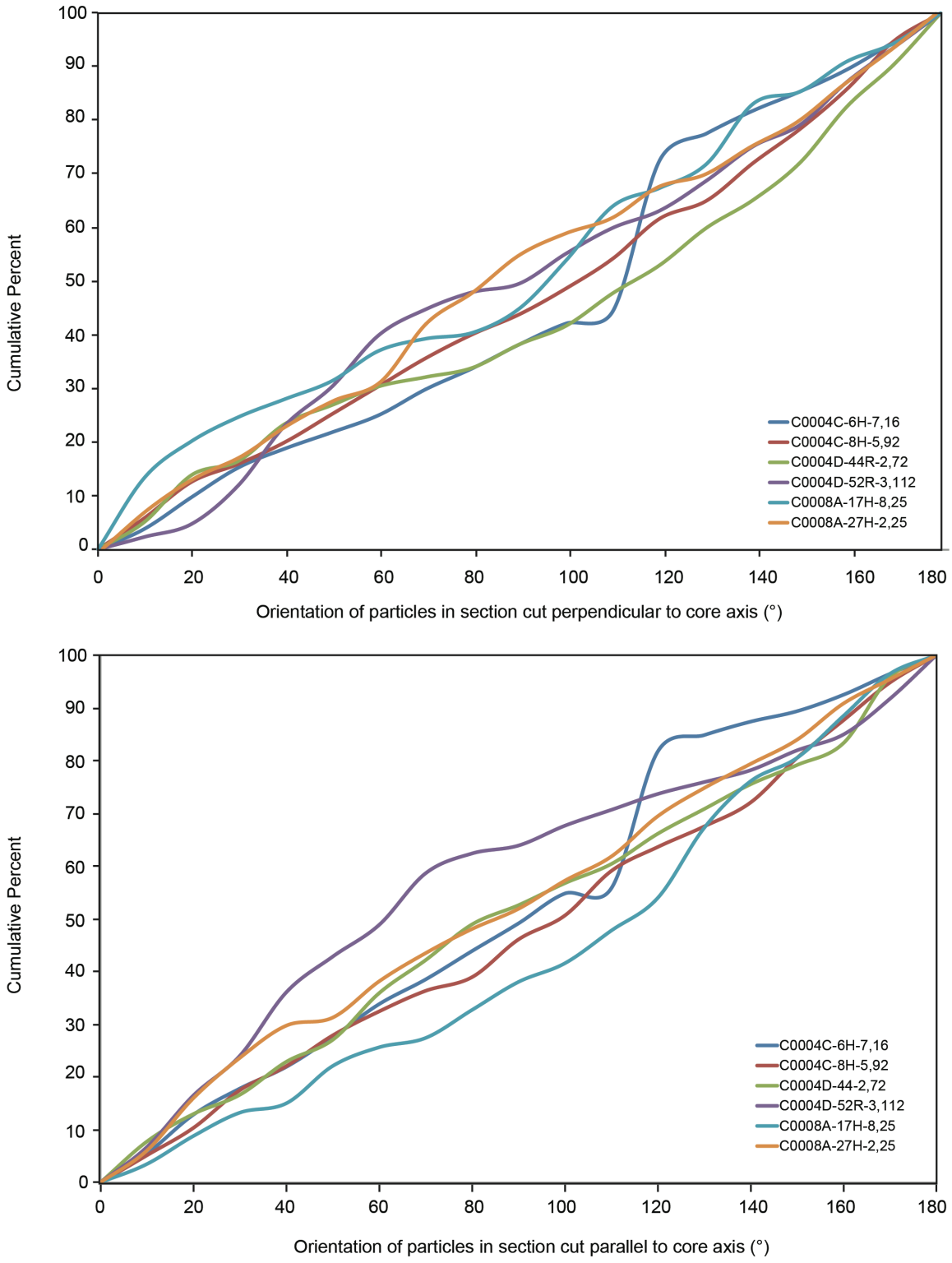

Figure 25. Cumulative frequency curves for grain orientation imaged on (A) horizontal section (perpendicular to core axis) and (B) vertical section (parallel to core axis) by environmental scanning electron microscopy, Sites C0004 and C0008. Angles of orientation for the apparent long axes were grouped into bins of 10°.

4.2. Results from Frontal Thrust Zone

Samples from Site C0006 were taken from depths of 34.49 m to 563.50 m below sea floor (Fig. 26); they include lithostratigraphic Unit II (accreted trench wedge) and Unit III (upper Shikoku Basin facies). The highest value of vertical hydraulic conductivity is 1.60E-06 cm/s with corresponding intrinsic permeability 1.63E-15 m^2 (Table 2). This sample (316-C0006E-22X-6, 5 cm) was taken at depth of 150.19 mbsf (Unit II). According to shipboard measurement, its porosity is 40%. The post-test water content measurement also shows that its porosity is 40% (Table 4). It is associated with 44º bedding dip. 500 grains were counted from its environmental SEM image, corresponding with standard deviation of orientation and index of orientation of 43.1º and 0.40 respectively (Table 6). Expedition 316 Scientists (2009a) reported it includes 39% total clay, 27% quartz, and 34% plagioclase by weight and calcite was considered as trace mineral in bulk powder sediment (Table 7). Clay mineralogy analyses show that it has 25% smectite, 38% illite, 4.1% kaolinite, and 34% chlorite in bulk sediment (Table 8).

The lowest value of vertical hydraulic conductivity is 2.63E-10 cm/s with intrinsic permeability equal to 2.68E-19 m^2. This sample (316-C0006F-19R-2, 78.5 cm) was taken at depth of 563.50 mbsf (Unit III). According to shipboard measurement, its porosity is 39%. The post-test water content measurement shows that its porosity is 40% (Table 4). Bedding dip datum does not exist for this interval. 500 grains were counted from its environmental SEM image, corresponding with standard deviation of orientation and index of orientation of 54.4º and 0.25 respectively (Table 6). Expedition 316 Scientists (2009a) reported it includes 63% total clay, 22% quartz, and 16% plagioclase by weight and calcite was considered as trace mineral in bulk powder sediment (Table 7).

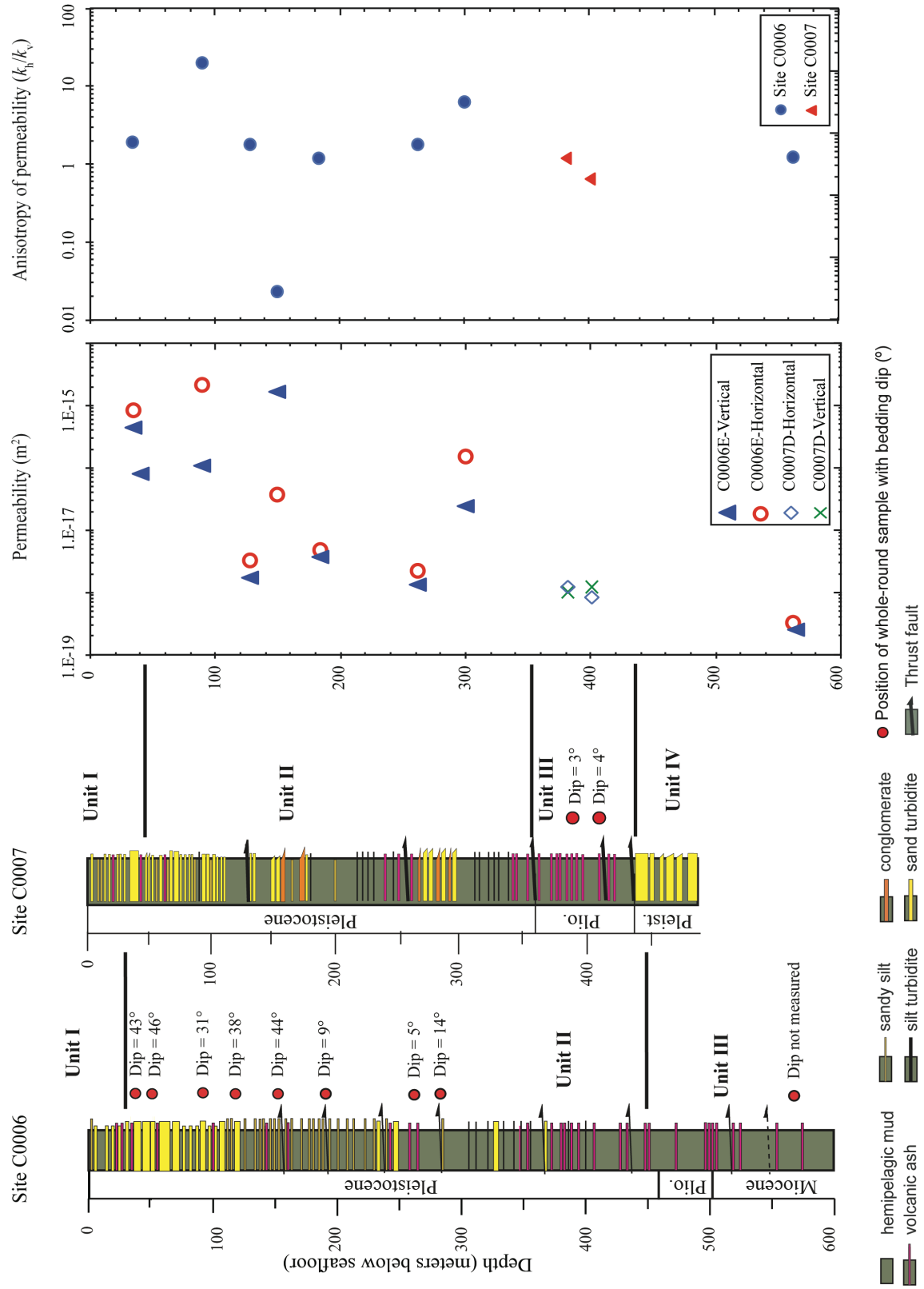

Figure 26. Values of vertical and horizontal permeability, and anisotropy ratio of intrinsic permeability versus depth, Sites C0006 and C0007, measured at an effective stress of 0.55 MPa. Vertical scale, 2 cm = 100 meters.

Clay mineralogy analyses show that it has 35% smectite, 42% illite, 6% kaolinite, and 17% chlorite in bulk sediment (Table 8).

The highest value of horizontal hydraulic conductivity is 2.07E-6 cm/s with intrinsic permeability equal to 2.11E-15 m^2. This sample (316-C0006E-16X-1, 113 cm) was taken at depth of 89.95 mbsf (Unit II). According to shipboard measurement, its porosity is 45% (Table 4). The post-test water content measurement also shows that its porosity is 41%. It is associated with 31º bedding dip. 391 grains were counted from its environmental SEM image, corresponding with standard deviation of orientation and index of orientation of 50.3º and 0.30 respectively (Table 6). Expedition 316 Scientists (2009a) reported it includes 45% total clay, 23% quartz, and 32% plagioclase by weight and calcite was considered as trace mineral in bulk powder sediment (Table 7). Clay mineralogy analyses show that it has 24% smectite, 40% illite, 4% kaolinite, and 32% chlorite in bulk sediment (Table 8).

The lowest value of horizontal hydraulic conductivity is 3.25E-10 cm/s with corresponding intrinsic permeability equal to 3.32E-19 m^2. This sample (316-C0006F-19R-2, 61 cm) has also the lowest value of vertical hydraulic conductivity as well.

The permeability ratio is generally greater than 1.0, ranging from 0.02 to 19.9 and average is 4.27 (Table 2). Figure 25 shows how vertical and horizontal permeability values, with corresponding k_h/k_v ratio, change as the sampling depth increases. Values of vertical and horizontal permeability both decrease with increasing depth except for one anomalous sample that was taken from 300 meters below sea floor (Sample 316-C0006E-39X-3, 48 cm). The anisotropy ratio for permeability shows a modest decreasing with depth and an anomalous result at ~150 mbsf (Sample 316-C0006E-22X-6, 5 cm).

Porosity values also decrease with burial depth.

The standard deviation for grain orientation ranges from 30.5° to 56.5°, and the index of orientation ranges from 0.18 to 0.58. With one exception, the standard deviation of orientation and the indexes of orientation are consistent with highly random arrangements of particles. Indexes of orientation are typically greater for the vertical section than for horizontal section. No clearly defined relation is apparent between the average indexes of microfabric orientation and depth of burial. Interpretation of these results, however, needs to take the dip of bedding into account, and for many samples the bedding dip angles >30º (Table 5). For example, even if beds of mudstone display a strong bedding-parallel fabric (e.g., shale fissility) but the dip is close to 45º.

Samples from Site C0007 came from depths of 382.00 m and 400.53 mbsf; they include lithostratigraphic Unit III (trench-basin transition deposits). The highest value of vertical hydraulic conductivity is 1.24E-09 cm/s with corresponding intrinsic permeability of 1.27E-18 m^2. The lowest value of vertical hydraulic conductivity is 9.54E-10 cm/s with intrinsic permeability equal to 9.73E-19 m^2. The highest value of horizontal hydraulic conductivity is 1.15E-09 cm/s with corresponding intrinsic permeability 1.17E-18 m^2, and the lowest value of horizontal hydraulic conductivity is 8.09E-10 cm/s with intrinsic permeability equal to 8.26E-19 m^2. In summary, the sample 316-C0007D-23R-2, 97 cm, which was taken from depth of 382 mbsf, shows higher horizontal permeability, but lower vertical permeability. According to shipboard measurement, its porosity is 49% (Table 4). It is associated with 3º bedding dip. 315 and 290 grains were counted for horizontal and vertical sections respectively from its environmental SEM image. Its standard deviation of orientation is 51.6º and index of

orientation 0.29 for horizontal section. For vertical section, values are 50.1º and 0.31 for standard deviation of orientation and index of orientation respectively (Table 6). Expedition 316 Scientists (2009b) reported it includes 67% total clay, 18% quartz, and 15% plagioclase by weight and calcite was considered as trace mineral in bulk powder sediment (Table 7). Clay mineralogy analyses show that it has 42% smectite, 38% illite, 5% kaolinite, and 15% chlorite in bulk sediment (Table 8).

In contrast, the sample 316-C0007D-25R-2, 80 cm, which came from depth at 400.73 mbsf, has higher vertical permeability, but lower horizontal permeability. According to shipboard measurement, its porosity is 49% (Table 4). It is associated with 4º bedding dip. 264 and 450 grains were counted for horizontal and vertical sections respectively from its environmental SEM image. Its standard deviation of orientation is 48.8º and index of orientation 0.32 for horizontal section. For vertical section, values are 43º and 0.40 for standard deviation of orientation and index of orientation respectively (Table 6). Expedition 316 Scientists (2009b) reported it includes 63% total clay, 18% quartz, and 19% plagioclase by weight and calcite was considered as trace mineral in bulk powder sediment (Table 7). Clay mineralogy analyses show that it has 40% smectite, 36% illite, 9% kaolinite, and 15% chlorite in bulk sediment (Table 8).

The anisotropy ratio for permeability ranges from 1.21 to 0.65 with a mean value 0.93 (Table 5). Figure 25 displays how vertical and horizontal permeability values, together with corresponding k_h/k_v ratio, change as the sampling depth increases. Values of vertical permeability increase while values of horizontal permeability decrease with increasing depth. The anisotropy ratio for permeability shows decrease with depth. Porosity values also decrease with burial depth.

The standard deviation for grain orientation ranges from 43.0° to 51.6°, and the index of orientation ranges from 0.29 to 0.40 (Table 6). Figure 27 displays rose diagrams of particle orientation and corresponding values for the standard deviation and index of orientation. These values are also tabulated in Table 4. Figure 28 shows all corresponding cumulative frequency curves for particle orientation. The standard deviation and the indexes of microfabric orientation are consistent with highly random arrangements of particle. Indexes of microfabric orientation and steep of cumulative slopes are typically greater for the vertical section than for the horizontal section. Frontal thrust Sites C0006 and C0007 exhibit higher orientation indexes and concomitant steeper cumulative slopes. No clearly defined relation is apparent between average indexes of microfabric orientation and depth of burial. The beds dip at angles of 3º and 4º.

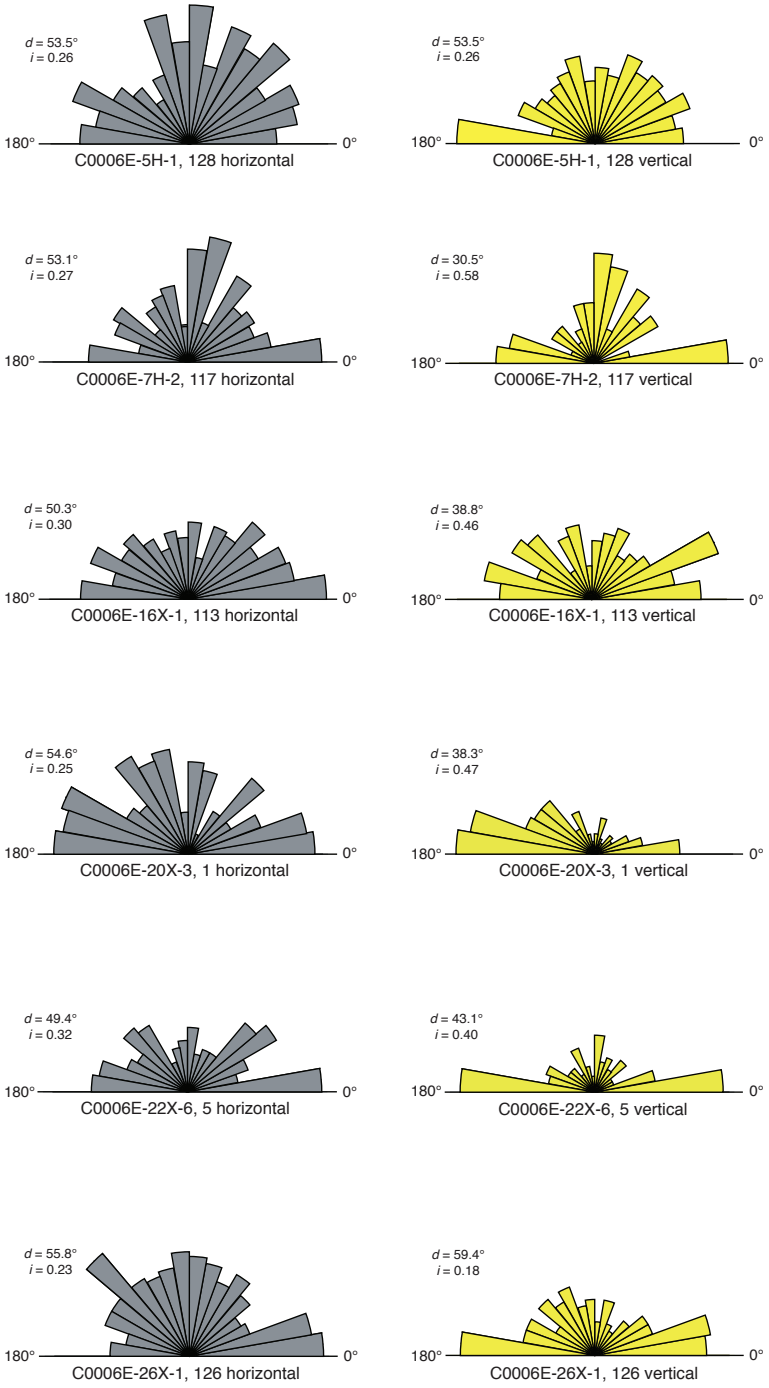

Figure 27. Rose diagrams showing orientation of grains (apparent long axis) measured on environmental scanning electron microscope images from section cut parallel and perpendicular to core axis. Values of standard deviation (*d*) for grain orientation and microfabric orientation index (*i*) are shown (Continue on next page).

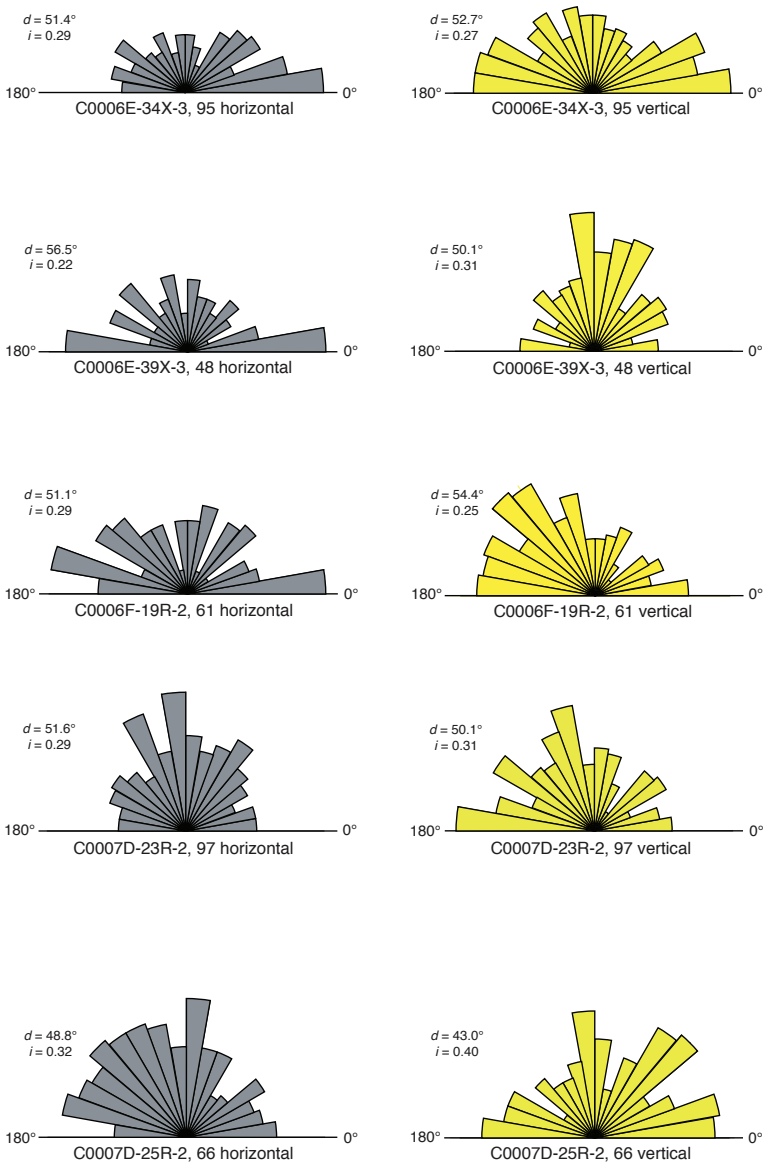

Figure 27. (Cont'd).

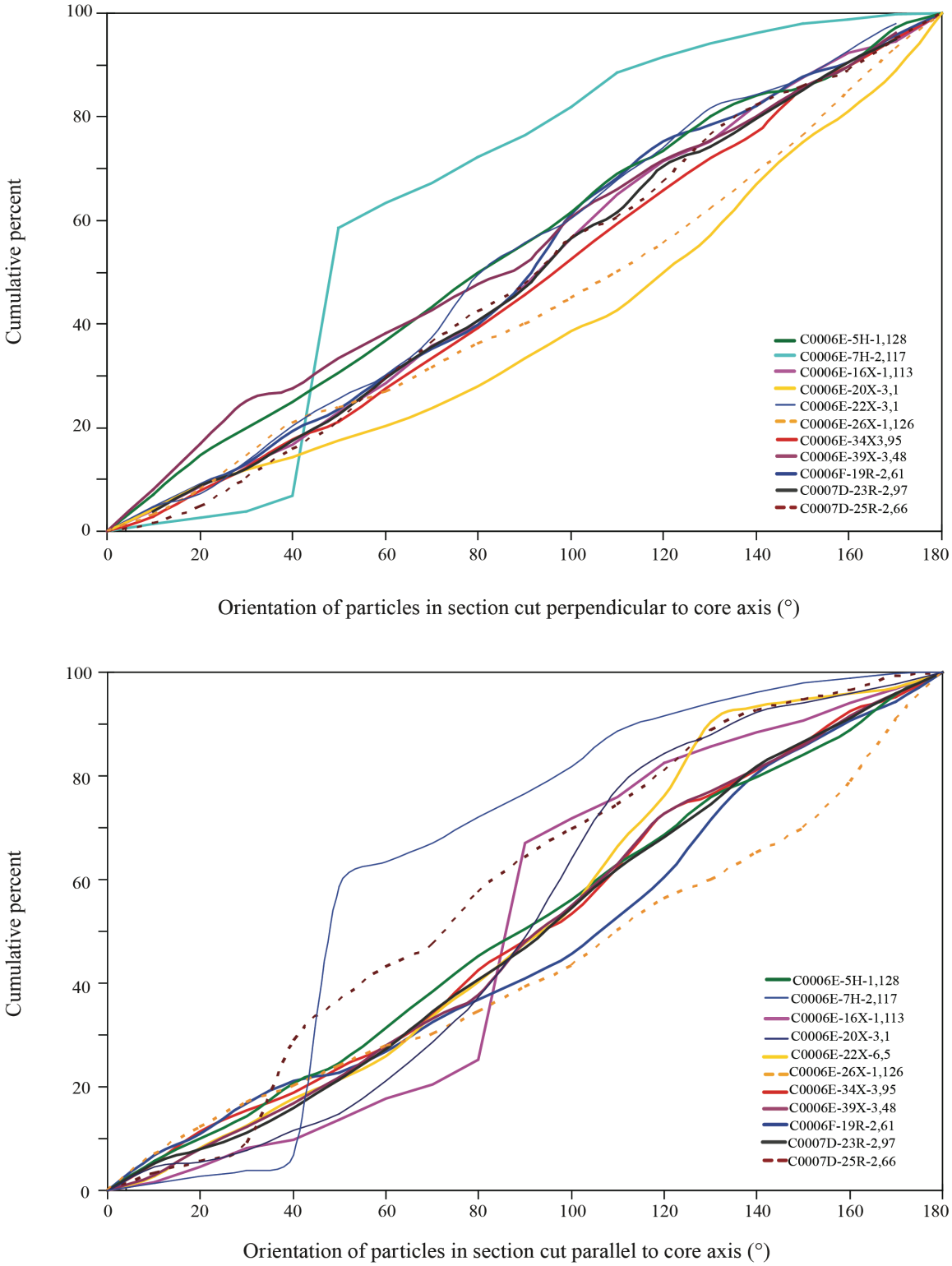

Figure 28. Cumulative frequency curves for grain orientation imaged on (A) horizontal section (perpendicular to core axis) and (B) vertical section (parallel to core axis) by environmental scanning electron microscopy, Sites C0006 and C0007. Angles of orientation for the apparent long axes were grouped into bins of 10°.

4.3. Results from Subduction Input Zone

Samples from Site C0011 came from depths of 36.43 m to 362.74 mbsf (Fig. 29); they include lithostratigraphic Unit I (hemipelagic/pyroclastic facies) and Unit II (volcanic turbidite facies). The highest value of vertical hydraulic conductivity is 1.31E-08 cm/s with corresponding intrinsic permeability of 1.34E-17 m^2. The lowest value of vertical hydraulic conductivity is 2.77E-10 cm/s with intrinsic permeability equal to 2.83E-19 m^2. The highest value of horizontal hydraulic conductivity is 1.76E-08 cm/s with intrinsic permeability equal to 1.80E-17 m^2. The lowest value of horizontal hydraulic conductivity is 5.05E-10 cm/s with corresponding intrinsic permeability equal to 5.15E-19 m^2.

The sample 333-C0011D-2H-7, 0 cm, which was taken from depth of 36.43 mbsf (Unit I), has the highest values of both vertical and horizontal permeability. According to shipboard measurement, it has 61% porosity. Likewise, the post-test water content measurement shows that its porosity is 61% (Table 4). It is associated with 10º bedding dip. Results of microfabric analyses show that 230 grains were counted for horizontal section, and 154 grains for vertical section from its environmental SEM image. For horizontal section, the standard deviation of microfabric orientation and the index of orientation of 59.8º and 0.17 respectively. For vertical section, the standard deviation of microfabric orientation and the index of orientation of 56.5º and 0.22 respectively (Table 6). Expedition 333 Scientists (2011) reported it includes 49% total clay, 17% quartz, 17% plagioclase, and 17% calcite by weight in bulk powder sediment (Table 7). Clay mineralogy analyses show that it has 31% smectite, 44% illite, 8% kaolinite, and 17% chlorite in bulk sediment (Table 8).

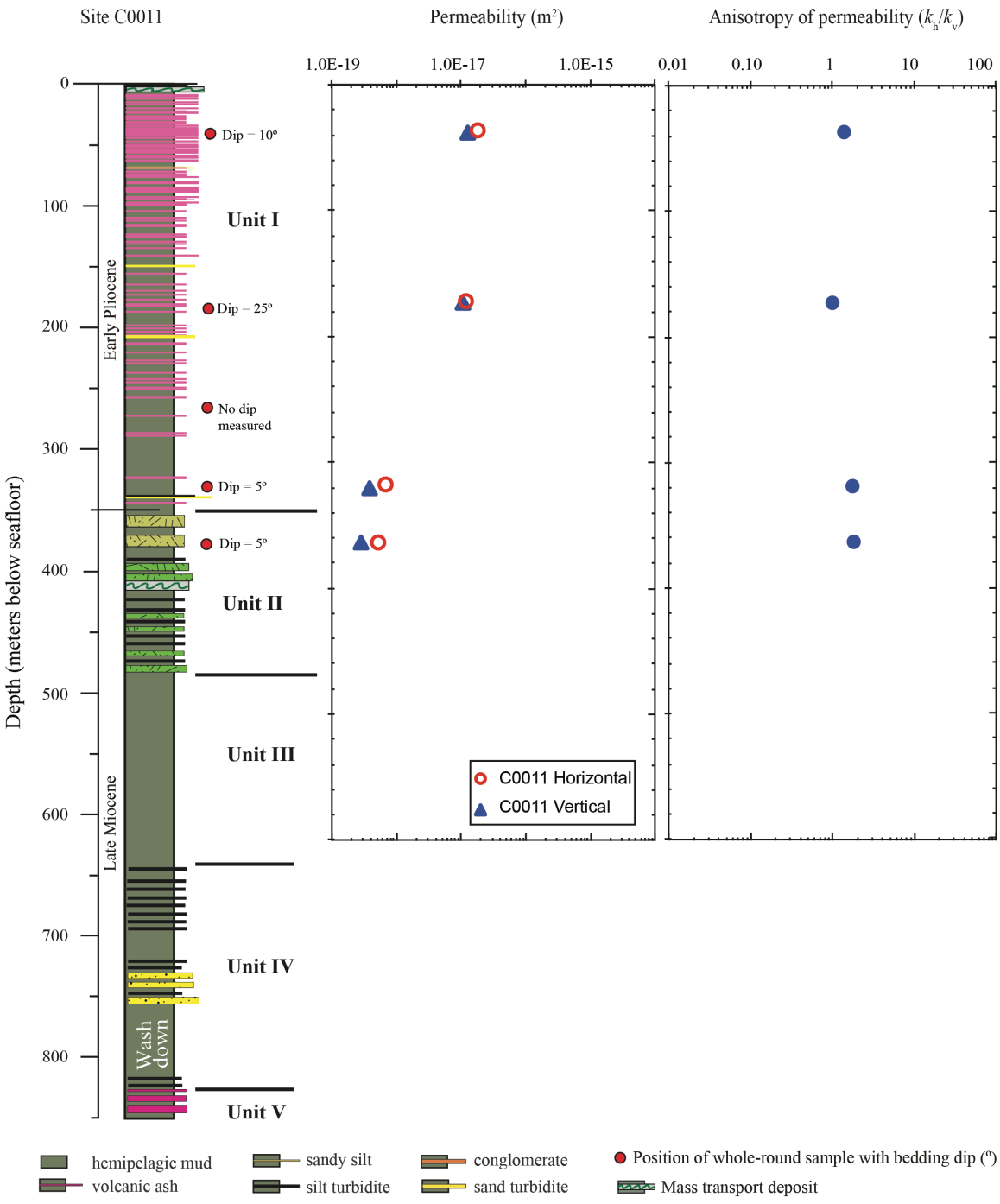

Figure 29. Values of vertical and horizontal permeability, and anisotropy ratio of intrinsic permeability versus depth, Site C0011, measured at an effective stress of 0.55 MPa. Vertical scale, 2 cm = 100 meters.

The sample 333-C0011D-49X-4, 51 cm, which was taken from depth of 362.74 mbsf (Unit II), has the lowest values of both vertical and horizontal permeability. According to shipboard measurement, it has 52% porosity. The post-test water content measurement shows that its porosity is 51%. It is associated with 5º bedding dip. Results of microfabric analyses show that 113 grains were counted for horizontal section, and 117 grains for vertical section from its environmental SEM image. For horizontal section, the standard deviation of microfabric orientation and the index of orientation of 56.6º and 0.22 respectively. For vertical section, the standard deviation of microfabric orientation and the index of orientation of 53.3º and 0.26 respectively. Expedition 333 Scientists (2011) reported it includes 71% total clay, 16% quartz, and 12% plagioclase by weight, whereas calcite is trace mineral in bulk powder sediment (Table 7). Clay mineralogy analyses show that it has 43% smectite, 44% illite, 3% kaolinite, and 10% chlorite in bulk sediment (Table 8). Relative mineral abundances in both clay-size fraction and bulk, below Unit I, show large variations in %-smectite.

The anisotropy ratio for permeability ranges between 1.82 and 1.04, whereas the permeability anisotropy values are greater than 1.0. The average value of the permeability anisotropy is 1.49 (Table 5). Figure 28 displays how vertical and horizontal permeability values, together with the corresponding k_h/k_v ratio, change as the sampling depth increase. Values of vertical and horizontal permeability both decrease with increasing depth. The anisotropy ratio for permeability shows a modest increase with depth. Porosity values also decrease with burial depth.

The standard deviation for grain orientation ranges from 53.3° to 59.8°, and the index of orientation ranges from 0.17 to 0.26 (Table 4). Figure 30 displays rose diagrams

of particle orientation and corresponding values for the standard deviation and index of orientation. These values are also tabulated in Table 6. Figure 31 shows all corresponding cumulative frequency curves for particle orientation. The standard deviations of microfabric orientation and the indexes of microfabric orientation are consistent with highly random arrangements of particles.

Indexes of orientation are typically greater for the vertical section than for horizontal section. No clearly defined relation is apparent between the average indexes of microfabric orientation and depth of burial. Interpretation of these results, however, needs to take the dip of bedding into account, and for many samples the bedding dip angles >10º (Table 5), except one sample, 333-19H-5, 99 cm. This sample, was taken from depth of 172.48 mbsf, has a bedding dip angel of 25º. Also, it has the lowest value of the anisotropy ratio for permeability.

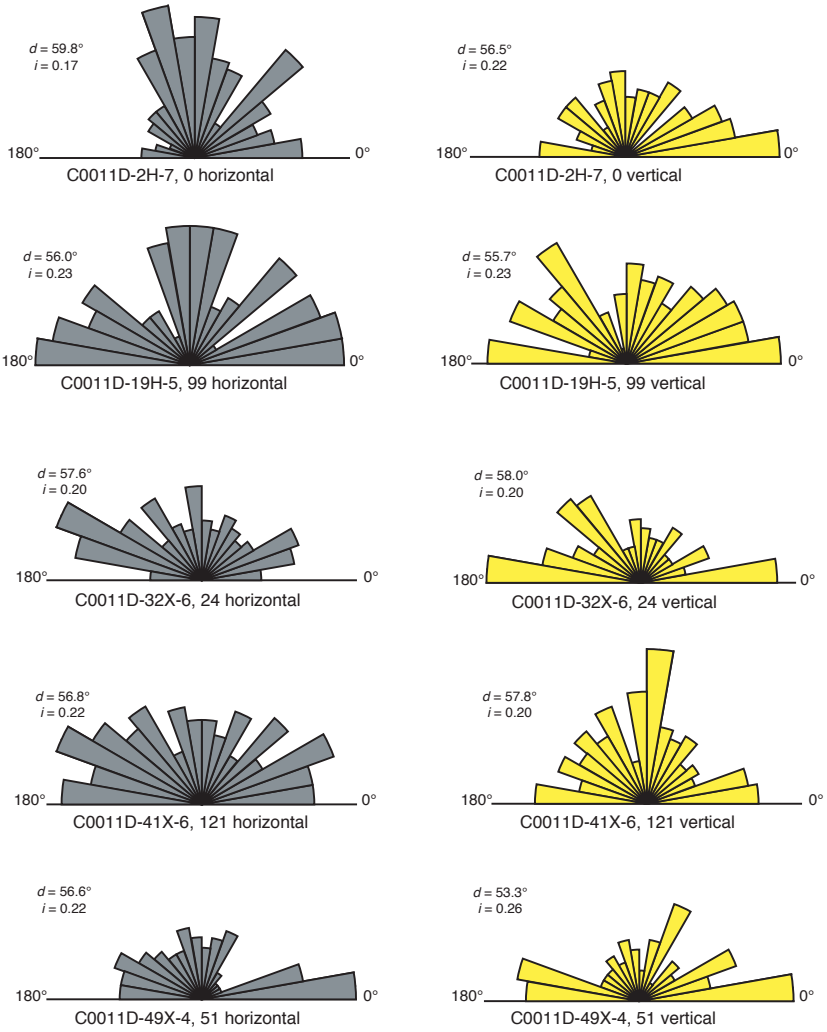

Figure 30. Rose diagrams for grain orientation (apparent long axis) measured on environmental scanning electron microscope images from section cut vertical and horizontal. Values of standard deviation (*d*) for grain orientation and microfabric orientation index (*i*) are shown.

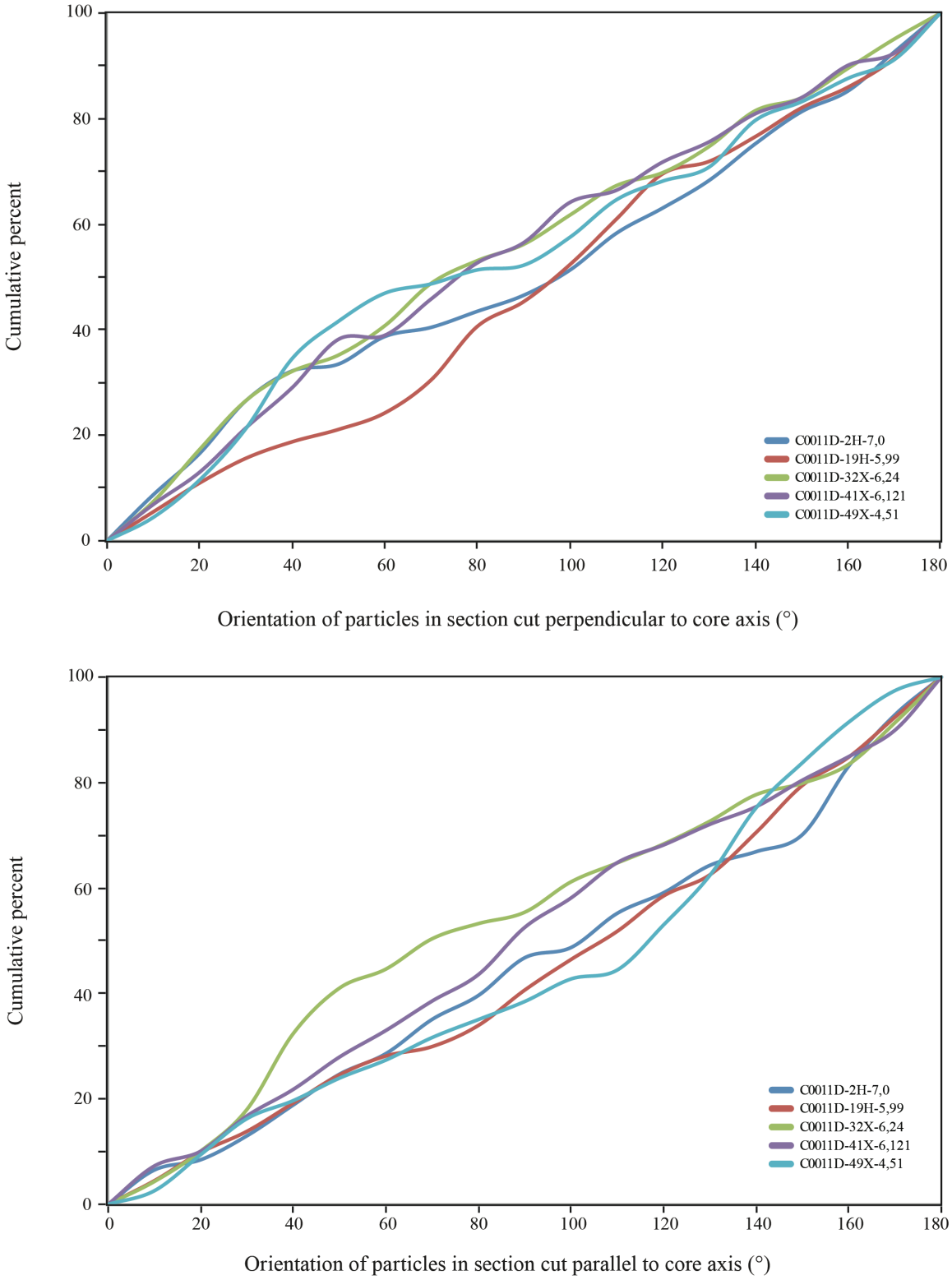

Figure 31. Cumulative frequency curves for grain orientation imaged on (A) horizontal section (perpendicular to core axis) and (B) vertical section (parallel to core axis) by environmental scanning electron microscopy, Site C0011. Angles of orientation for the apparent long axes were grouped into bins of 10°.

5. DISCUSSION

Taylor and Fisher (1993) measured the permeability of samples from ODP Site 808. The Site 808 is situated at the toe of the Nankai accretionary prism, along the Muroto transect. The sediment within the upper part of this prism extends 0 to ~618 mbsf and is dominated by clastic material transported by turbidity currents that flowed southwestward alogn the Nankai Trough from the collision zone between Japan and the Izu-Bonin arc. The lower part of the prism, below depth of ~618 mbsf, is formed from hemipelagic sediments deposited on the oceanic crust of the Shikoku Basin. The décollement extends from ~945 to 964 mbsf. As reported, the constant-head and constant-flow methods were used. A pressured system was used at pressures between 140-275 kPa (20-40 psi). The indirect measurements, which are directly linked to sediment stress-strain behavior, consist of the rate of response of sediment to an imposed stress and depend, in part, on the ability of fluid to leave or enter the particulate system. As a result, the sedimentary Units I and II, extend from 0 to ~556 mbsf, have quite variable and locally higher permeability because of uncemented sand layers. The vertical permeability ranges between 1.58E-14 and 5.89E-15 m^2 at the confining pressure of 140 kPa (20 psi). However, the values gradually decrease from 10^{-16} m^2 at 320 mbsf to 10^{-17} m^2 above the décollement. Below the décollement, both k_v and k_h generally increase with depth, are about 10^{-17} m^2. The lowest coefficient of permeability is 10^{-19} m^2 for sample from 1014 mbsf. The permeability anisotropy varies as burial depth increases, with horizontal permeability higher relative to vertical permeability.

Byrne et al. (1993) also reported results of permeability measurements for samples from ODP Site 808. Samples were taken from depths of 43 to 1262 mbsf. The

tests were conducted under effective stresses of 1 to 5 MPa. The indirect permeability measurement was used. Results show that a shallower sample (from 196 mbsf) has a permeability value of 3E-16 m^2, while the more deeply buried sample (from 347 mbsf) gives a value of 3E-18 m^2.

Gamage and Screaton (2003) and Adatia et al. (2004) documented the results of permeability measurements of samples from ODP Sites 1173 and 1174, along the Muroto transect. Site 1173 was drilled in the trench outer margin in order to provide reference for the pre-deformation status of geological and geochemical characteristics of the incoming sedimentary section. Coring at ODP Sites 1173 and 1174 recovered a sequence of upper and lower Shikoku Basin facies (Mikada et al., 2002). Gamage and Screaton (2003) reported that the measured samples from Site 1173 ranged in depth from 199.9 to 428.6 mbsf with lithologies consisting of silty claystone with moderate bioturbation. Samples from Site 1174 ranged in depth from 538.2 to 941.8 mbsf with lithologies consisting of silty and siliceous claystone. They used the constant-flow technique in their measurements.

Adaita et al. (2004) reported that backpressure was maintained at 350 kPa, and tests were carried out at a serious of confining pressures of 375 to 800 kPa. Effective pressure ranged from 25 to 450 kPa. Two samples from Site 1173 came from depths of 117 to 166 mbsf. Samples include sedimentary Unit II (upper Shikoku Basin facies), which is characterized by hemipelagic mud with abundant ash. Two samples from Site 1174 came from depths of 394 to 452 mbsf. Samples include Unit IIB and IIC (outer trench-wedge and trench-to-basin transition facies), which are characterized by silt turbidites and hemipelagic mud. The permeability values of four samples tested range

from 10^{-15} to 10^{-18} m^2. The samples showing lower permeability consist entirely of hemipelagic mud.

Gamage and Screaton (2003) measured permeabilities at varying effective stress values ranging from 240 to 620 kPa. The highest coefficient of permeability is 6.45E-17 m^2 for a sample from the upper Shikoku Basin facies. The lowest coefficient of permeability is 3.7E-19 m^2 for a sample from lower Shikoku Basin facies. The permeability values decrease with increases in effective stress, and deeper samples show less variation in permeability with increase in effective stress.

Bourlange et al. (2004) reported permeability measurements for samples from ODP Sites 1173 and 1174. Samples came from lower Shikoku basin facies. Tests were performed in the 0.5–2.5 MPa range in a tri-axial cell. Their results indicate that permeability decreases from 10^{-18} to 10^{-19} m^2 with effective confining pressure increasing from 0.2 to 1.5 MPa. When the effective pressure is then increased from 1.5 to 2.5 MPa, permeability is roughly constant at 10^{-19} m^2.

Rowe et al. (2011) completed permeability measurements for sample from IODP Site C0001 and Sites C0004, C0006, C0007, and C0008. Sites C0001, C0004, and C0008 represent sediments from the megasplay fault region from the Kumano Basin transect off Kii Peninsula, whereas samples from Sites C0006 and C0007 represent sediments from the frontal thrust region. The constant-flow method was used to measure the permeability of samples. Tests were performed in the 0.14–0.41 MPa range in a tri-axial cell. The permeability values range from 5.26E-16 to 2.51E-19 m^2 (Table 9). Lower permeabilities tend to represent clay-rich sediments, whereas the higher permeabilities represent sand-rich or interbedded ash layers.

Yue et al (2011) also completed permeability measurements for samples from IODP Site C0001 that represents sediments from megasplay fault zone from Kumano Basin. The samples came from depths of approximately 25 to 290 m below seafloor and include lithologic Units I (slope apron facies) and II (upper accretionary prism). The constant-flow method was used to measure the permeability of samples. Effective isotropic confining stress during the tests ranged from 0.034 MPa (5 psi) to 0.551 MPa (80 psi). Average values of intrinsic permeability range from 10^{-16} to 10^{-17} m^2. The ratio of horizontal to vertical permeability averages 1.15.

Gamage et al. (2011) documented permeability-porosity relationship of sediments from different subduction zones, such as northern Barbados, Costa Rica, Nankai, and Peru (Table 10). For siliciclastic sediments and diatom oozes, permeability decreases with increase in percentage of clay-size material. But nannofossil oozes have permeability values 1.5 orders of magnitude higher than siliciclastic sediments of the same porosity and show poor correlation between permeability and porosity.

Yang et al. (2007) documented permeability for 30 deeply buried mudstones from North Sea, Gulf of Mexico, and Caspian Sea wells. The samples have the following ranges of key properties: clay-sized fraction content 12-66%; maximum effective stress 15-38 MPa, burial depth 1800-5200 m; porosity 5.5-26.5%. Transient pulse decay method was used to measure the permeabilities with effective stress ranging between 2.5 and 60 MPa. They reported vertical permeability decreases logarithmically with porosity.

Table 9. Permeability test results for samples from IODP Sites C0004, C0006, C0007, and C0008 (Rowe et al., 2011)

Core, section interval (cm)	Depth mbsf	Effective Stress (MPa)	Intrinsic Permeability (m^2)
316-C0004D-			
29R-CC, 19.5	277.14	0.14	9.32E-17
		0.27	3.91E-17
		0.41	2.45E-17
48R-1, 28	359.87	0.14	2.41E-17
		0.34	1.56E-17
		0.55	1.40E-17
52R-3, 78	381.07	0.14	1.76E-17
		0.28	1.17E-17
		0.41	8.68E-18
55R-1, 28.5	391.36	0.14	1.75E-17
		0.28	1.45E-17
316-C0006E-			
19X-4, 97	119.62	0.14	2.55E-17
		0.27	1.42E-17
		0.41	1.33E-17
34X-3, 84	262.09	0.14	3.85E-17
45X-3, 65	366.27	0.14	2.35E-17
		0.27	7.26E-18
		0.41	4.36E-18
316-C0006F-			
17R-1, 65	542.91	19.62	2.51E-19
316-C0007C-			
6X-4, 57	55.95	0.14	9.30E-17
		0.27	5.92E-17
		0.41	5.28E-17

(Table 9 cont'd)

Core, section interval (cm)	Depth mbsf	Effective Stress (MPa)	Intrinsic Permeability (m^2)
11X-1, 24	100.32	0.14	1.31E-17
		0.27	8.51E-18
		0.41	6.93E-18
316-C0007D-			
17R-2, 24	324.60	19.62	3.02E-18
23R-4, 4	383.89	0.14	1.79E-17
		0.27	5.67E-18
		0.41	4.30E-18
29R-2, 77	438.62	0.14	1.99E-18
316-C0008A			
6H-6, 90	50.50	0.14	2.62E-16
		0.27	1.79E-16
		0.41	1.31E-16
12H-6, 88.5	106.00	0.14	7.24E-17
		0.27	5.09E-17
		0.41	3.88E-17
20H-4, 96	156.33	0.14	1.40E-16
		0.27	7.92E-17
		0.41	5.98E-17
24H-4, 84.5	191.14	0.14	5.86E-17
		0.27	3.79E-17
		0.41	3.09E-17
316-C0008C-			
5H-2, 19.5	34.79	0.14	1.50E-16
		0.27	9.16E-17
		0.41	7.06E-17
25X-11, 96	173.96	0.14	4.49E-16
		0.27	3.17E-16
		0.41	7.40E-17

Table 10. Log linear permeability-porosity relation predicted for varying lithology at Barbados, Costa Rica, Nankai, and Peru subduction zones (Gamage et al., 2011). k = permeability, n = porosity, R^2 = coefficient of determination.

Lithologies and location	Permeability–porosity relationship
Siliciclastics	
Barbados claystones	log $(k) = -25.3 + 13.2n$ ($R^2 = 0.60$)
Costa Rica silty claystones	log $(k) = -20.6 + 6.1n$ ($R^2 = 0.63$)
Nankai silty claystones	log $(k) = -19.8 + 5.2n$ ($R^2 = 0.72$)
Silty claystones (Costa Rica and Nankai)	log $(k) = -19.9 + 5.1n$ ($R^2 = 0.69$)
All siliciclastics	log $(k) = -19.8 + 4.6n$ ($R^2 = 0.55$)
Diatom oozes	
Costa Rica diatom oozes	log $(k) = -20.4 + 4.9n$ ($R^2 = 0.82$)
Peru diatom oozes	log $(k) = -17.3 + 1.0n$ ($R^2 = 0.19$)
All diatom oozes	log $(k) = -19.9 + 4.9n$ ($R^2 = 0.49$)
Nannofossil oozes and chalk	
Peru nannofossil oozes	log $(k) = -15.2 + 0.4n$ ($R^2 = 0.02$)
All nannofossil oozes (Peru and Costa Rica)	log $(k) = -14.5 - 1.3n$ ($R^2 = 0.07$)
Peru nannofossil chalk	log $(k) = -28.9 + 20.7n$ ($R^2 = 0.77$)
Costa Rica nannofossil chalk	log $(k) = -18.0 + 4.5n$ ($R^2 = 0.36$)
All chalks	log $(k) = -20.5 + 7.7n$ ($R^2 = 0.21$)

Table 11. Permeability values that were calculated from CRS consolidation tests for Sites C0004, C0006, C0007, and C0008 (Saffer et al., 2011; Guo et al., 2011)

Test	Hole, core, section	Depth (mbsf)	Permeability (k) (m^2)
U-136	C0004D-47R-2	357.11	1.37E–17
U-140	C0004D-51R-2	375.08	6.50E–18
MU-7	C0004D-52R-3	380.81	1.05E–17
U-127	C0008C-9H-5	71.64	5.58E–17
MU-8	C0008A-17H-8	137.23	3.10E–17
MU-10	C0008C-23X-6	152.73	5.22E–17
MU-11	C0008C-23X-6	152.84	2.79E–17
MU-9	C0008A-27H-2	211.95	2.89E–17
MU-19	C0006E-5H-1, 128	35.56	6.20E–16
MU-20	C0006E-16X-1, 113	89.96	3.15E–16
MU-21	C0006E-22X-6, 5	150.04	1.71E–17
MU-22	C0006E-26X-1, 126	183.5	1.44E–17
MU-23	C0006E-34X-3, 59	261.64	4.47E–18
MU-24	C0007C-3H-3, 104	32.64	6.97E–17
MU-25	C0007D-25R-2, 66	400.59	7.02E–18

Dewhurst et al. (1999) documented that mudstone permeability varies by ten orders of magnitude and by three orders of magnitude at a single porosity. Much of the range at a given porosity can be explained by differences in grain size; at a given effective stress, coarser-grained mudstones are more permeable than fine-grained mudstones. They stressed that none of the existing permeability models are ideal and they need to be validated through the acquisition of a larger permeability database of well characterized mudstones.

Constant-rate-of-strain (CRS) consolidation tests were performed by Saffer et al. (2011) on eight whole-round samples from IODP Sites C0004 and C0008 (from depth of ~71 to ~380 mbsf) and by Guo et al. (2011) on seven whole-round samples from Sites C0006 and C0007 (from depth of ~32 to ~400 mbsf) to estimate in-situ effective stress and pore pressure conditions, and to define the compression behavior and hydraulic properties of the sediments. Saffer et al. (2011) reported that in-situ effective stress values of samples from Sites C0004 and C0008 range between 0.52 and 9 MPa. Results show that all samples are overconsolidated. In-situ effective stress increases systematically as burial depth increases in Site C0004, but the in-situ stress values vary with burial depth in Site C0008. Guo et al. (2011) reported the in-situ effective stress values of samples from Sites C0006 and C0007 range between 0.53 and 10.4 MPa. Results show that all samples are overconsolidated, highly disturbed. Permeability results were calculated from CRS consolidation tests and tabulated in Table 11.

Previous laboratory tests of natural clay–rich sediment and shale reveal large ranges in values of intrinsic permeability and hydraulic conductivity because of differences in the material's mineral composition, texture, and porosity (Bennett et al.,

1989; Neuzil, 1994; Dewhurst et al., 1999; Yang and Aplin, 2007; Gamage et al., 2011). Overall, permeability results of this study are consistent and similar with previous those studies; Taylor et al. (1993), Gamage et al. (2003), Adaita et al. (2004), Dungan and Daigle (2011), Reuschle (2011), Saffer et al. (2011), Guo et al. (2011), and Rowe et al. (2011).

Linear regression and determination of r-value of horizontal (r = 0.01; 14 data points) and vertical (r = 0.02; 20 data points) sections demonstrates that porosity does not show a statistically significant correlation with permeability at confidence level of %95 (Fig. 32). Appendix chapter contains details about statistical analysis, and definition of two-tail test. The data set for porosity-permeability relation was plotted with upper and lower limits of Gamage et al. (2011), calculated to match the standard deviation of the Nankai silt claystone log-linear equation (Fig. 33). The porosity-permeability relation shows a modest conformity with Gamage et al. (2011)'s larger data set. It is important to note that the used data set by the Gamage et al (2011) was collected from different sites and facies. The local variations (e.g., lithology) may be the responsible for the disagreement.

One porosity value is significantly higher than the shipboard and pre-test measurements (sample 316-C0006E-7H-2, 117 cm). The possible reasons of this difference are: (1) damage during transportation and/or storage, (2) expansion of micro-fractures after the pressure release. Thus, the sample 316-7H-2, 117 cm was omitted from porosity interpretations.

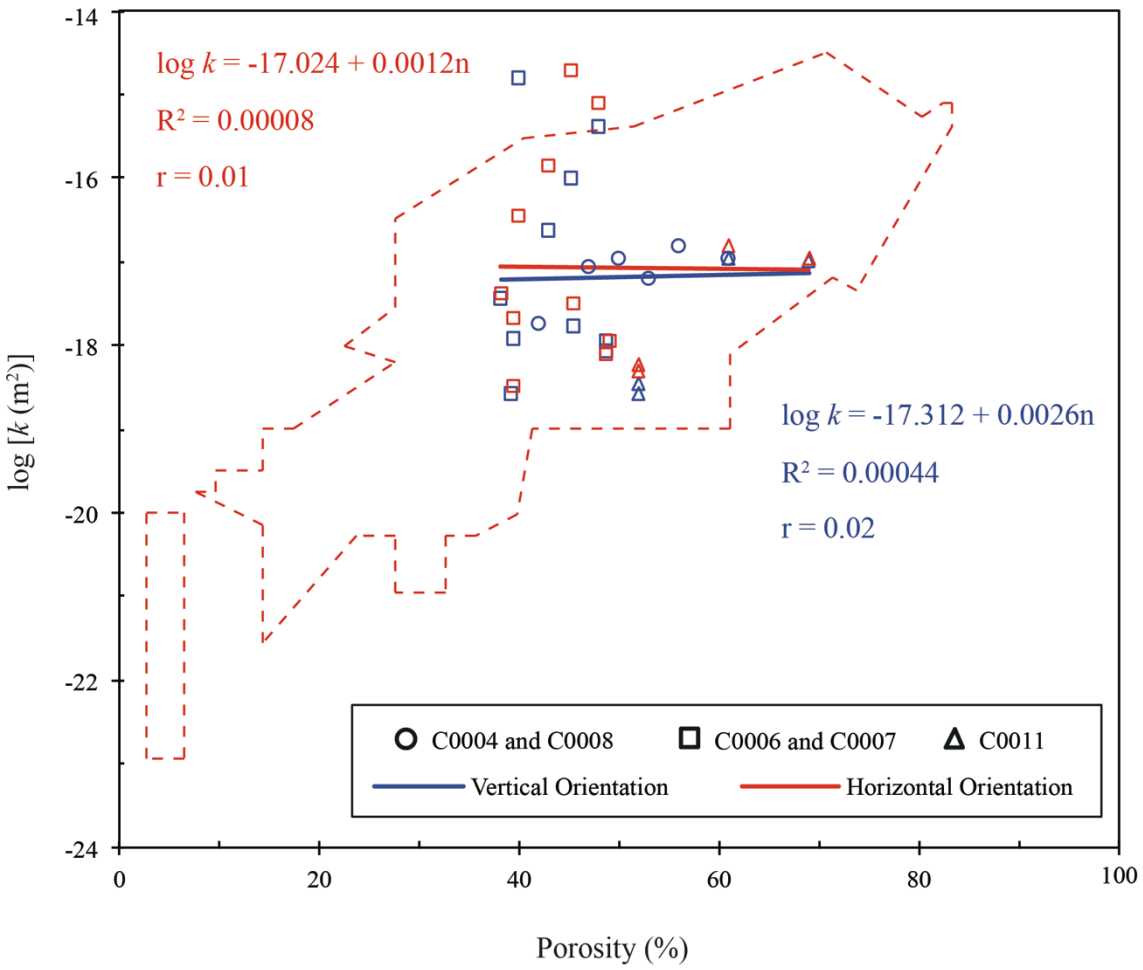

Figure 32. Linear regression between permeability and porosity values for Sites C0004, C0006, C0007, and C0008. It is superimposed on outline of Neuzil (1994) plot for argillaceous sediments. r = correlation coefficient, n = porosity.

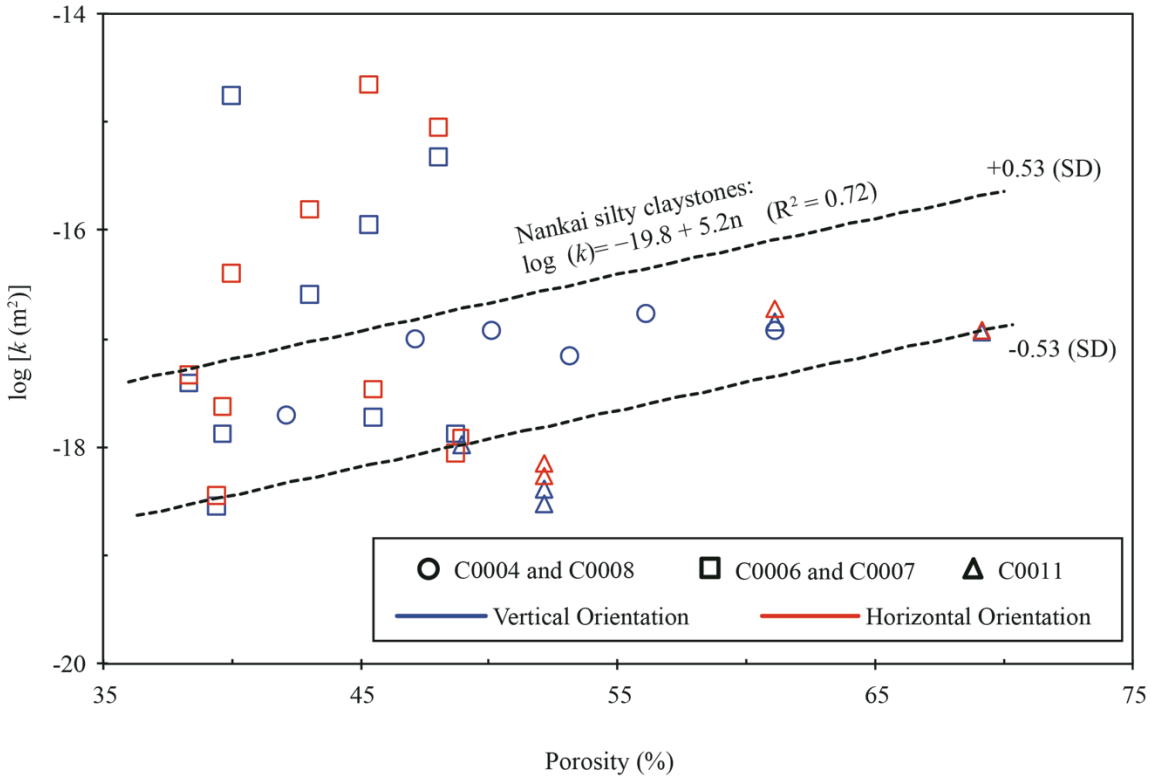

Figure 33. Plots of porosity values superimposed Gamage et al. (2011)'s permeability-porosity relation for the Nankai silt claystones. SD = standard deviation. Dash lines represent upper and lower ultimate limits for log-linear relation.

The tests for statistical significance at a specific confidence level show that a relation exists between relative total clay-mineral abundance and permeability (r = 0.71; 21 data points) (Fig. 34). Likewise, there is a negative linear correlation between relative smectite abundance in bulk sediment and permeability (r = 0.56; 21 data points) (Fig. 35). However, the permeability does not show a statistically significant correlation with relative abundance of illite in bulk mud (r = 0.07; 21 data points) (Fig. 36) at confidence level of 0.05 (%95). Mitchell (1993) pointed out that smectite clay minerals have a layer lattice structure, expandable, interlayer cations exchangeable and interlayer surfaces and cations hydratable. In contrast, illite clay minerals are non-expanding, and their interlayers are mainly occupied by poorly hydrated potassium cations responsible for absence of swelling. Thus, chemical and structural differences between smectite and illite may be the possible reasons why smectite mineral abundance correlates with permeability but illite mineral abundance does not.

The microfabric on the vertical cut face shows better-preferred orientation than microfabric on the horizontal, which increases the anisotropy of permeability ($k_h/k_v > 1$). Nonetheless, the microfabric anisotropy does not show a statistically significant correlation with; the vertical permeability (r = 0.30, 20 data points) (Fig. 36), the horizontal permeability (r = 0.0.38, 14 data points) (Fig. 37), or the anisotropy of permeability ($r = 0.40$, $n = 14$ data points) (Fig. 38). The standard deviations of orientation and the indexes of microfabric orientation are consistent with highly random arrangements of particles. No clearly defined trend is present between the fabric and depth of burial. Samples with significant increases in the anisotropy of permeability ($k_h/k_v > 1$) also show significant improvements of preferred orientation on the vertical cut face.

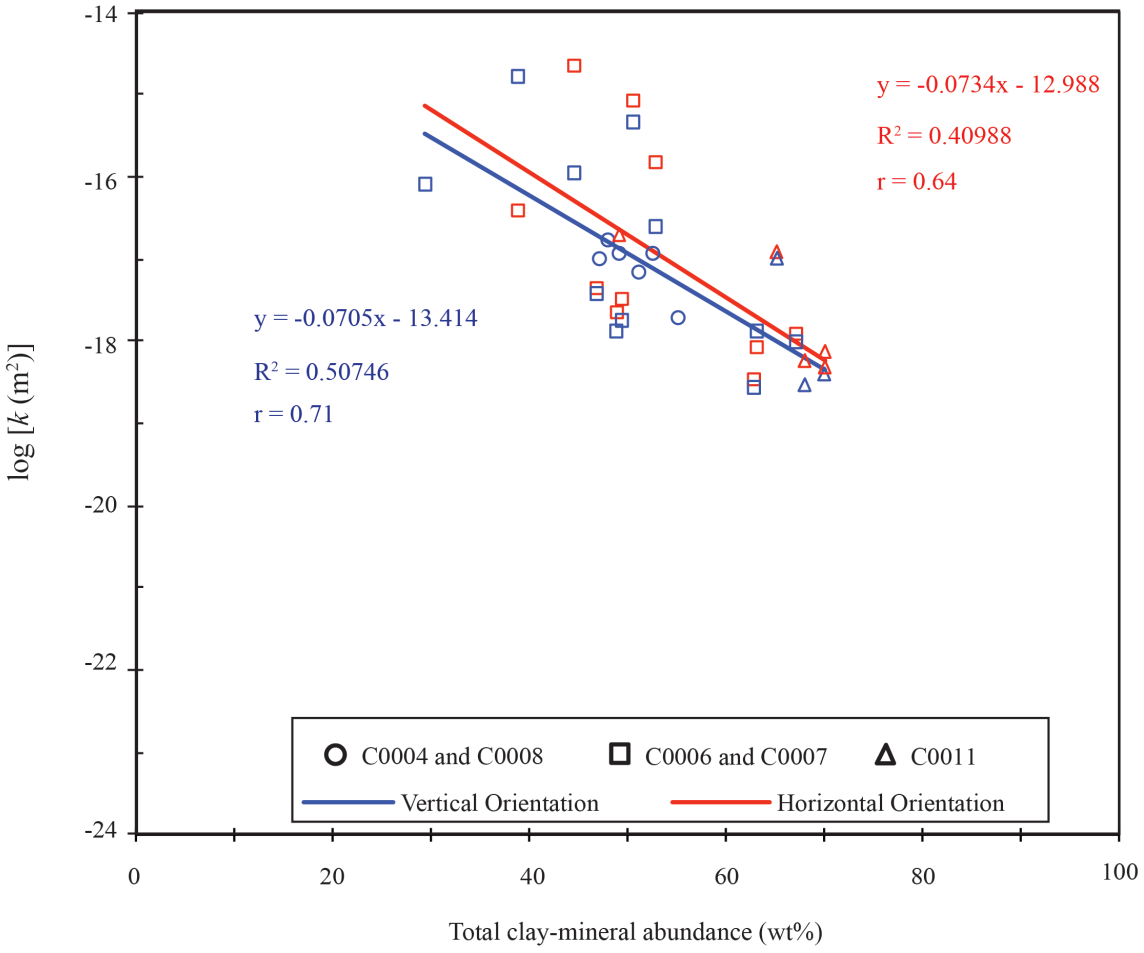

Figure 34. Linear regression between permeability and relative abundance of total clay minerals. r = correlation coefficient.

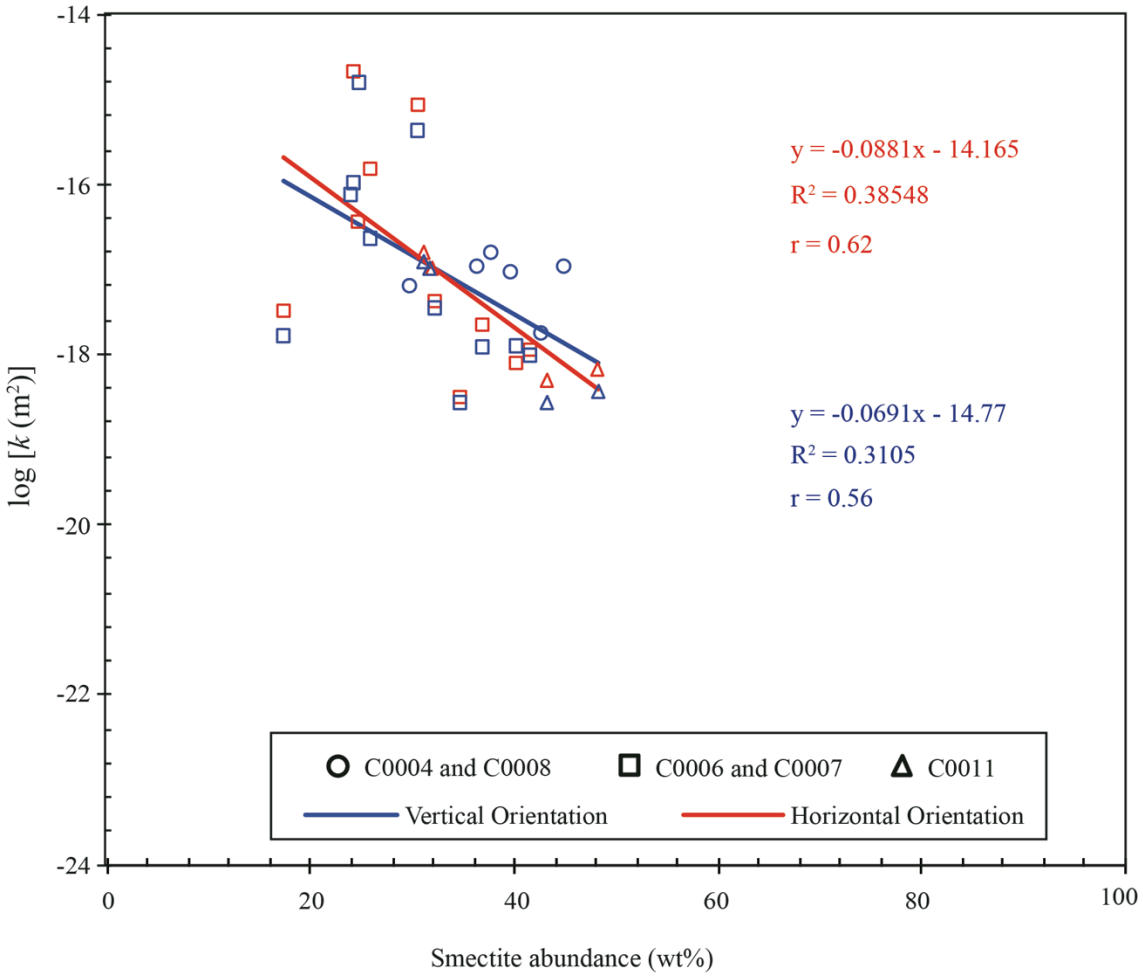

Figure 35. Linear regression between permeability and relative mineral abundance of smectite in bulk mud. r = correlation coefficient.

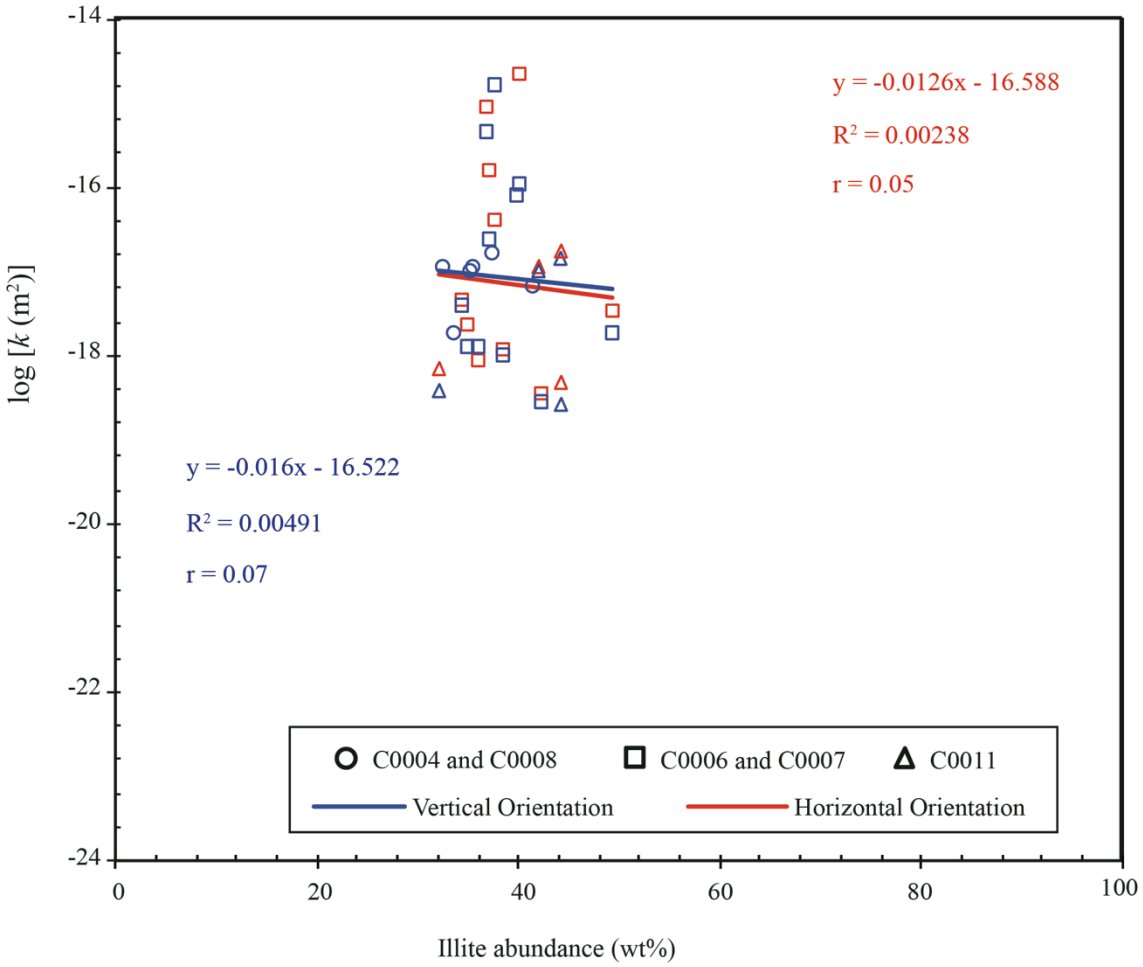

Figure 36. Linear regression between permeability and relative mineral abundance of illite in bulk mud. r = correlation coefficient.

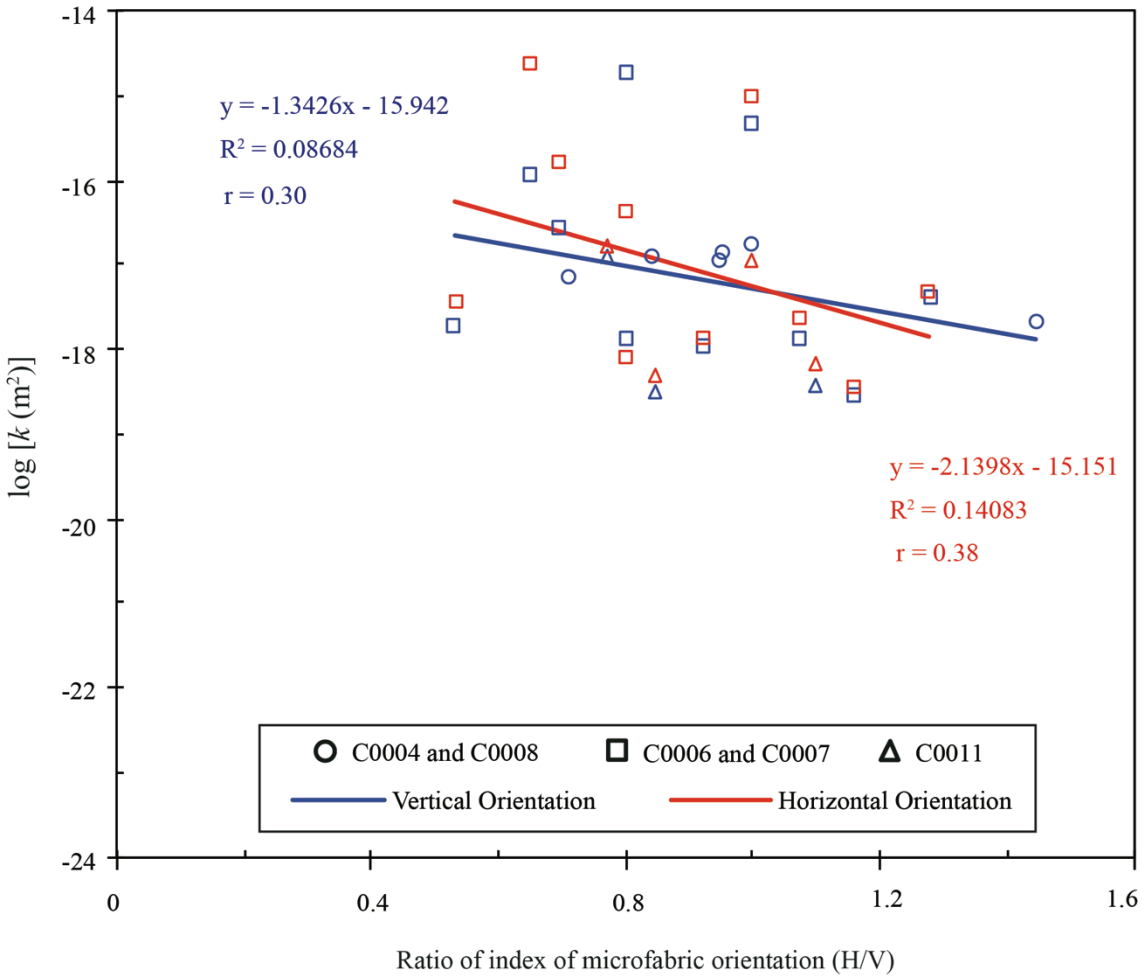

Figure 37. Linear regression between permeability and ratio of index of microfabric orientation for all samples. r = correlation coefficient.

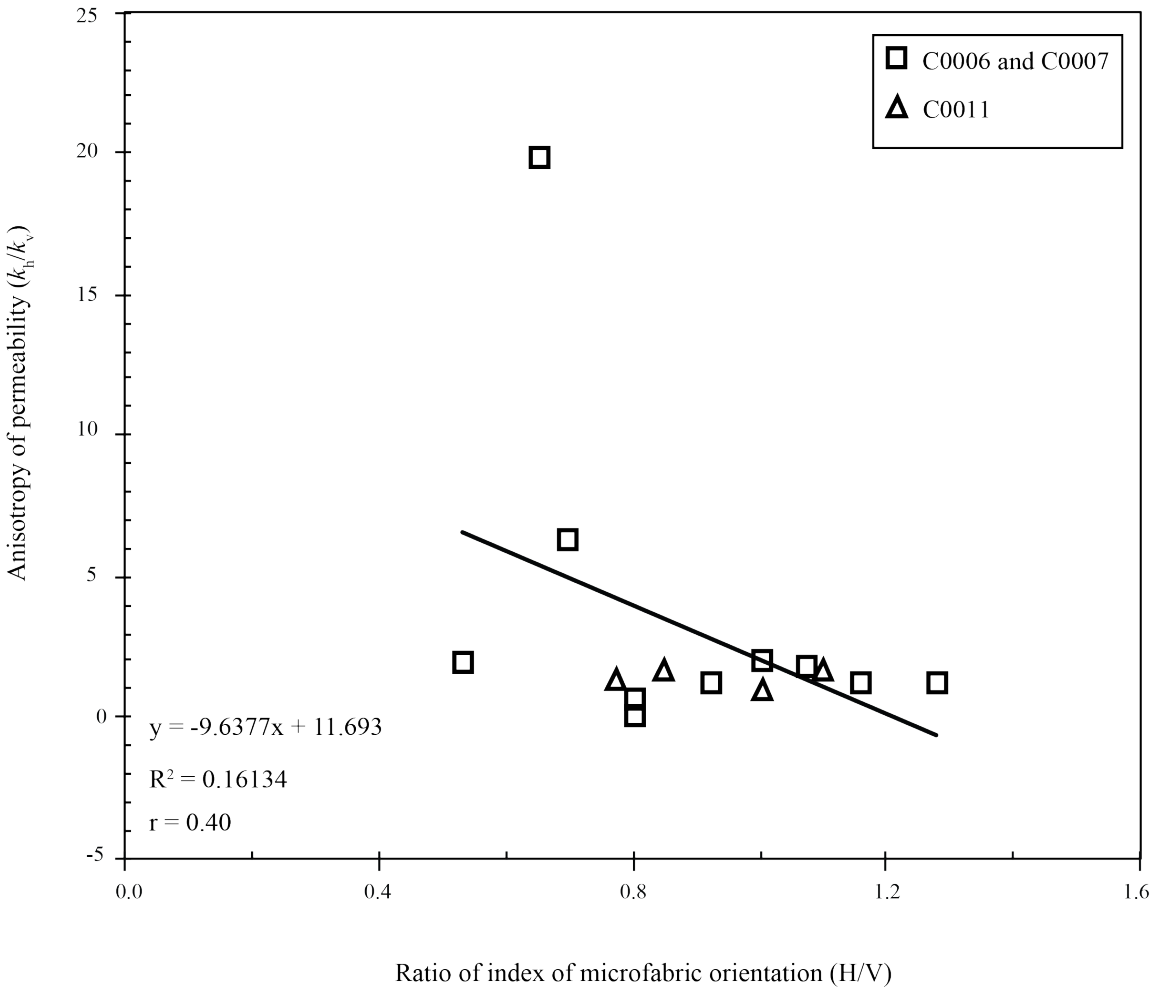

Figure 38. Linear regression between anisotropy of permeability and ratio of index of microfabric for samples from Sites C0006, C0007, and C0011. r = correlation coefficient.

This sensitivity of permeability to changes in grain fabric is to be expected as a weak fissility begins to develop with progressive compaction of the mudstone.

Interpretation of these results, however, needs to take the dip of bedding into account. When beds of mudstone display a strong bedding-parallel fabric, with dips close to 45°, the fabric should be the same on horizontal and vertical sections (Guo et al., 2011; Saffer et al., 2011). For samples from the frontal thrust zone, beds dip at angles >30º, when bedding dip angles of samples from the megasplay fault and sediment inputs zones vary between 0º and 25º. The results of this study show that ratios of index of microfabric orientation range between 0.53 and 1.44. Thus, there is no clear trend between bedding dips and microfabric orientation, although the number of samples tested is not large enough to demonstrate a definitive statistical correlation.

Grain size is another variable that usually affects hydraulic conductivity (Moon and Hurst, 1984; Bennett et al., 1989; Mitchell, 1993). Kopf et al. (2011) documented the particle size distribution of sediments recovered from IODP Sites C0001 through C0008. Statistical analysis shows that a statistical significant correlation does not exist between permeability and median grain size. One possible reason for this is that grain size doesn't change enough within the mudstone to import much effect (Fig. 39). Figure 40 shows correlation between the content of clay-size particles and permeability. This correlation also fails the test for statistical significance. Evidently, the mineral content is more important than clay-size content as an influence on hydraulic properties, at least over the range of depths sampled in this study.

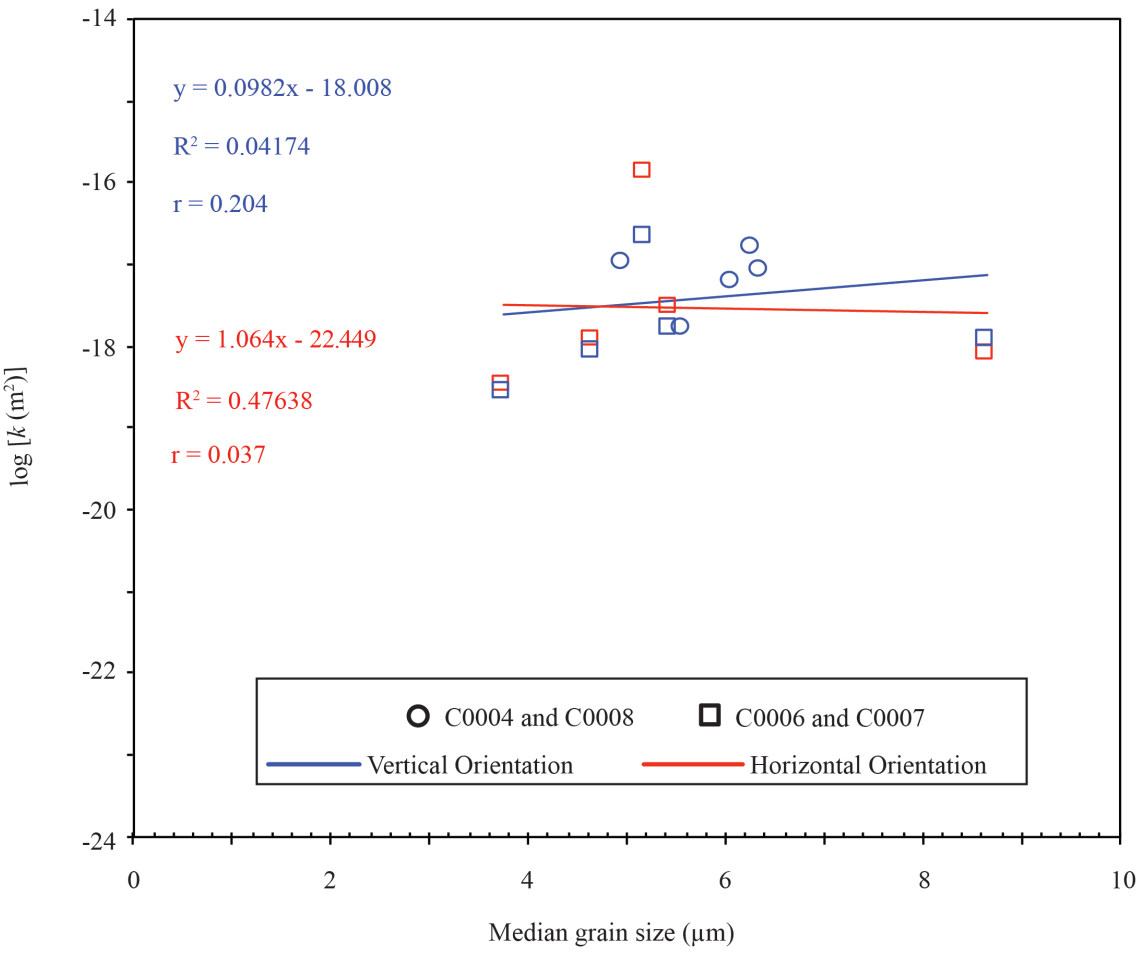

Figure 39. Linear regression between permeability and average median grain size of sediments from Sites C0006, C0007, and C0011. r = correlation coefficient.

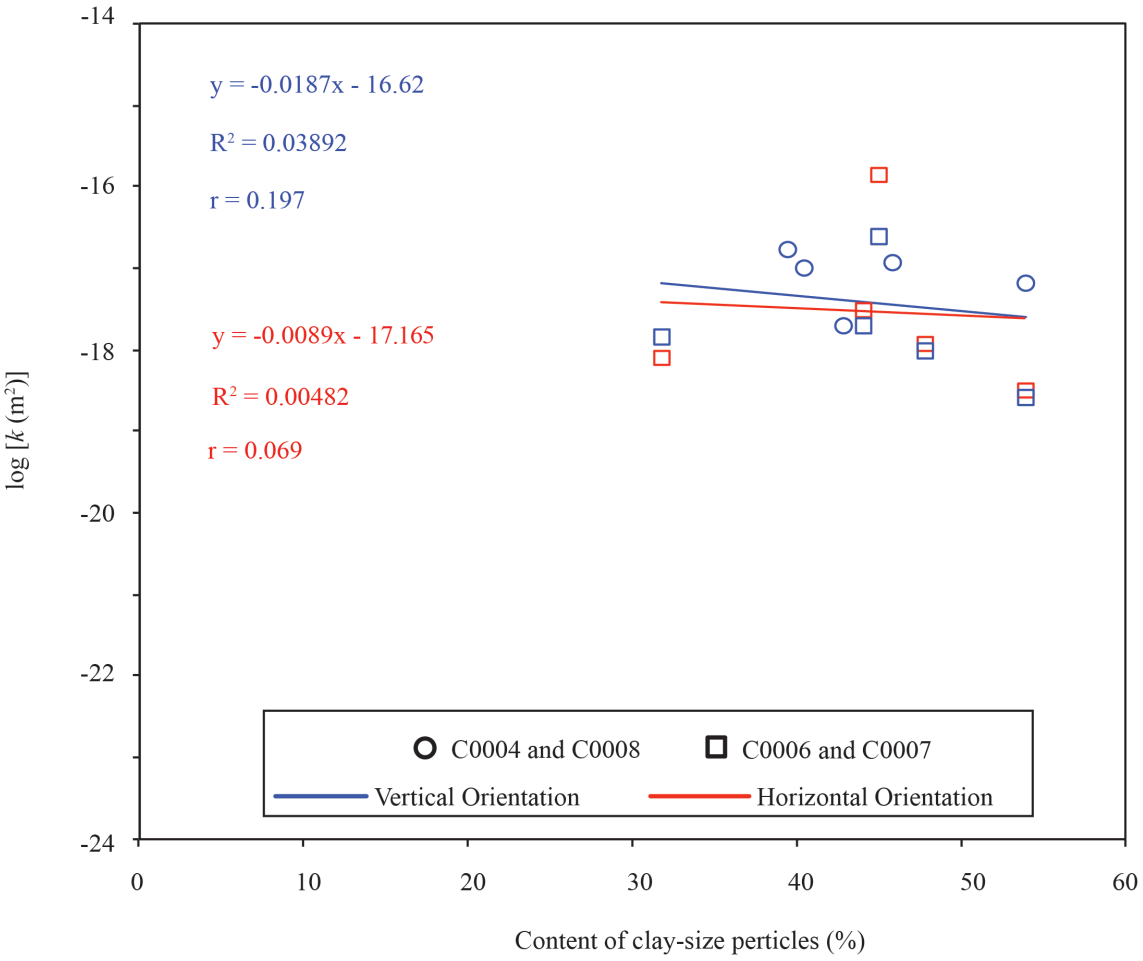

Figure 40. Linear regression between permeability and clay-size fraction (< 4-µm) for samples from Sites C0006, C0007, and C0011. r = correlation coefficient.

6. CONCLUSIONS

Constant-flow permeability tests were completed to measure permeability for vertical and horizontal direction using twenty-one samples collected from the Nankai Trough accretionary prism and Shikoku Basin during the IODP Expeditions 316 and 333. Effective isotropic confining stress was set at 0.55 MPa (80 psi). The results of constant-flow through tests on mud/mudstone lithologies were correlated with the microfabric and clay mineralogy.

For samples from the megasplay fault zone, the vertical permeability ranges between 1.61E-17 m^2 and 1.86E-18 m^2 above the depth of 381 mbsf. The vertical permeability varies from 1.63E-15 to 2.68E-19 m^2 at the frontal thrust zone between depths of 35 and 564 mbsf, whereas the values of horizontal permeability range between 2.11E-15 and 3.32E-19 m^2. Samples from Shikoku Basin came from ~36 to 362 mbsf. Their values of vertical permeability differ between 1.34E-17 m^2 and 2.83E-19 m^2, whereas the values of horizontal permeability show variations between 1.80E-17 m^2 and 5.15E-19 m^2. The ratio of horizontal to vertical permeability (k_h/k_v) ranges between 0.02 and 19.90. The anisotropy ratio for permeability shows a modest decrease with depth in the frontal thrust zone, while it shows a modest increase with depth within the upper Shikoku Basin facies.

The porosity and permeability values tend to decrease as burial depth increases. The overall porosity-permeability relation for this study is similar to the larger data set documented in Gamage et al. (2011). The permeabilities for both directions do not show a statistically significant correlation with porosity. However, the small number of

samples tested needs to be considered; it is not large enough to demonstrate a definitive statistical trend.

The values of vertical permeability decrease with increases in the relative abundance of total clay minerals in bulk sediment. The relative abundance of smectite in bulk mud has a statistically significant correlation with the vertical permeability. Illite is the most abundant clay mineral in the Nankai accretionary prism, but relative percentages of illite do not impart a statistically significant influence on permeability. One possible reason for this is that smectite shows large variations with depth, while contents of illite do not.

Median grain size does not statistically correlate with permeability, probably because samples come from one similar lithology and have similar grain size distributions. The content of clay-size particles also fails to show statistically significant correlation with permeability. Thus, differences exist between the effects of changing the amount clay-size particles and abundance of specific clay minerals.

The standard deviation and the indexes of microfabric orientation are consistent with highly random arrangements of particle. The indexes of microfabric orientation and the steepness of cumulative curves are typically greater for the vertical section than for the horizontal section. Microfabric on the vertical cut face shows better preferred orientation than microfabric on the horizontal cut, which also influences the anisotropy of permeability ($k_h/k_v > 1$). However, microfabric anisotropy does not show a statistically significant correlation with either vertical or horizontal permeability, or with the anisotropy of permeability.

This study contributes to the test of one of the NanTroSEIZE's hypotheses, exploring the relationship between systematic, progressive material and state changes to the onset of seismogenic behavior along subduction thrusts. Saffer and Marone (2003) pointed out that transitions from aseismic to seismic slip and updip limit of seismicity are influenced by fault zone composition, consolidation state, normal stress magnitude, pore-fluid pressure, and strain rate. Similarly, Kinoshita et al. (2007) proposed that one of the highest priority goals in characterizing the Nankai Trough seismogenic zone, crucial for understanding subduction zone megathrust behavior, is to elucidate the role of the megasplay fault in accommodating plate motion through characterization of its mechanical and hydrologic behavior. Documenting the hydrological properties of sediments and sedimentary rocks within shallow levels of subduction zones such as Nankai Trough helps isolate the primary effect of lithology, porosity, microfabric, amount of fine-grained sediments, and type of clay minerals. Once those initial conditions are understood, the more complicated progression of depth- and stress-dependent evolution of fault properties can be evaluated.

APPENDIX

Two-tail Test

Two-tailed test was used to determine how statistically significant a correlation is between dependent and independent variables. Prior to collecting data, researchers predetermine an alpha level, which is how willing they are to be wrong when they state that there is a relationship (in the case of correlation research) or difference (in the case of a t-test) between the two variables they measured. A common alpha level for educational research is .05 for 95 percent confident level. For t-test, first, we must determine something called degrees of freedom (df). For a correlation study, the degrees of freedom are equal to 2 less than the number of subjects we had. If we collected data from 27 pairs, the degrees of freedom would be 25. The critical value table of Pearson's Correlation Coefficient (Table A2 Appendix) was used to find the intersection of alpha .05 (see the columns) and 25 degrees of freedom (see rows). The value found at the intersection (.381) is the minimum correlation coefficient r that we would need to confidently state 95 times out of a hundred that the relationship you found with our 27 subjects exists in the population from which they were drawn. If the absolute value of the correlation coefficient is above .381, null hypothesis (there is no relationship) is rejected and the alternative hypothesis is accepted: There is a statistically significant relationship between arm span and height, $r\ (25) = .87$, $p < .05$.

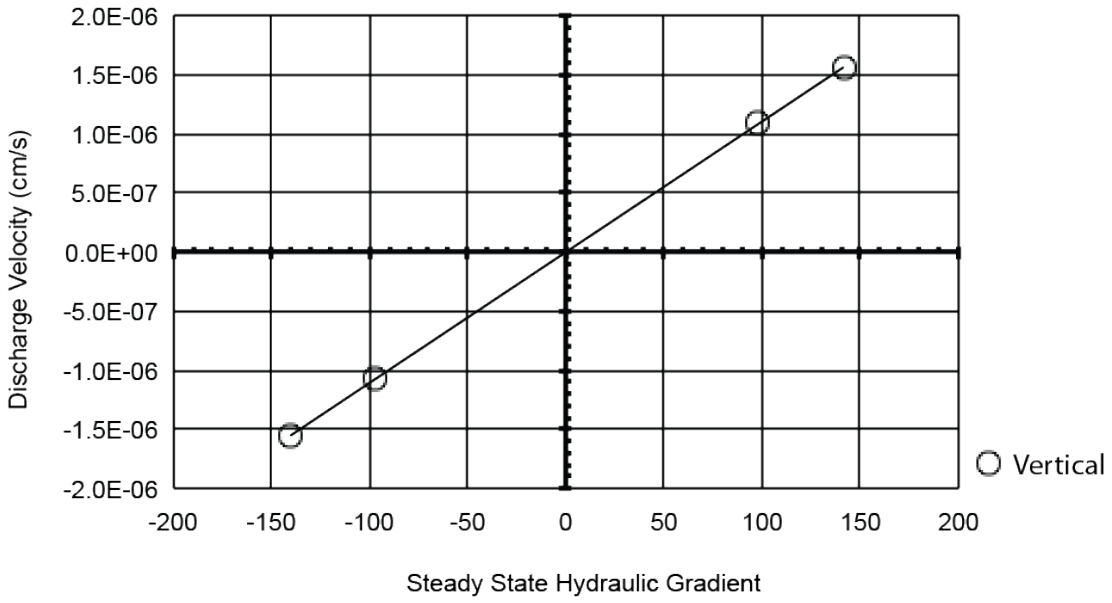

Figure A 1. Hydraulic gradient vs. discharge velocity (Sample 316-C0004C-6H-7, 16 cm).

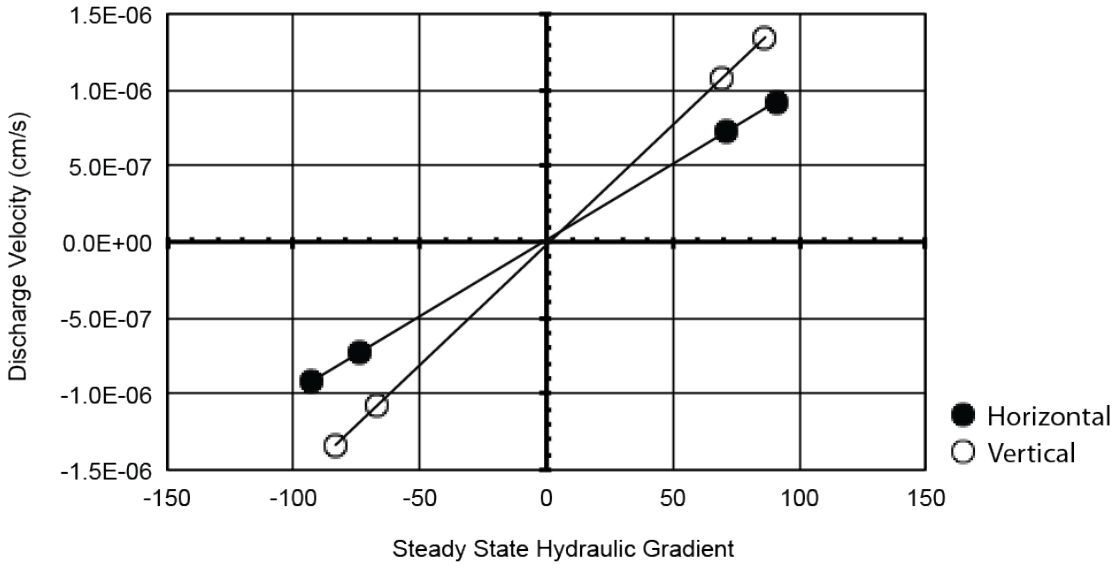

Figure A 2. Hydraulic gradient vs. discharge velocity (Sample 316-C0004C-8H-5, 92 cm)

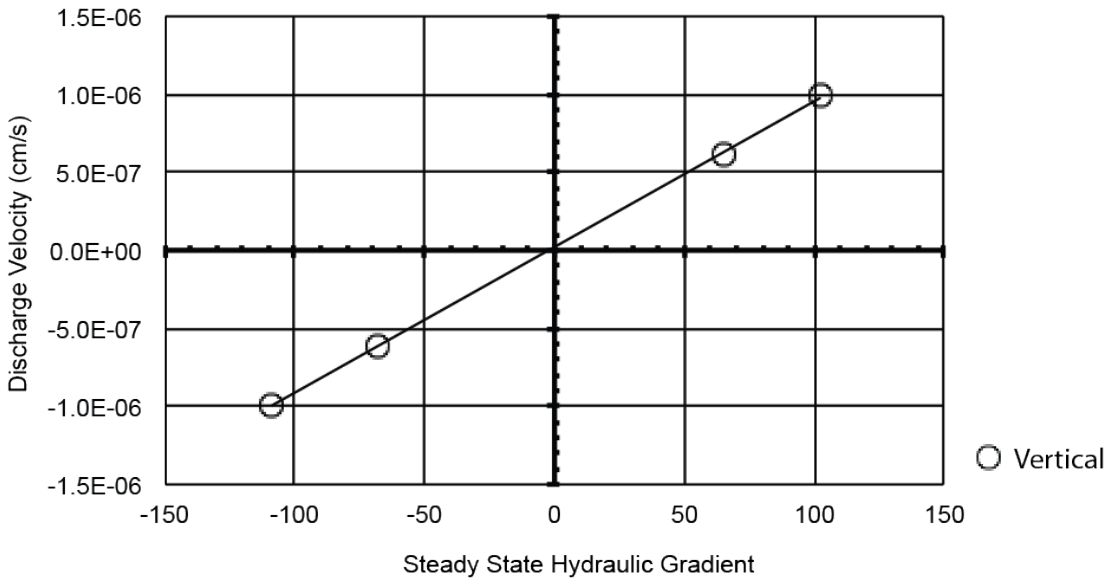

Figure A 3. Hydraulic gradient vs. discharge velocity (Sample 316-C0004D-44R-2, 72 cm).

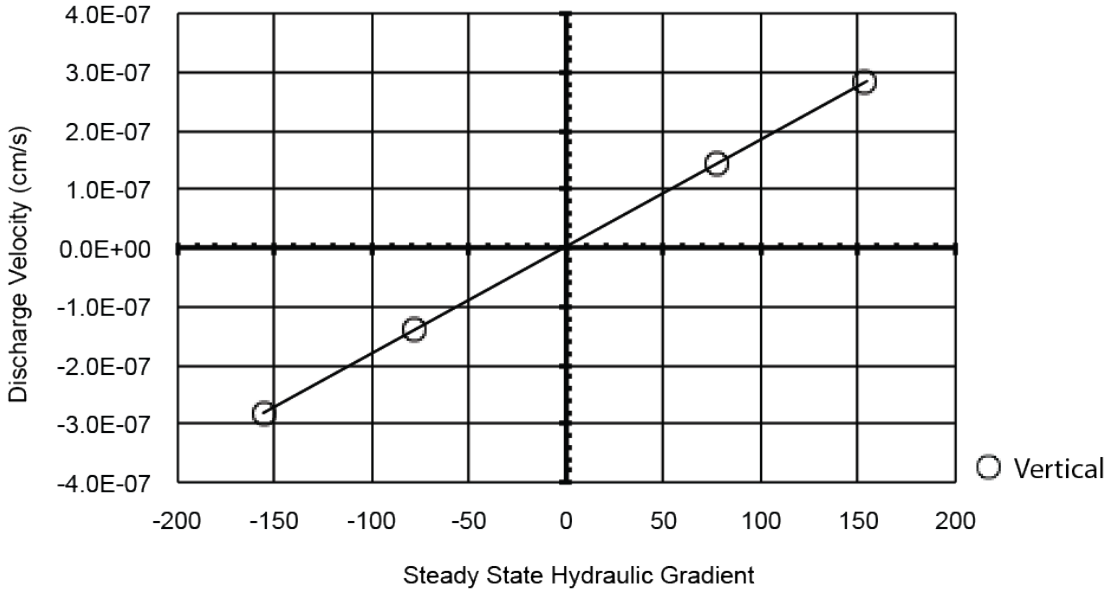

Figure A 4. Hydraulic gradient vs. discharge velocity (Sample 316-C0004D-52R-3, 112 cm).

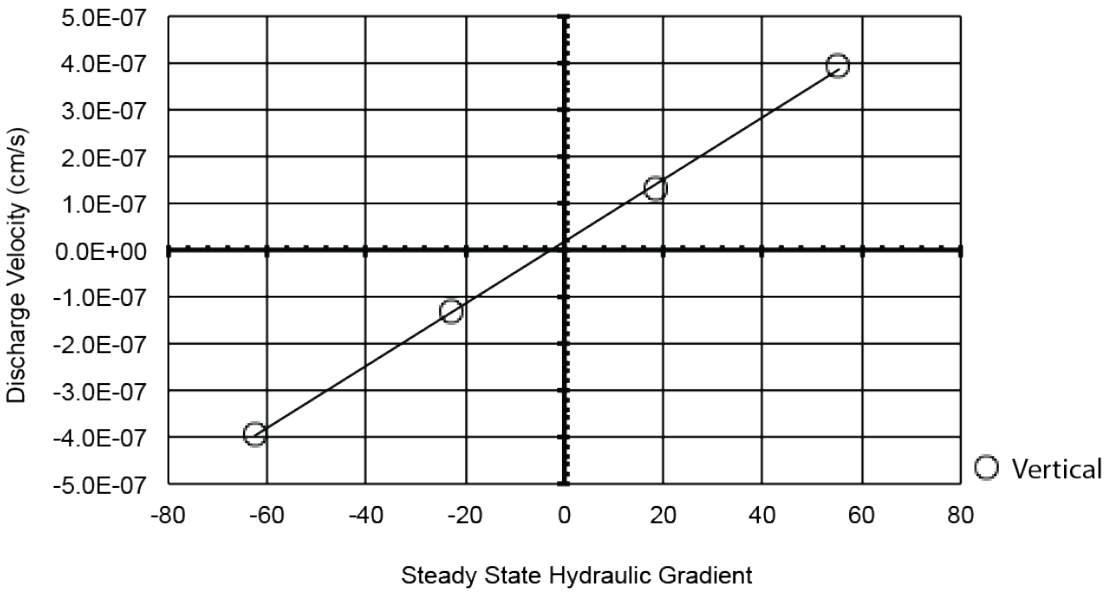

Figure A 5. Hydraulic gradient vs. discharge velocity (Sample 316-C0008A-17H-8, 25 cm).

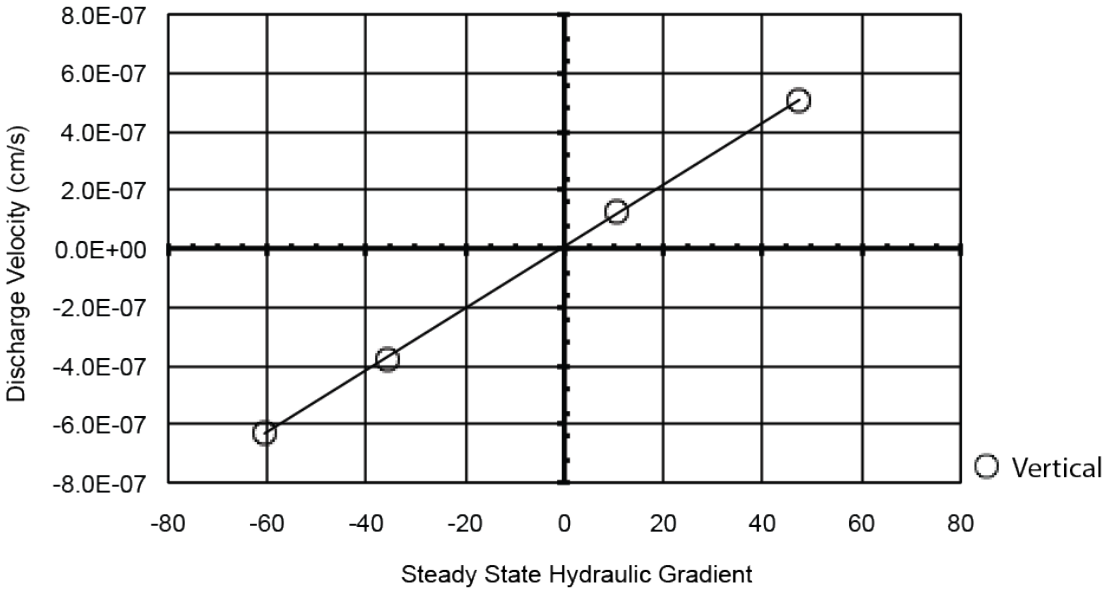

Figure A 6. Hydraulic gradient vs. discharge velocity (Sample 316-C0008A-27H-2, 25 cm).

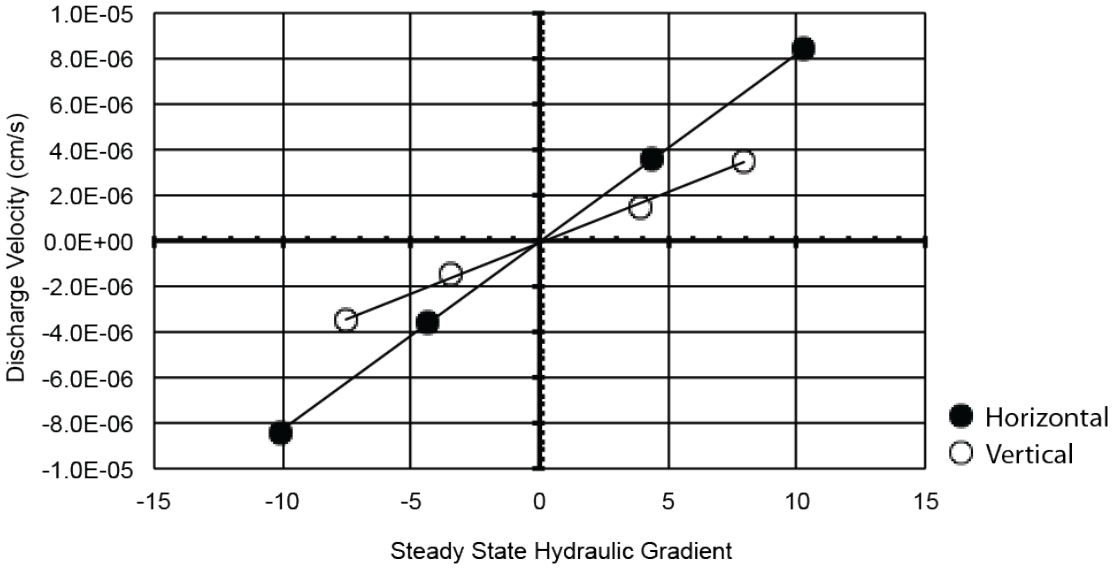

Figure A 7. Hydraulic gradient vs. discharge velocity (Sample 316-C0006E-5H-1, 128 cm).

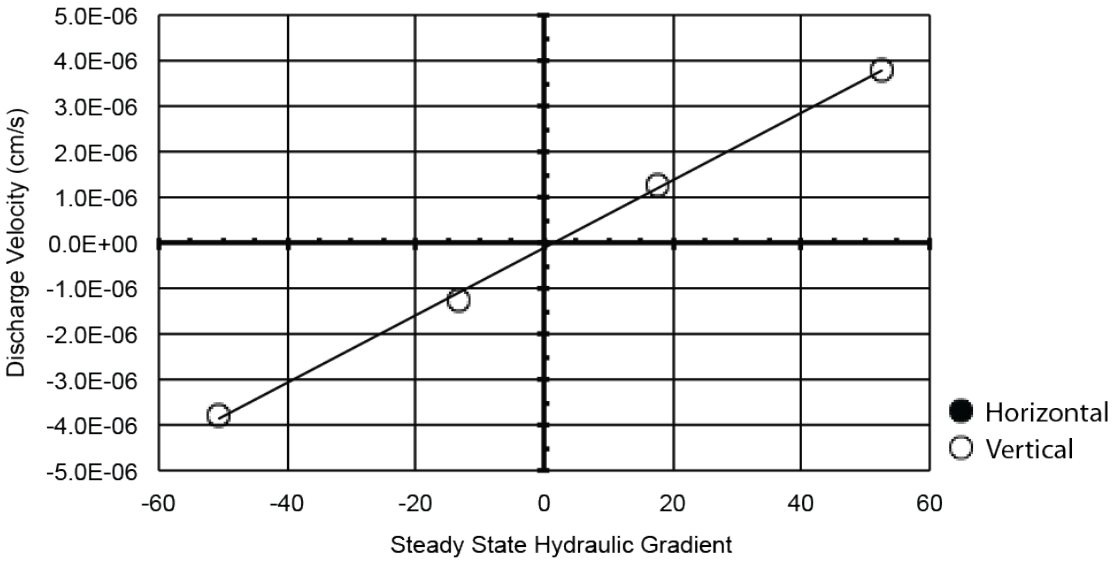

Figure A 8. Hydraulic gradient vs. discharge velocity (Sample 316-C0006E-7H-2, 117 cm).

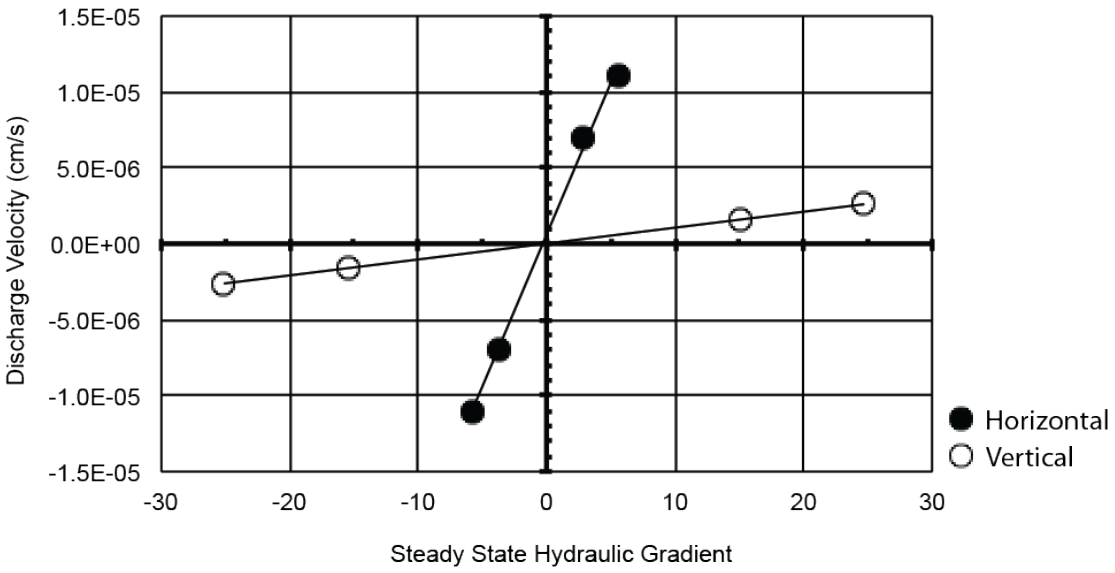

Figure A 9. Hydraulic gradient vs. discharge velocity (Sample 316-C0006E-16X-1, 113 cm).

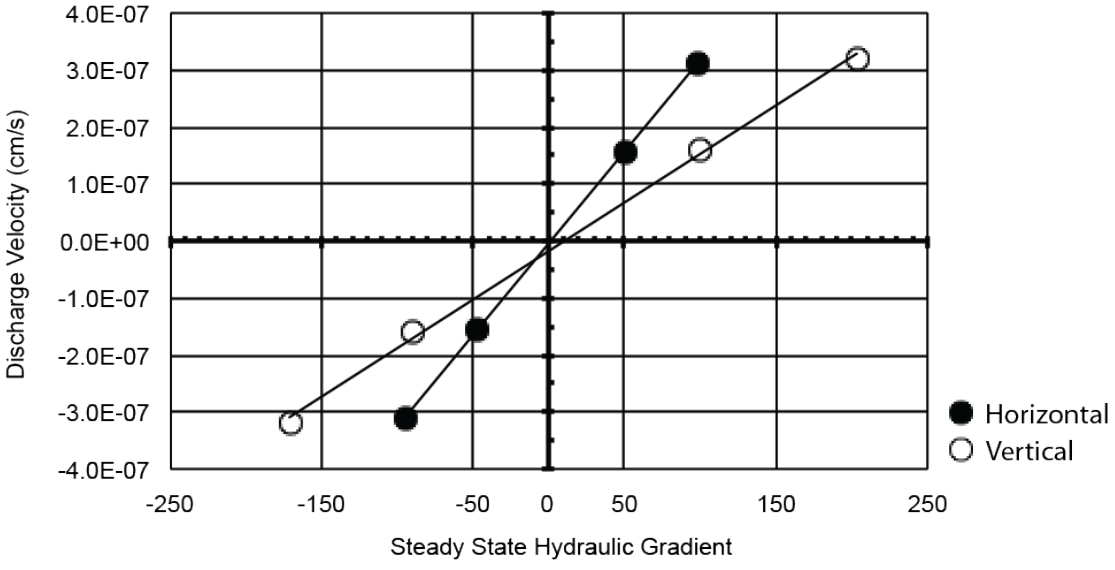

Figure A 10. Hydraulic gradient vs. discharge velocity (Sample 316-C0006E-20X-3, 1 cm).

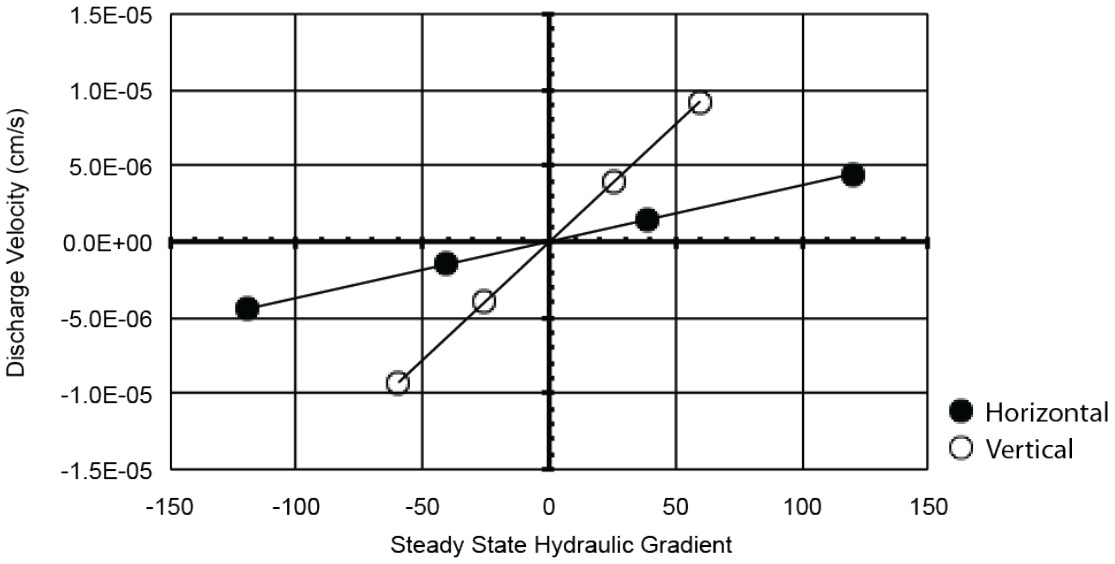

Figure A 11. Hydraulic gradient vs. discharge velocity (Sample 316-C0006E-22X-6, 5 cm).

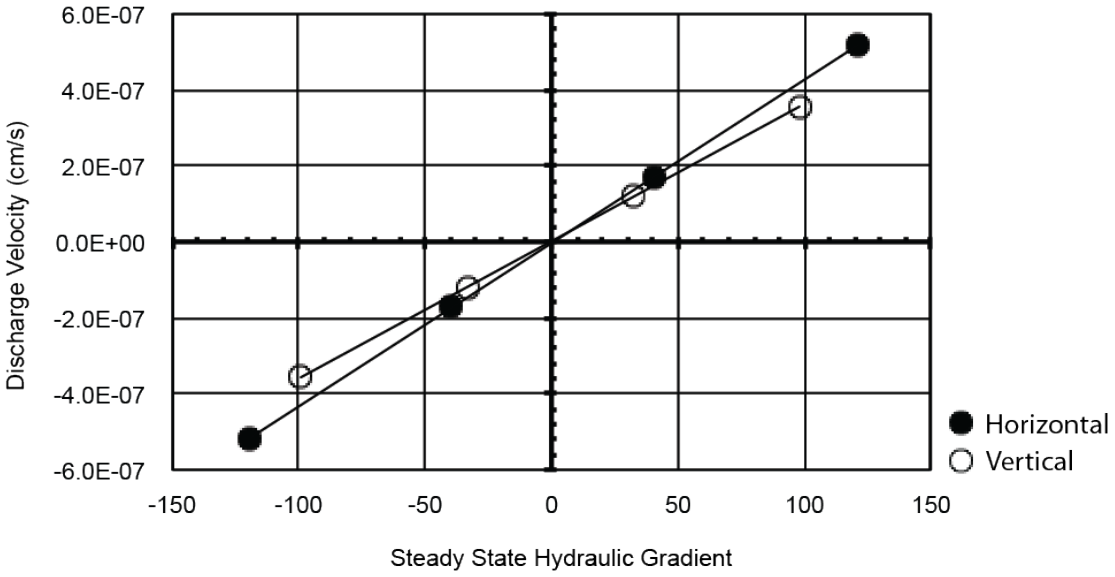

Figure A 12. Hydraulic gradient vs. discharge velocity (Sample 316-C0006E-26X-1, 126 cm).

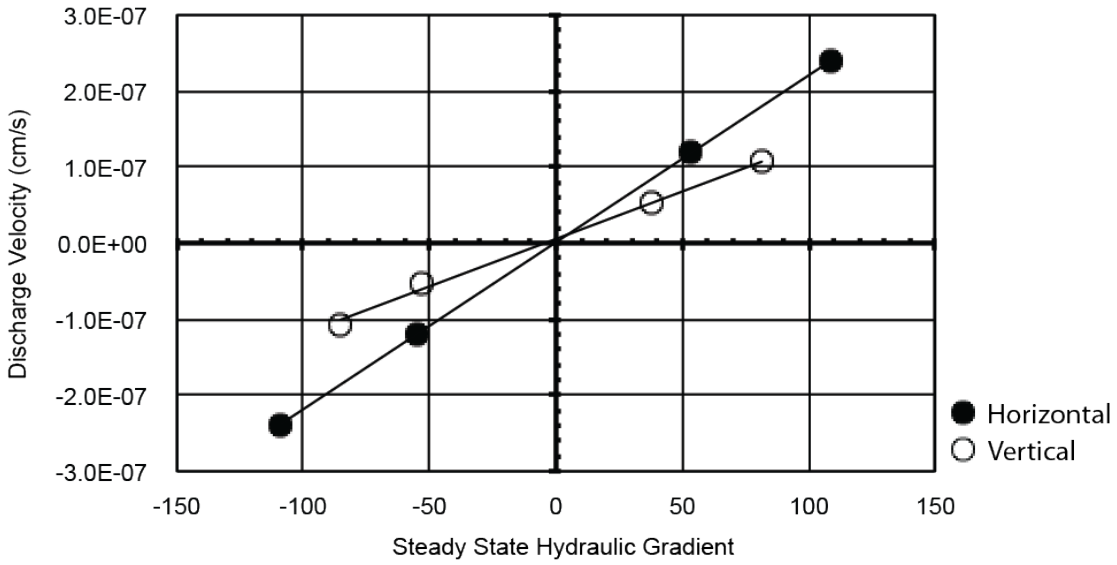

Figure A 13. Hydraulic gradient vs. discharge velocity (Sample 316-C0006E-34X-3, 95 cm).

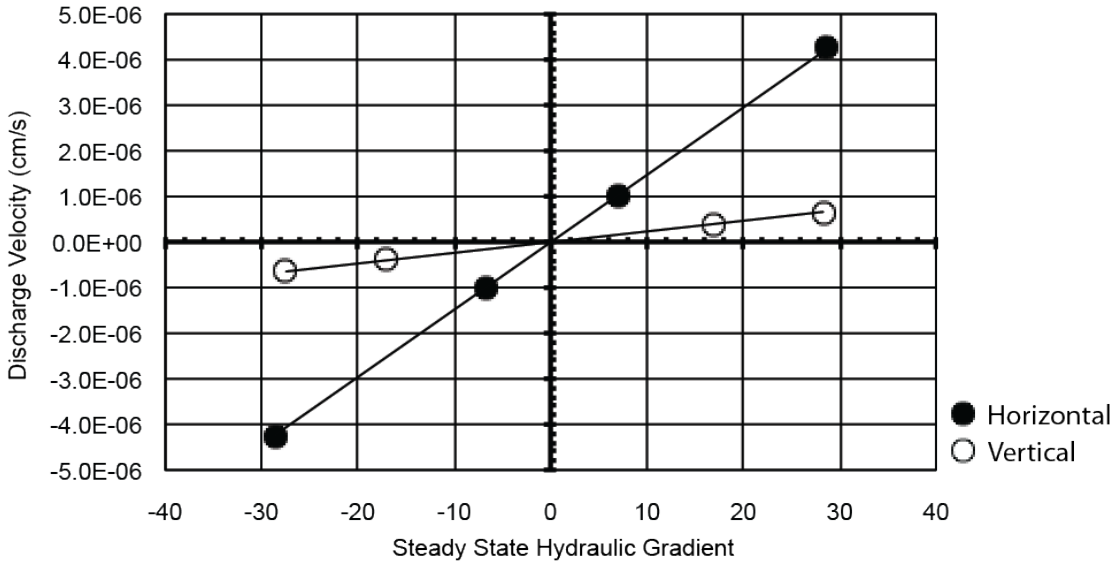

Figure A 14. Hydraulic gradient vs. discharge velocity (Sample 316-C0006E-39X-3, 48 cm).

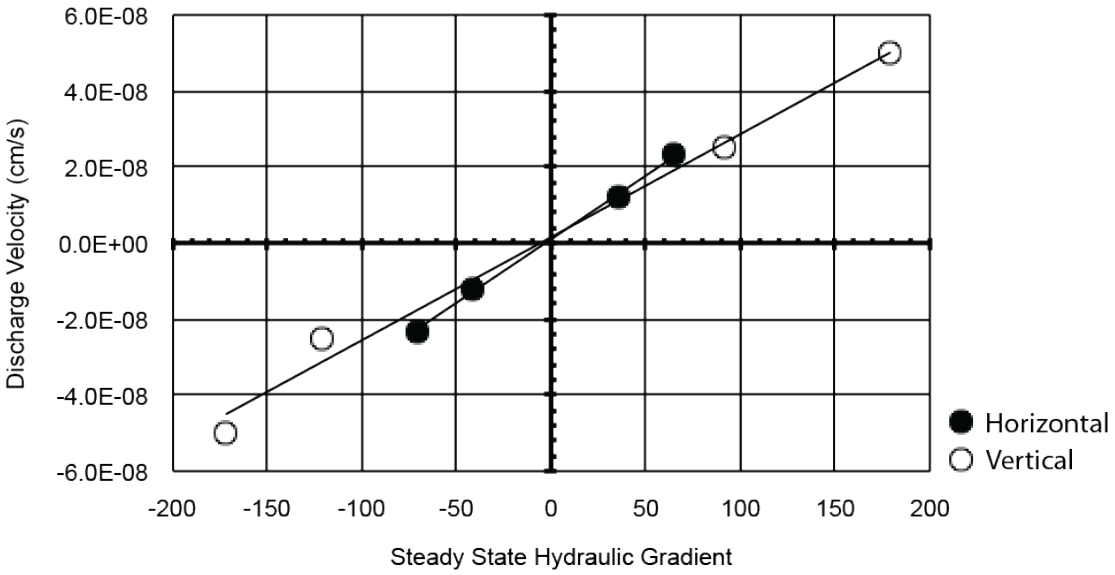

Figure A 15. Hydraulic gradient vs. discharge velocity (Sample 316-C0006F-19R-2, 61 cm)

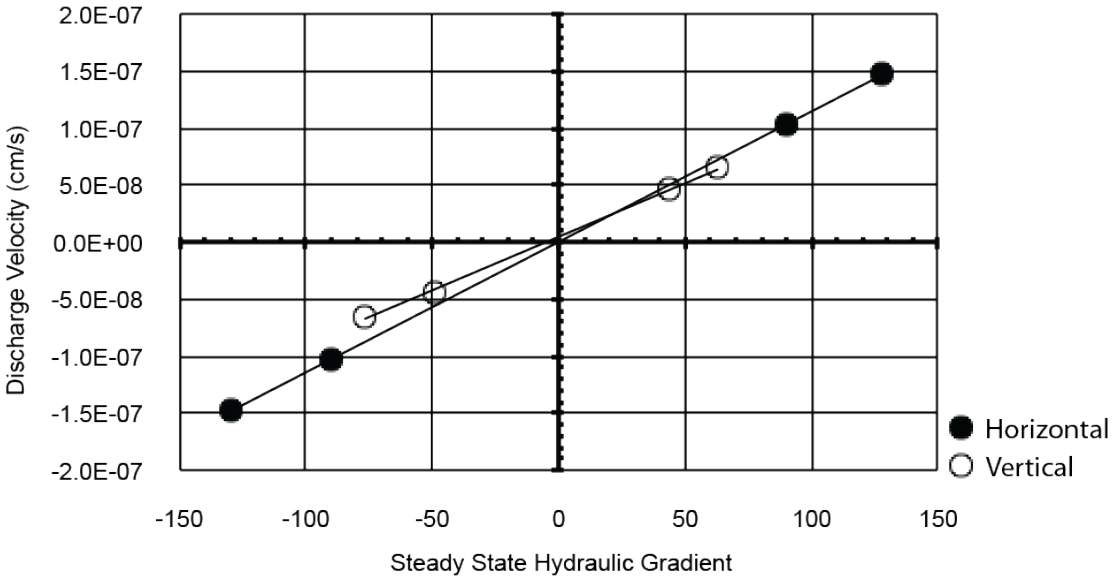

Figure A 16. Hydraulic gradient vs. discharge velocity (Sample 316-C0007D-23R-2, 97 cm).

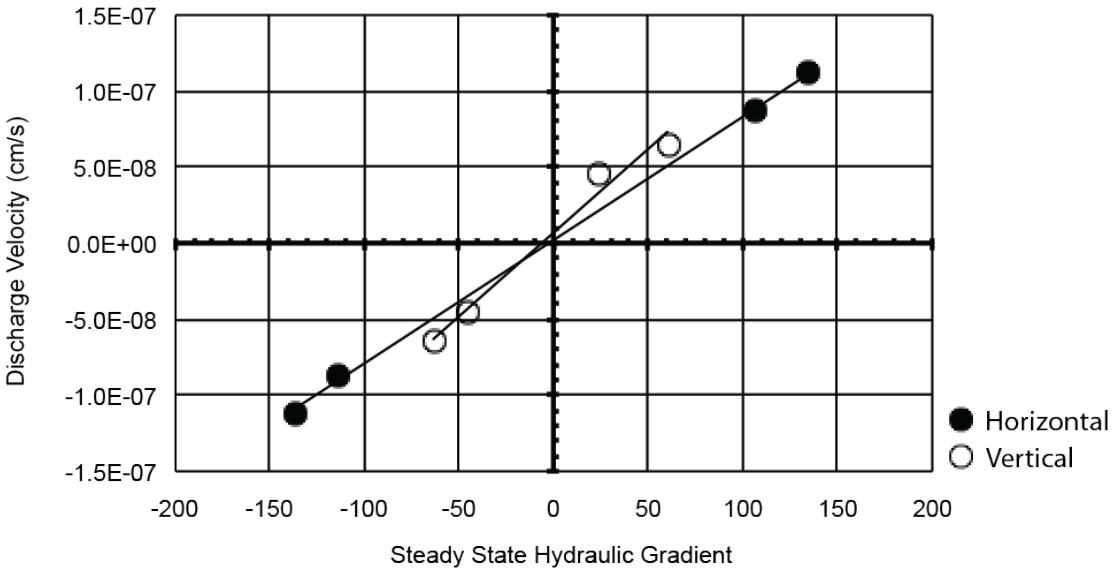

Figure A 17. Hydraulic gradient vs. discharge velocity (Sample 316-C0007D-25R-2, 66 cm).

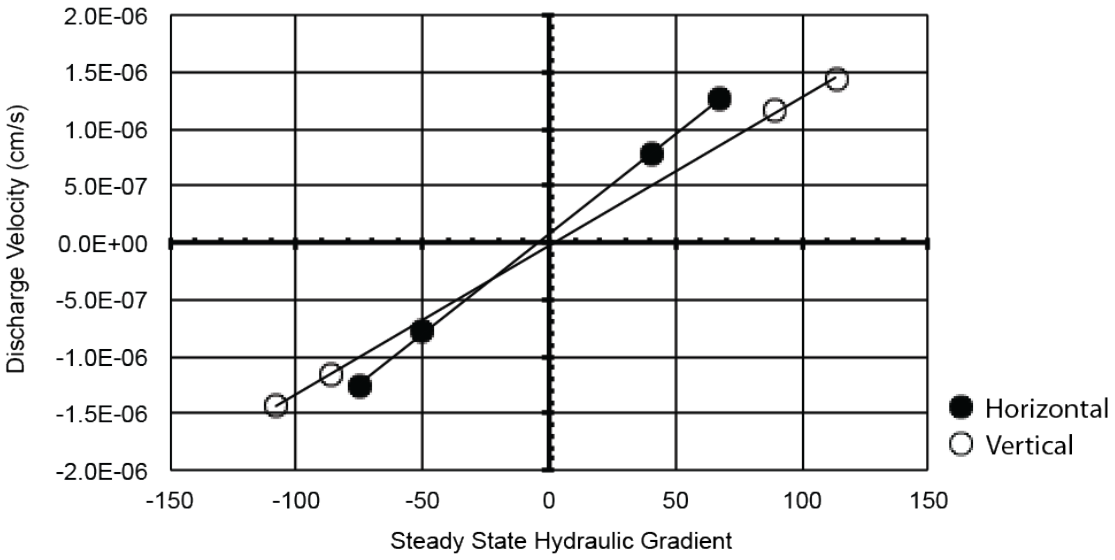

Figure A 18. Hydraulic gradient vs. discharge velocity (Sample 333-C0011D-2H-7, 0 cm).

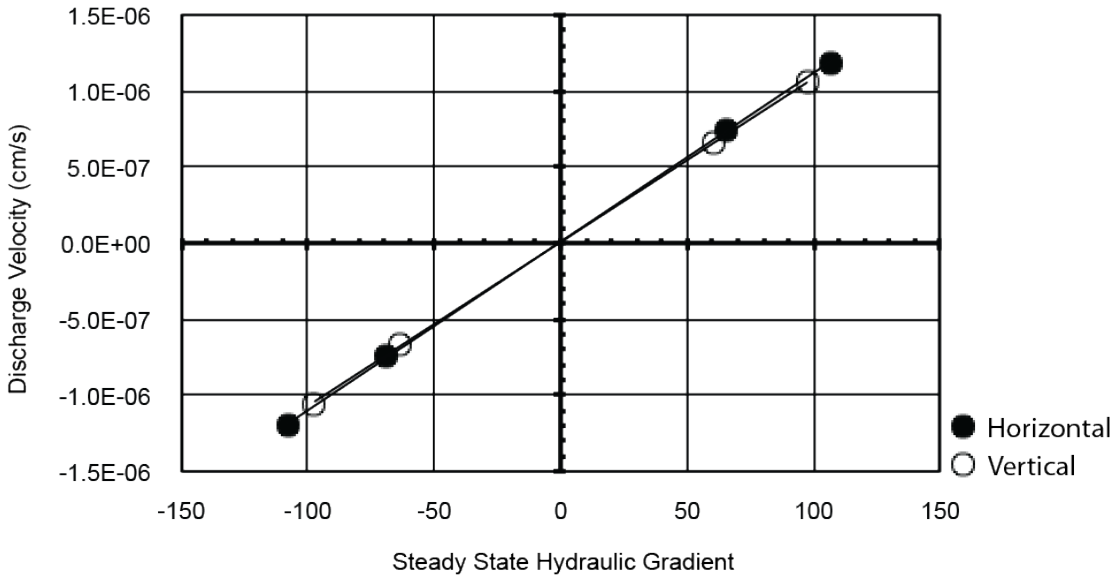

Figure A 19. Hydraulic gradient vs. discharge velocity (Sample 333-C0011D-19H-5, 99 cm).

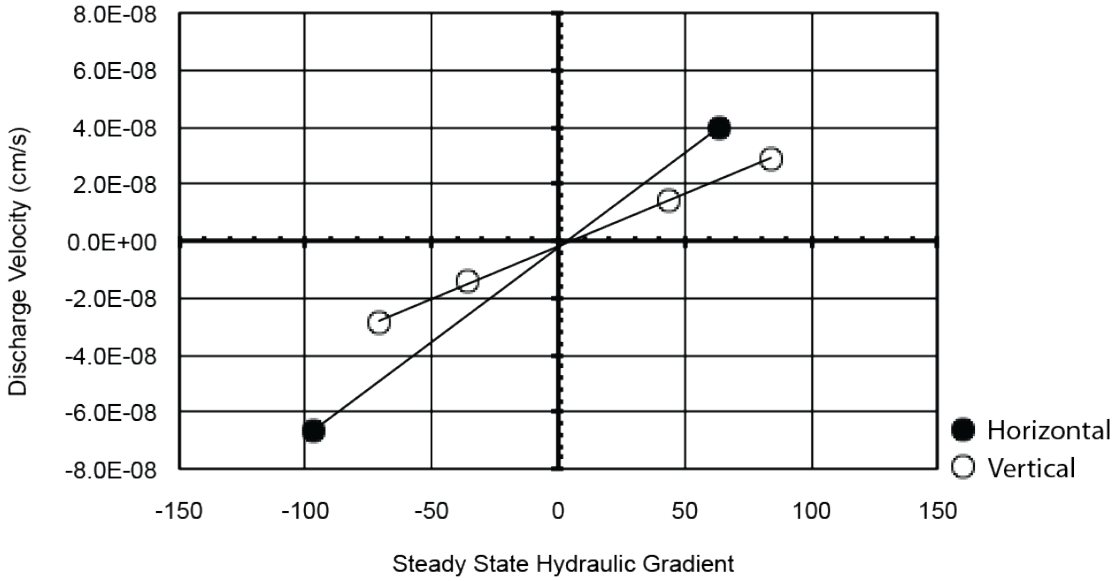

Figure A 20. Hydraulic gradient vs. discharge velocity (Sample 333-C0011D-41X-6, 121 cm).

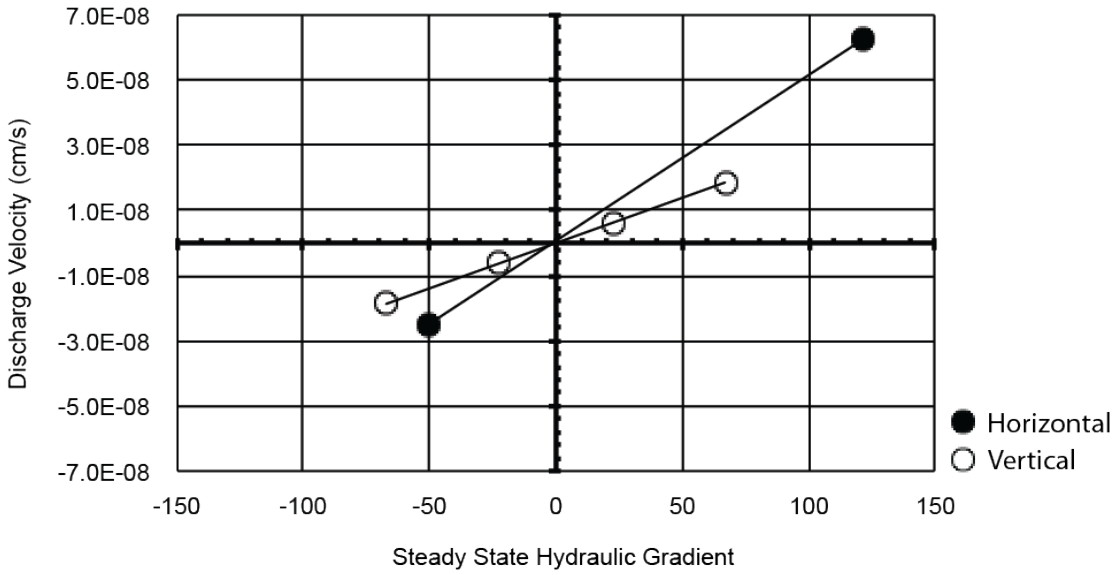

Figure A 21. Hydraulic gradient vs. discharge velocity (Sample 333-C0011D-49X-4, 51 cm).

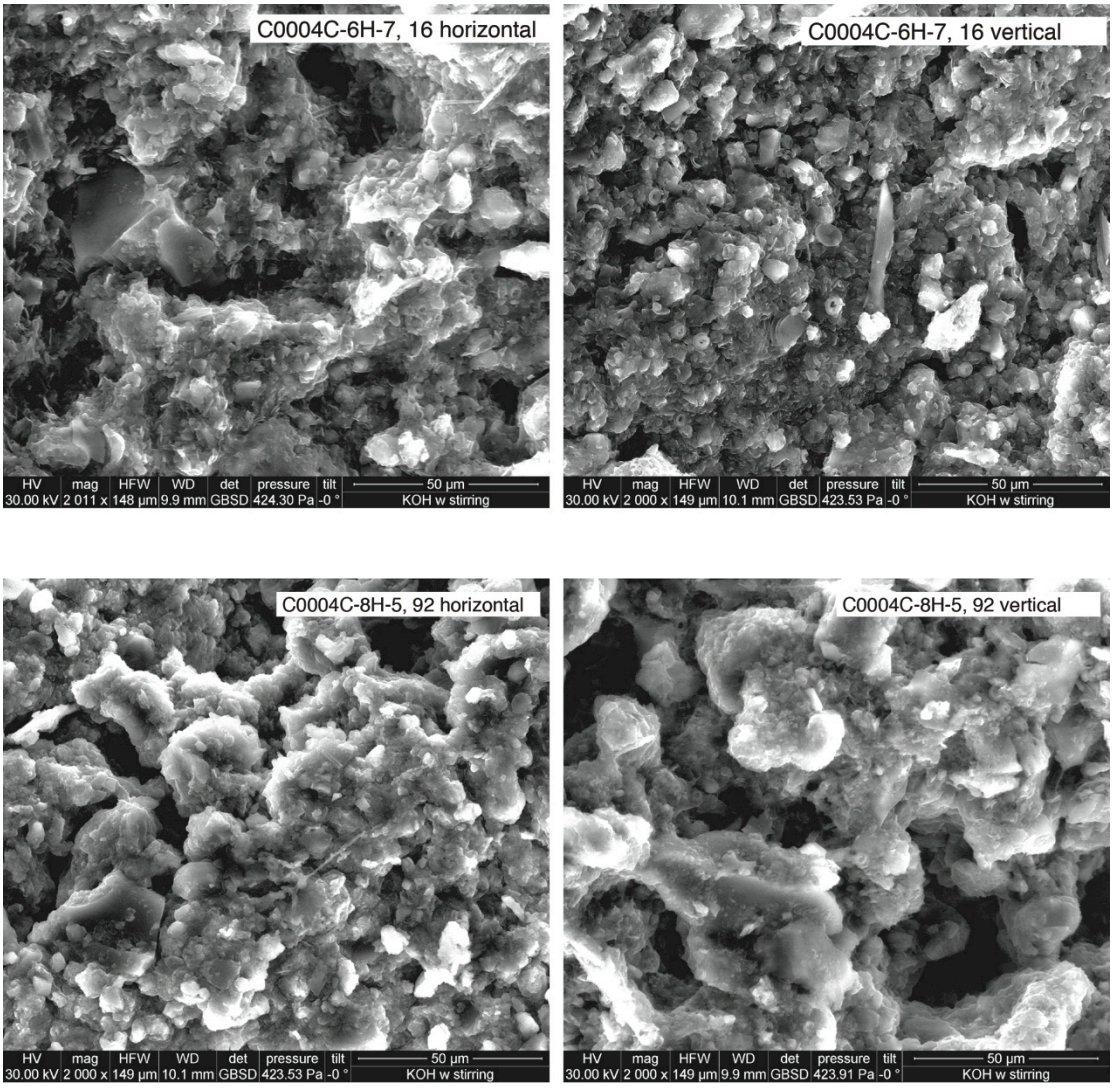

Figure A 22. Environmental scanning electron microscope images for all specimens tested for permeability, Sites C0004, C0008, C0006, C0007 and C0011. Sections were cut parallel and perpendicular to core axis. (Continued on next eleven pages).

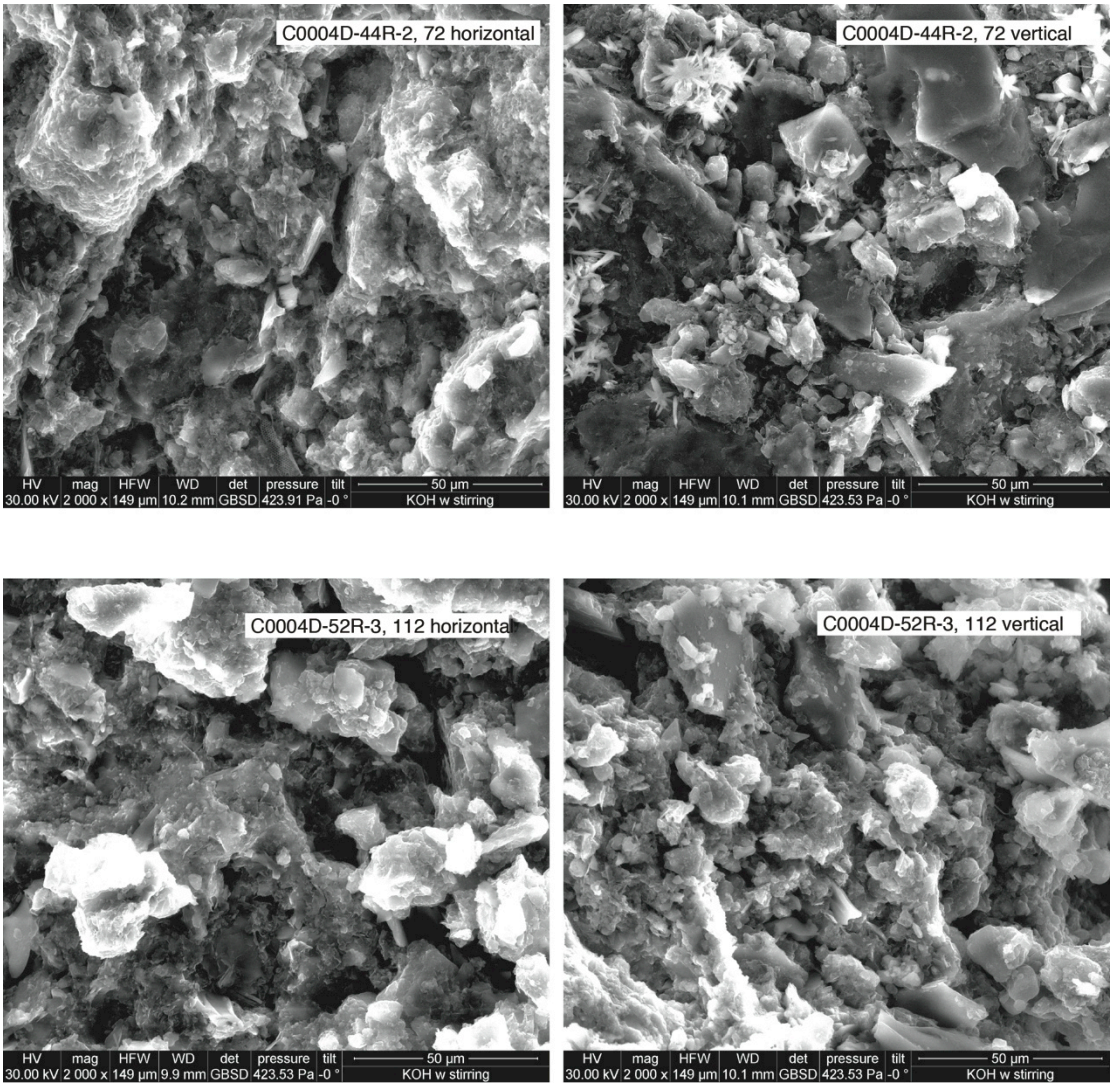

Figure A 22 (cont'd).

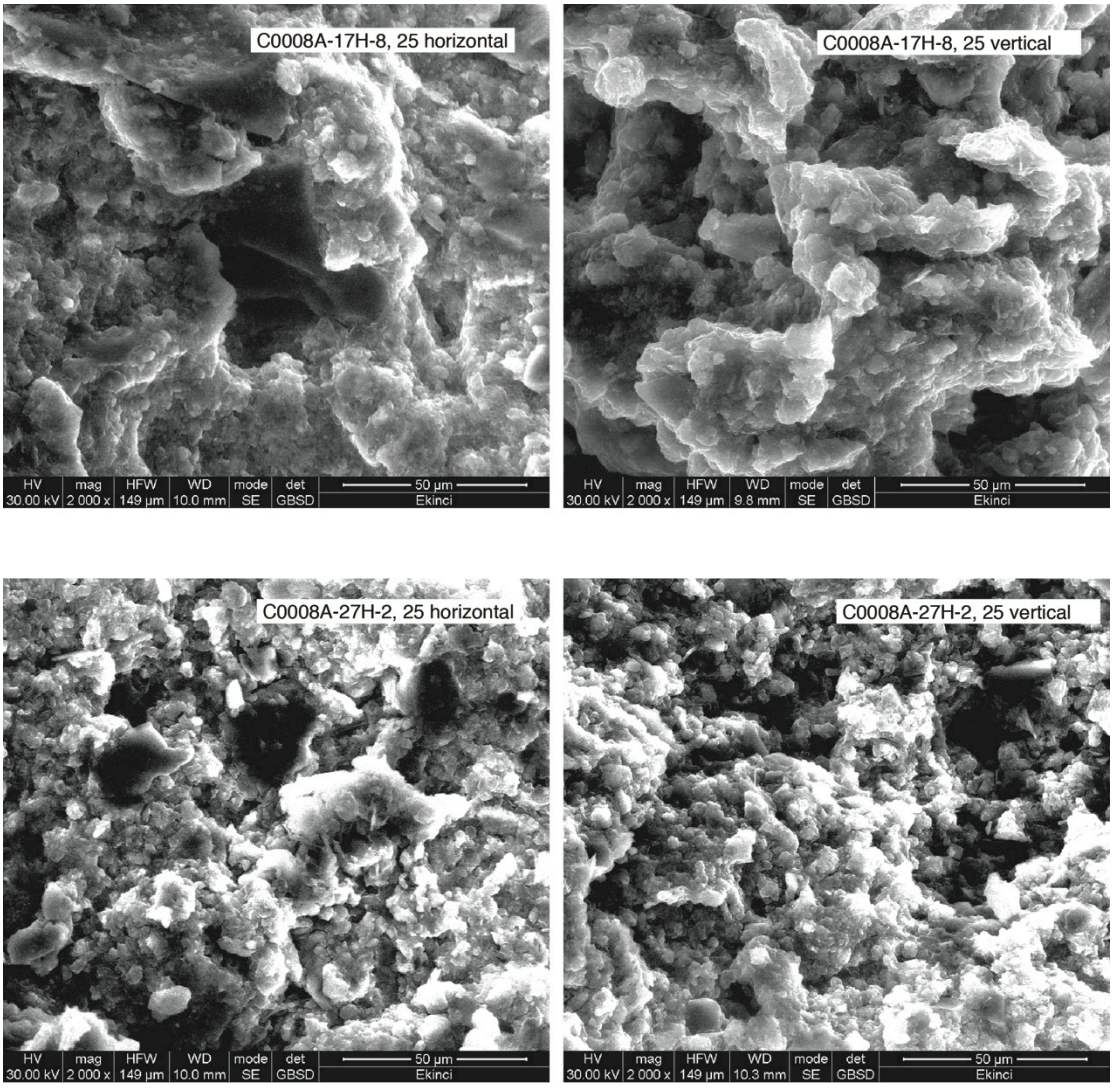

Figure A 22 (cont'd).

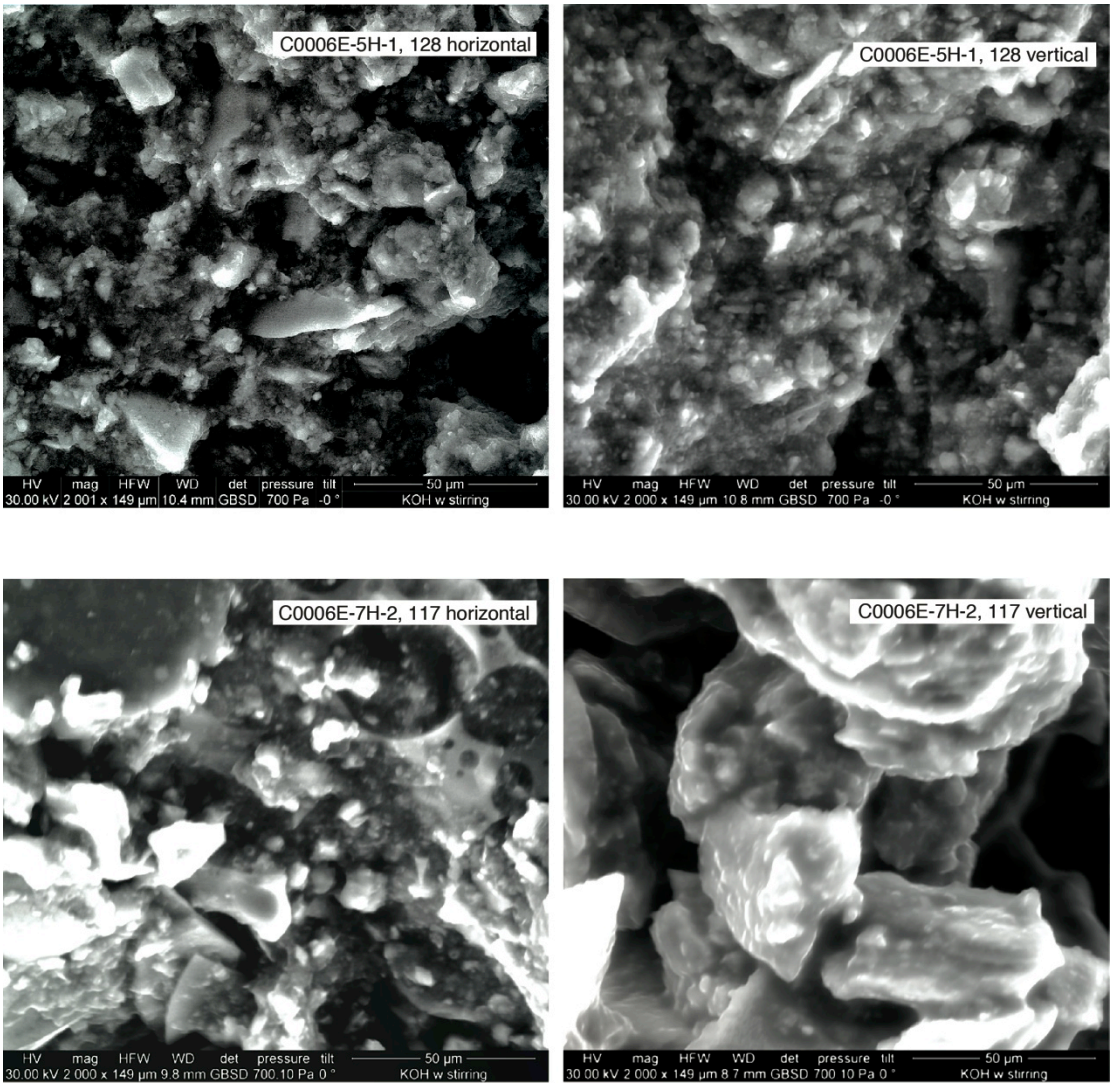

Figure A 22 (cont'd).

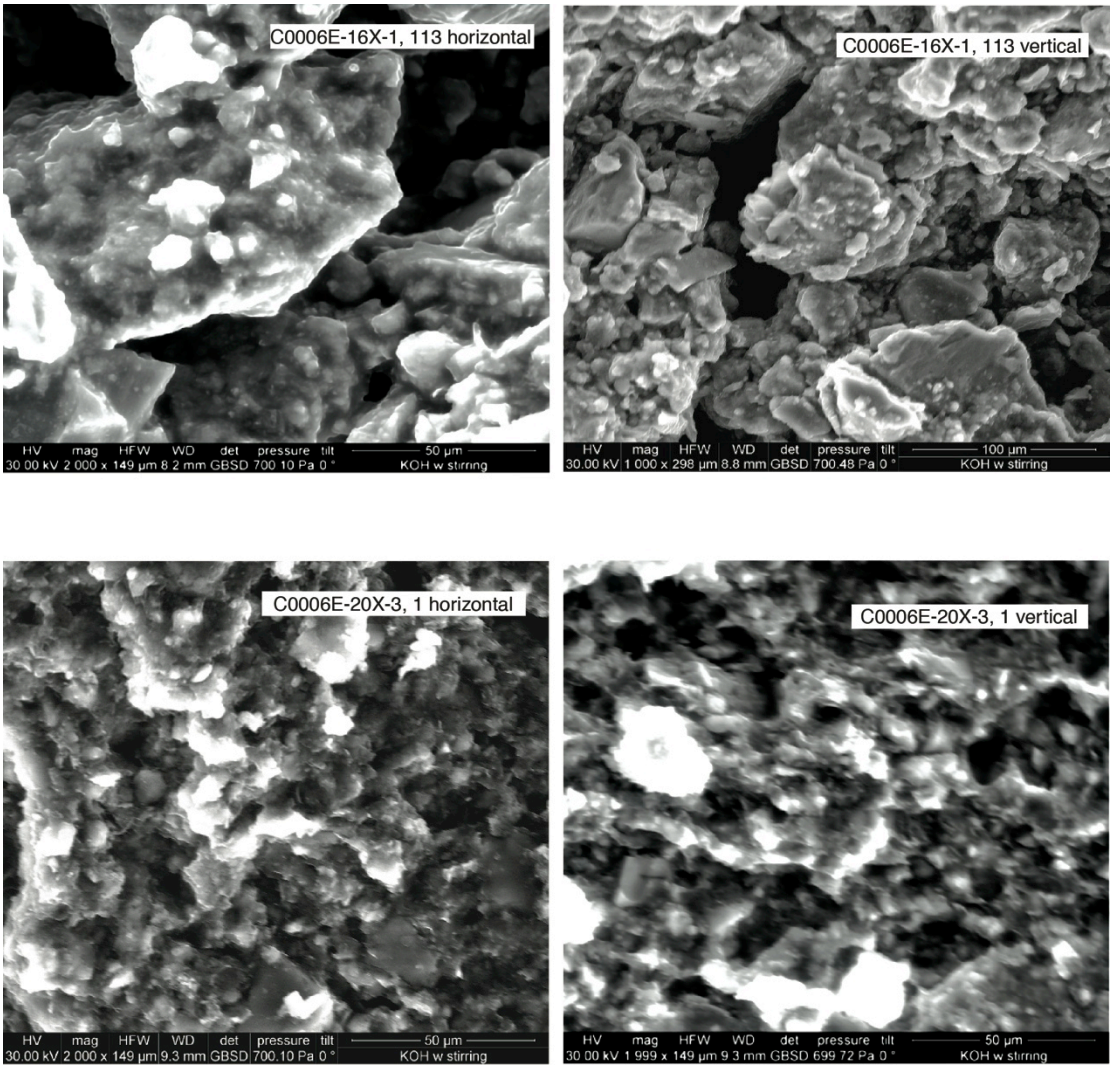

Figure A 22 (cont'd).

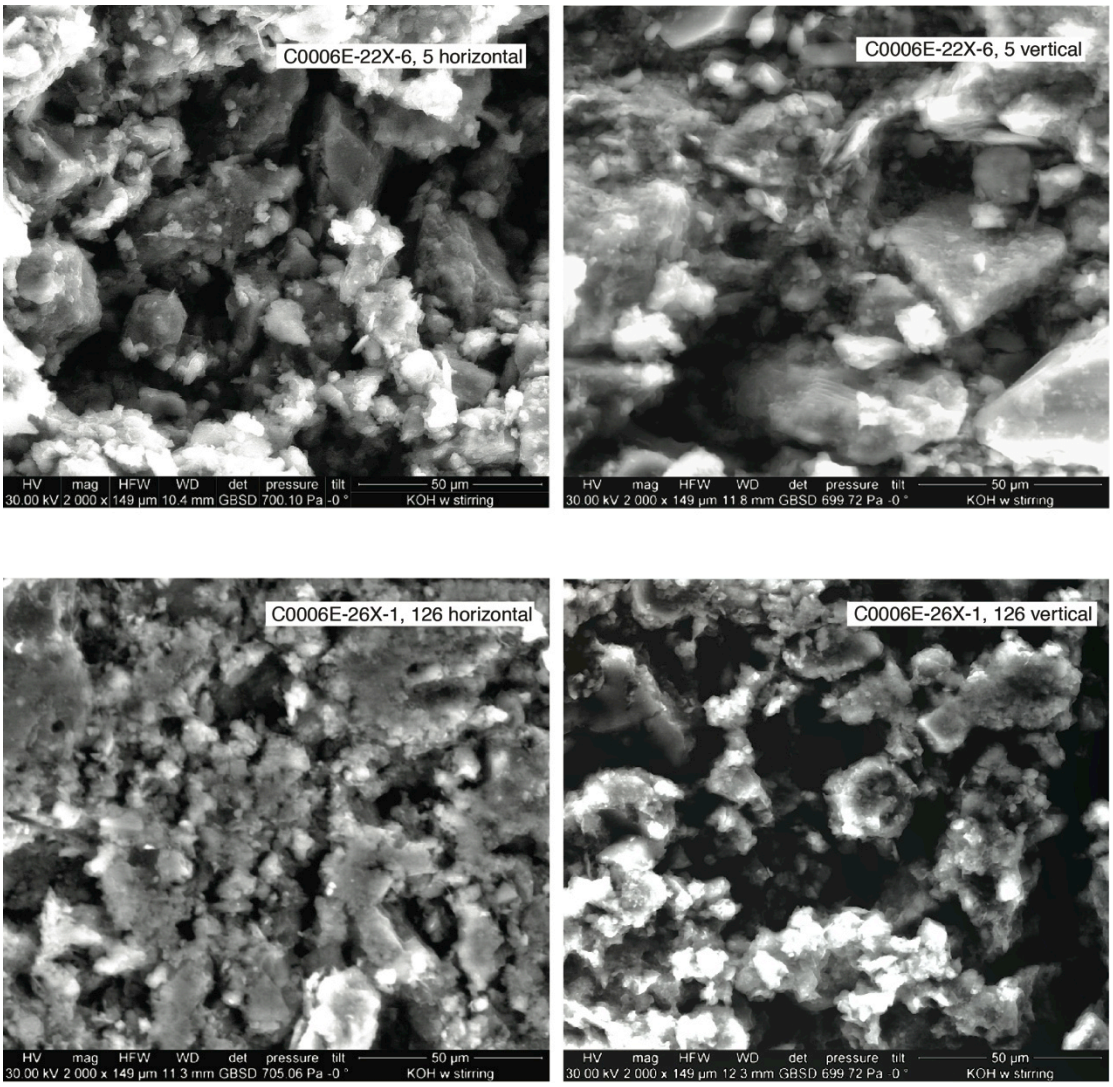

Figure A 22 (cont'd).

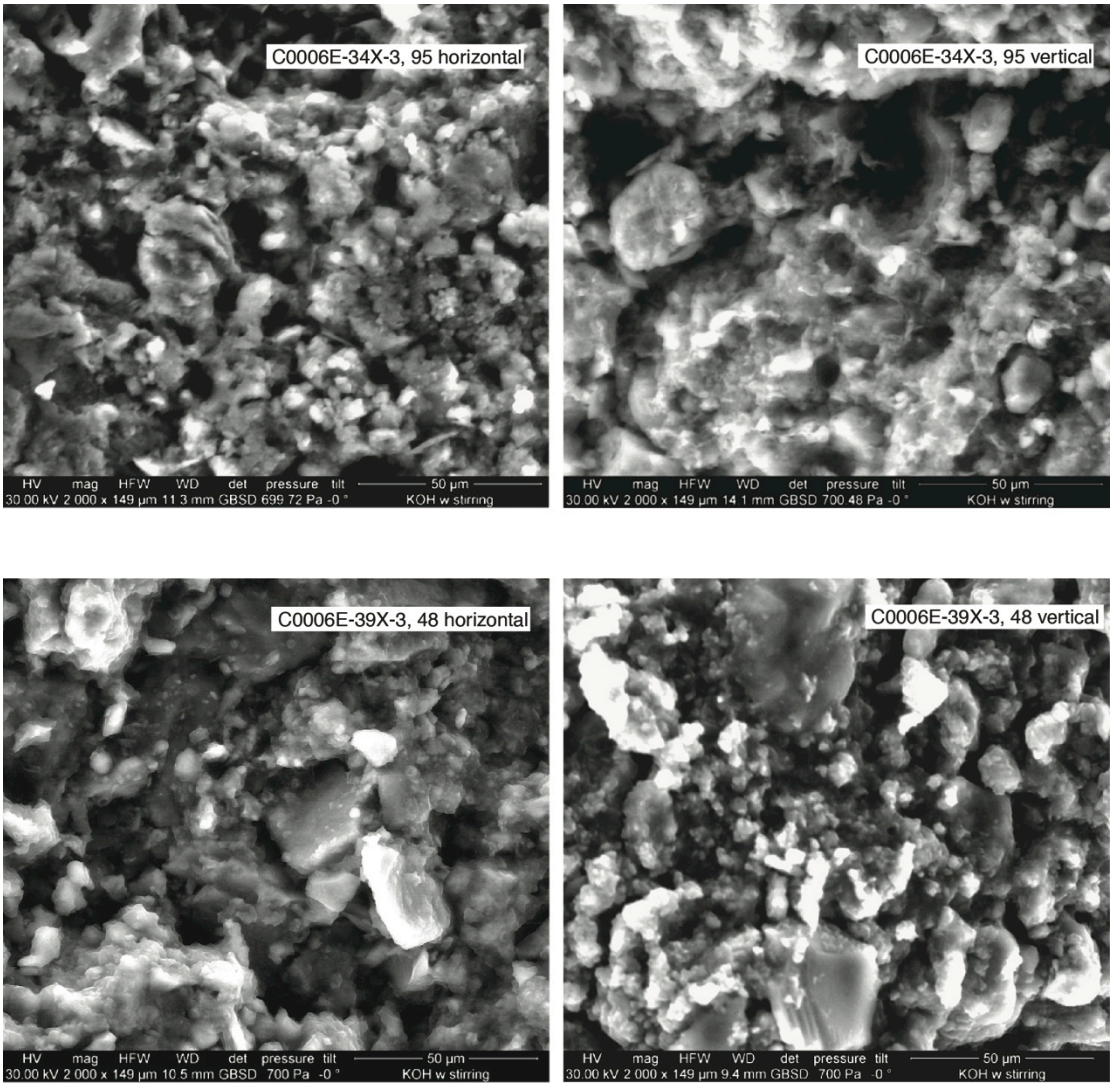

Figure A 22 (cont'd).

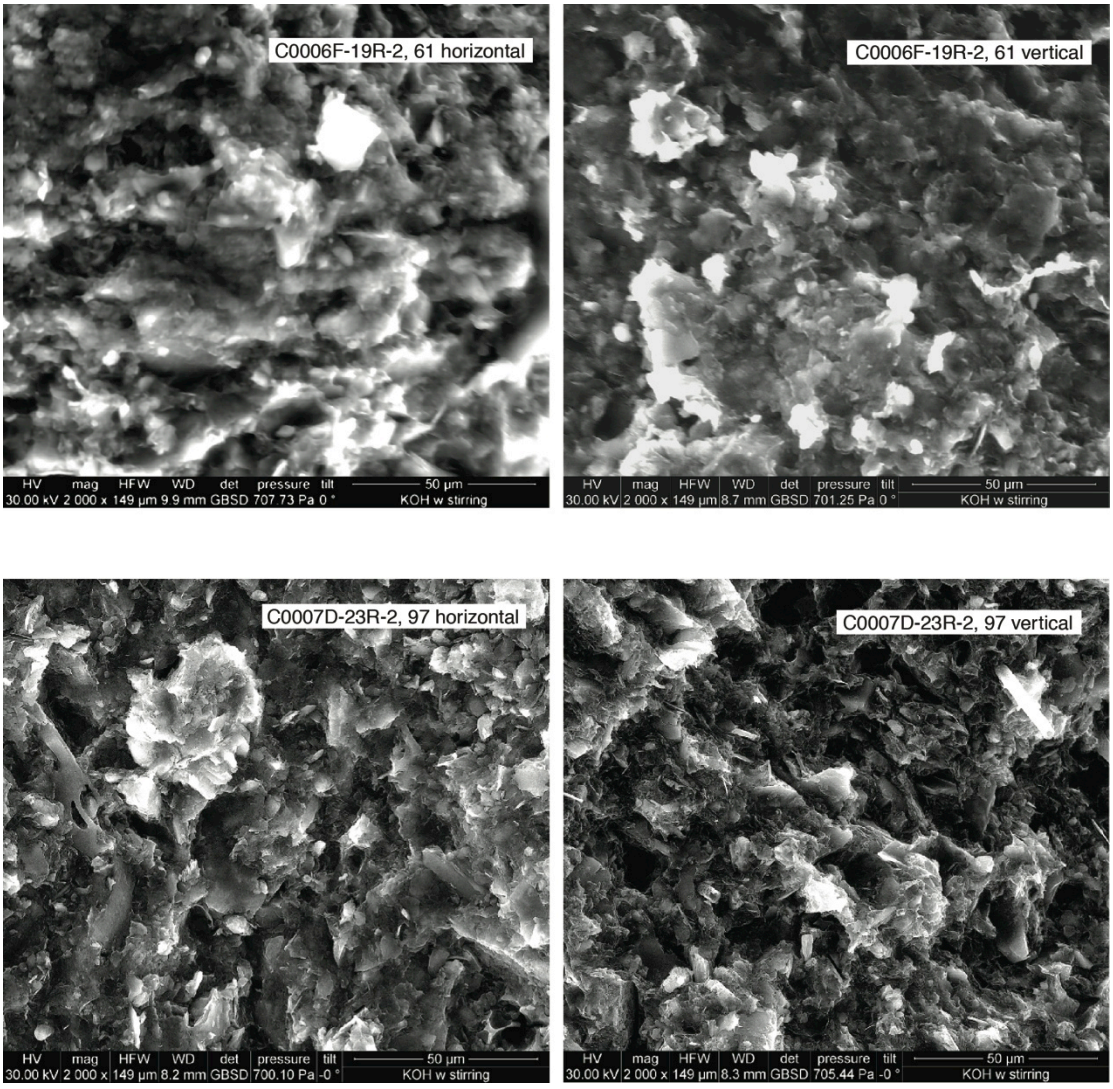

Figure A 22 (cont'd).

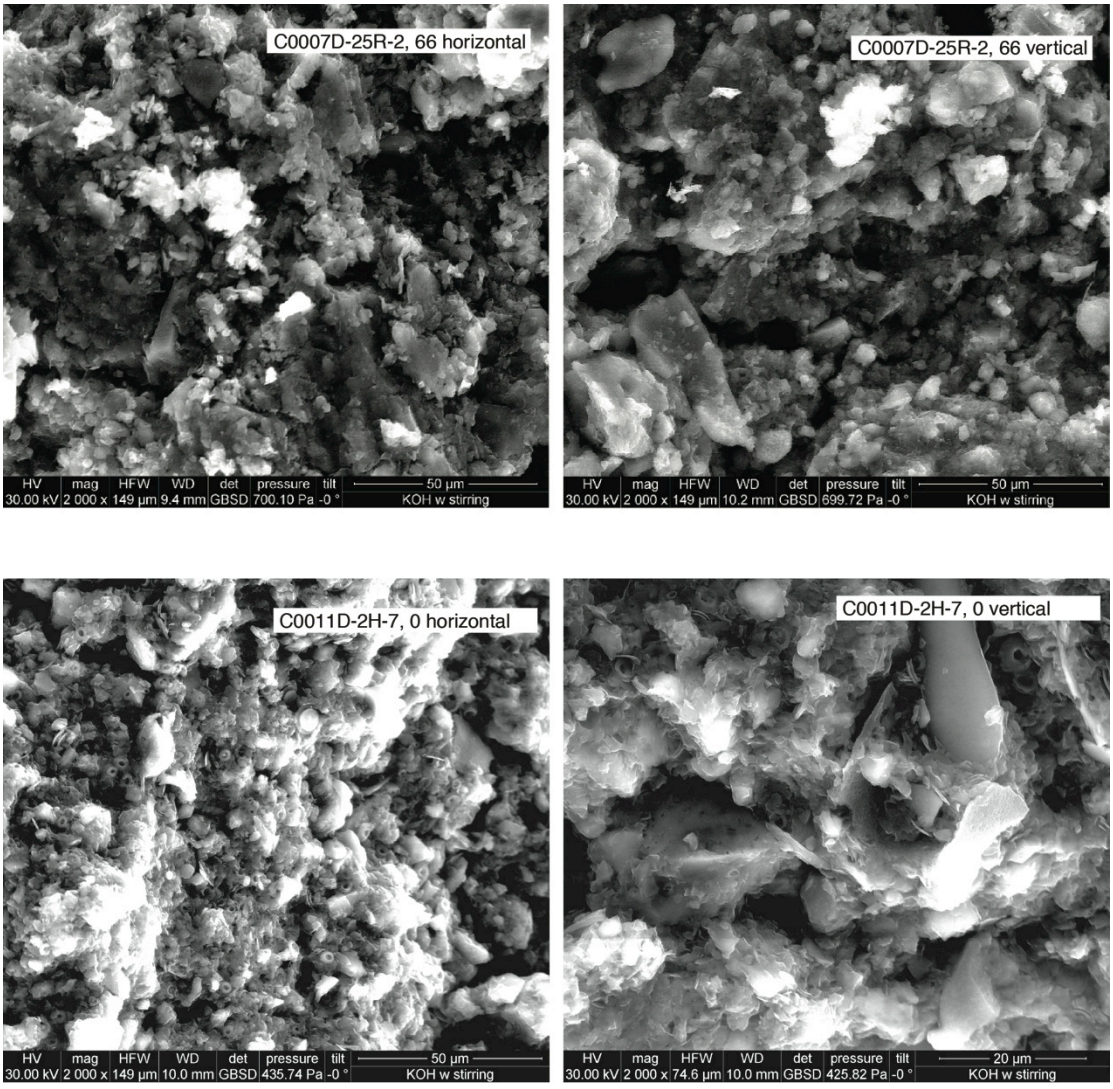

Figure A 22 (cont'd).

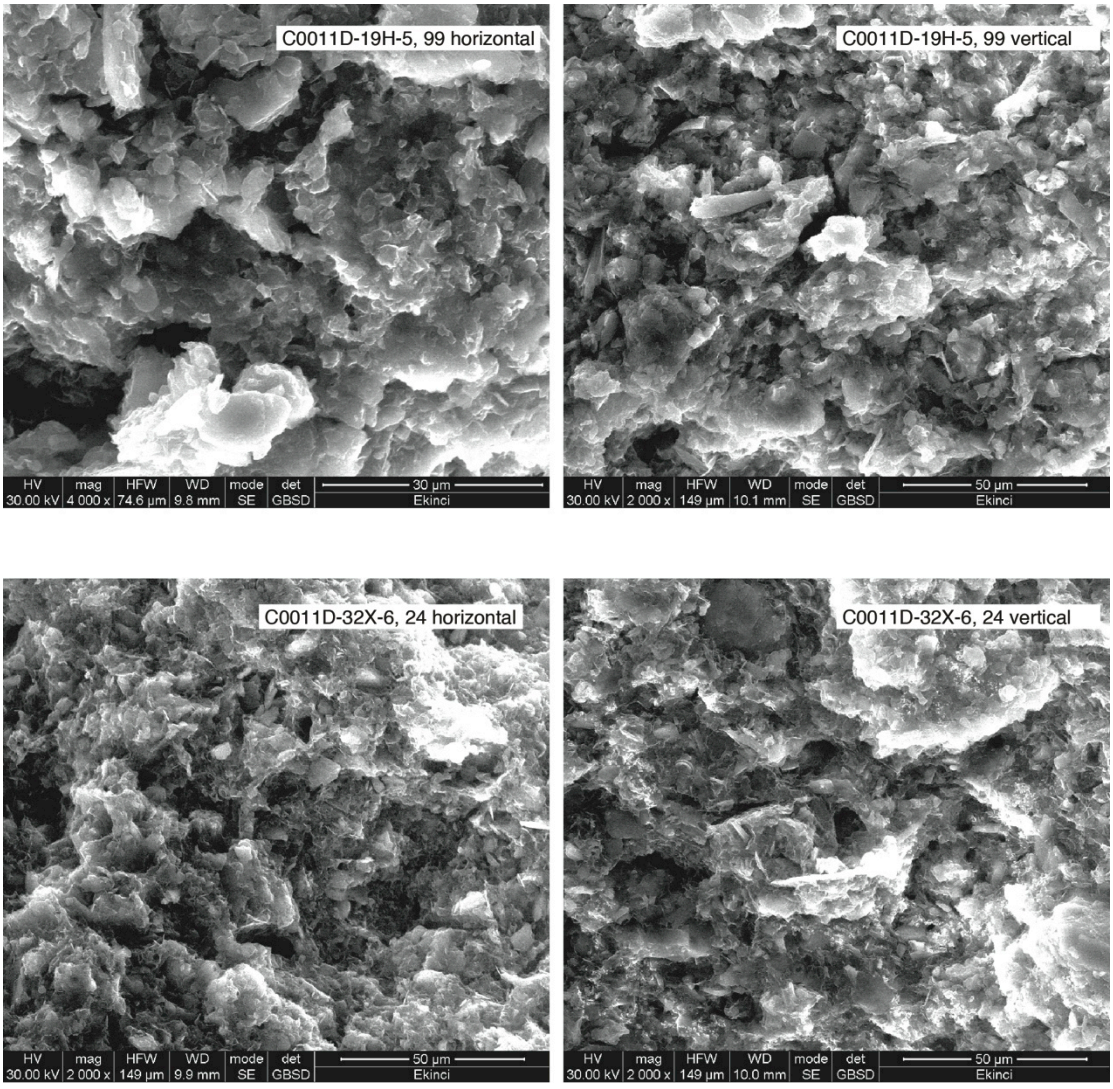

Figure A 22 (cont'd).

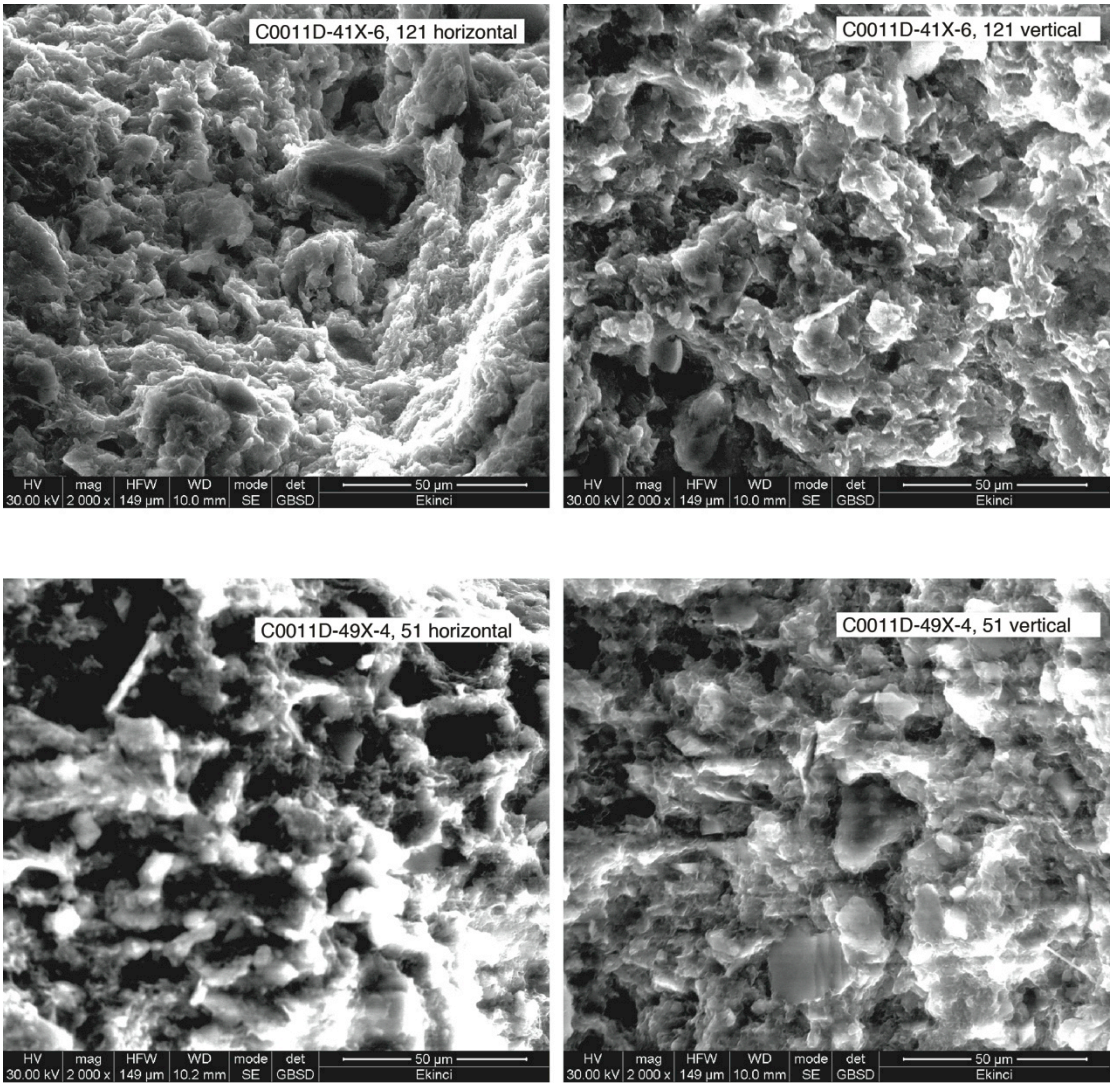

Figure A 22 (cont'd).

Table A1. Results of individual tests, Sites C0004, C0008, C0006, C0007 and C0011. (Continued on next nine pages).

Core, section, interval (cm)	Test run	Volumetric flow rate (cm^3/min)	Discharge velocity (cm/s)	Head Difference (cm)	Hydraulic gradient	Hydraulic Conductivity (cm/s)	Intrinsic Permeability (m^2)
316-C0004C-							
6H-7, 16 vertical	1	0.001	1.55E-06	857	141.19	1.10E-08	1.12E-17
	2	0.0007	1.09E-06	594	97.86	1.11E-08	1.13E-17
	3	-0.001	-1.55E-06	-850	-140.03	1.11E-08	1.13E-17
	4	-0.0007	-1.08E-06	-591	-97.36	1.11E-08	1.13E-17
					Average:	1.11E-08	1.13E-17
8H-5, 92 vertical	1	0.001	1.34E-06	464	86.57	1.55E-08	1.58E-17
	2	0.0008	1.07E-06	368	68.66	1.56E-08	1.59E-17
	3	-0.001	-1.34E-06	-447	-83.40	1.61E-08	1.64E-17
	4	-0.0008	-1.07E-06	-359	-66.98	1.60E-08	1.63E-17
					Average:	1.58E-08	1.61E-17
8H-5, 92 horizontal	1	0.001	9.18E-07	448	90.87	1.01E-08	1.03E-17
	2	0.0008	7.31E-07	350	70.99	1.03E-08	1.05E-17
	3	-0.001	-9.17E-07	-459	-93.10	9.85E-09	1.01E-17
	4	-0.0008	-7.34E-07	-365	-74.04	9.91E-09	1.01E-17
					Average:	1.00E-08	1.02E-17
316-C0004D-							
44R-2, 72 vertical	1	0.0005	6.19E-07	219	65.77	9.41E-09	9.60E-18
	2	0.0008	9.90E-07	340	102.10	9.70E-09	9.90E-18
	3	-0.0005	-6.19E-07	-228	-68.47	9.04E-09	9.22E-18
	4	-0.0008	-9.90E-07	-362	-108.71	9.11E-09	9.30E-18
					Average:	9.32E-09	9.51E-18
52R-3, 112 vertical	1	0.0002	2.82E-07	496	152.62	1.85E-09	1.89E-18
	2	0.0001	1.41E-07	251	77.23	1.83E-09	1.87E-18
	3	-0.0002	-2.82E-07	-506	-155.69	1.81E-09	1.85E-18
	4	-0.0001	-1.41E-07	-256	-78.77	1.79E-09	1.83E-18
					Average:	1.82E-09	1.86E-18

Core, section, interval (cm)	Test run	Volumetric flow rate (cm^3/min)	Discharge velocity (cm/s)	Head Difference (cm)	Hydraulic gradient	Hydraulic Conductivity (cm/s)	Intrinsic Permeability (m^2)
316-C0008A-							
17H-8, 25 vertical	1	0.0001	1.31E-07	120	18.69	7.03E-09	7.17E-18
	2	0.0003	3.94E-07	356	55.45	7.10E-09	7.24E-18
	3	-0.0001	-1.31E-07	-145	-22.59	5.81E-09	5.93E-18
	4	-0.0003	-3.94E-07	-401	-62.46	6.31E-09	6.44E-18
					Average:	6.56E-09	6.70E-18
27H-2, 25 vertical	1	0.0001	1.26E-07	57	10.36	1.22E-08	1.24E-17
	2	0.0004	5.03E-07	261	47.45	1.06E-08	1.08E-17
	3	-0.0003	-3.80E-07	-197	-35.82	1.06E-08	1.08E-17
	4	-0.0005	-6.30E-07	-333	-60.55	1.04E-08	1.06E-17
					Average:	1.10E-08	1.12E-17
316-C0006E-							
5H-1, 128 vertical	1	0.007	3.52E-06	39	7.94	4.43E-07	4.52E-16
	2	0.003	1.51E-06	19	3.87	3.89E-07	3.97E-16
	3	-0.007	-3.52E-06	-37	-7.54	4.67E-07	4.77E-16
	4	-0.003	-1.51E-06	-17	-3.46	4.35E-07	4.44E-16
					Average:	4.34E-07	4.42E-16
5H-1, 128 horizontal	1	0.007	8.39E-06	52	10.28	8.16E-07	8.33E-16
	2	0.003	3.59E-06	22	4.35	8.26E-07	8.43E-16
	3	-0.007	-8.39E-06	-51	-10.08	8.32E-07	8.49E-16
	4	-0.003	-3.59E-06	-22	-4.35	8.26E-07	8.43E-16
					Average:	8.25E-07	8.42E-16
7H-2, 117 vertical	1	0.003	3.79E-06	268	52.55	7.21E-08	7.36E-17
	2	0.001	1.26E-06	90	17.65	7.15E-08	7.30E-17
	3	-0.003	-3.79E-06	-258	-50.59	7.49E-08	7.64E-17
	4	-0.001	-1.26E-06	-69	-13.53	9.33E-08	9.52E-17
					Average:	**7.80E-08**	**7.95E-17**
16X-1, 113 vertical	1	0.005	2.61E-06	130	24.67	1.06E-07	1.08E-16
	2	0.003	1.58E-06	80	15.18	1.04E-07	1.06E-16
	3	-0.005	-2.63E-06	-132	-25.05	1.05E-07	1.07E-16
	4	-0.003	-1.57E-06	-81	-15.37	1.02E-07	1.04E-16
					Average:	**1.04E-07**	**1.06E-16**

Core, section, interval (cm)	Test run	Volumetric flow rate (cm^3/min)	Discharge velocity (cm/s)	Head Difference (cm)	Hydraulic gradient	Hydraulic Conductivity (cm/s)	Intrinsic Permeability (m^2)
16X-1,113 horizontal	1	0.005	6.94E-06	12	2.78	2.50E-06	2.55E-15
	2	0.008	1.11E-05	24	5.56	2.00E-06	2.04E-15
	3	-0.008	-1.11E-05	-25	-5.79	1.92E-06	1.96E-15
	4	-0.005	-6.93E-06	-16	-3.70	1.87E-06	1.91E-15
					Average:	**2.07E-06**	**2.11E-15**
20X-3, 1 vertical	1	0.0002	3.21E-07	858	203.32	1.58E-09	1.61E-18
	2	0.0001	1.60E-07	423	100.24	1.60E-09	1.63E-18
	3	-0.0002	-3.20E-07	-722	-171.09	1.87E-09	1.91E-18
	4	-0.0001	-1.60E-07	-380	-90.05	1.78E-09	1.82E-18
					Average:	**1.71E-09**	**1.74E-18**
20X-3, 1 horizontal	1	0.0001	1.56E-07	265	50.57	3.08E-09	3.14E-18
	2	0.0002	3.12E-07	512	97.71	3.19E-09	3.26E-18
	3	-0.0001	-1.56E-07	-251	-47.90	3.25E-09	3.32E-18
	4	-0.0002	-3.12E-07	-498	-95.04	3.28E-09	3.35E-18
					Average:	**3.20E-09**	**3.27E-18**
22X-6, 5 vertical	1	0.003	3.96E-06	144	25.90	1.53E-07	1.56E-16
	2	0.007	9.23E-06	331	59.53	1.55E-07	1.58E-16
	3	-0.003	-3.96E-06	-142	-25.54	1.55E-07	1.58E-16
	4	-0.007	-9.26E-06	-330	-59.35	1.56E-07	1.59E-16
					Average:	**1.55E-07**	**1.58E-16**
22X-6, 5 horizontal	1	0.003	4.45E-06	425	120.06	3.71E-08	3.79E-17
	2	0.001	1.48E-06	139	39.27	3.78E-08	3.86E-17
	3	-0.003	-4.46E-06	-424	-119.77	3.72E-08	3.80E-17
	4	-0.001	-1.49E-06	-143	-40.40	3.68E-08	3.76E-17
					Average:	**3.72E-08**	**3.80E-17**
26X-1, 126 vertical	1	0.0003	3.56E-07	596	98.03	3.63E-09	3.70E-18
	2	0.0001	1.19E-07	194	31.91	3.72E-09	3.80E-18
	3	-0.0003	-3.56E-07	-603	-99.18	3.59E-09	3.66E-18
	4	-0.0001	-1.18E-07	-199	-32.73	3.62E-09	3.69E-18
					Average:	**3.64E-09**	**3.71E-18**

Core, section, interval (cm)	Test run	Volumetric flow rate (cm^3/min)	Discharge velocity (cm/s)	Head Difference (cm)	Hydraulic gradient	Hydraulic Conductivity (cm/s)	Intrinsic Permeability (m^2)
26X-1, 126 horizontal	1	0.0003	5.17E-07	540	121.35	4.26E-09	4.35E-18
	2	0.0001	1.72E-07	180	40.45	4.26E-09	4.35E-18
	3	-0.0003	-5.17E-07	-529	-118.88	4.35E-09	4.44E-18
	4	-0.0001	-1.72E-07	-178	-40.00	4.31E-09	4.40E-18
					Average:	**4.30E-09**	**4.38E-18**
34X-3, 95 vertical	1	0.0001	5.31E-08	304	38.19	1.39E-09	1.42E-18
	2	0.0002	1.06E-07	648	81.41	1.30E-09	1.33E-18
	3	-0.0001	-5.32E-08	-419	-52.64	1.01E-09	1.03E-18
	4	-0.0002	-1.07E-07	-679	-85.30	1.25E-09	1.28E-18
					Average:	**1.24E-09**	**1.26E-18**
34X-3, 95 horizontal	1	0.0002	2.39E-07	455	109.11	2.19E-09	2.23E-18
	2	0.0001	1.20E-07	221	53.00	2.26E-09	2.31E-18
	3	0.0002	-2.39E-07	-453	-108.63	2.20E-09	2.24E-18
	4	0.0001	-1.20E-07	-231	-55.40	2.16E-09	2.20E-18
					Average:	**2.20E-09**	**2.25E-18**
39X-3, 48 vertical	1	0.0005	6.56E-07	136	28.27	2.32E-08	2.37E-17
	2	0.0003	3.94E-07	81	16.84	2.34E-08	2.39E-17
	3	-0.0005	-6.56E-07	-132	-27.44	2.39E-08	2.44E-17
	4	-0.0003	-3.94E-07	-82	-17.05	2.31E-08	2.36E-17
					Average:	**2.34E-08**	**2.39E-17**
39X-3, 48 horizontal	1	0.0007	9.87E-07	34	6.95	1.42E-07	1.45E-16
	2	0.0003	4.24E-06	140	28.63	1.48E-07	1.51E-16
	3	-0.0007	-9.85E-07	-33	-6.75	1.46E-07	1.49E-16
	4	-0.0003	-4.24E-06	-140	-28.63	1.48E-07	1.51E-16
					Average:	**1.46E-07**	**1.49E-16**
316-C0006F- 19R-2, 61 vertical	1	0.00004	5.01E-08	755	178.91	2.80E-10	2.86E-19
	2	0.00002	2.50E-08	383	90.76	2.75E-10	2.81E-19
	3	-0.00004	-5.00E-08	-723	-171.33	2.92E-10	2.98E-19
	4	-0.00002	-2.50E-08	-510	-120.85	2.07E-10	2.11E-19
					Average:	**2.64E-10**	**2.69E-19**

Core, section, interval (cm)	Test run	Volumetric flow rate (cm^3/min)	Discharge velocity (cm/s)	Head Difference (cm)	Hydraulic gradient	Hydraulic Conductivity (cm/s)	Intrinsic Permeability (m^2)
19R-2, 6 horizontal	1	0.00002	2.35E-08	255	64.89	3.62E-10	3.69E-19
	2	0.00001	1.17E-08	142	36.13	3.25E-10	3.32E-19
	3	-0.00002	-2.35E-08	-279	-70.99	3.31E-10	3.38E-19
	4	-0.00001	-1.18E-08	-165	-41.98	2.80E-10	2.86E-19
					Average:	**3.25E-10**	**3.31E-19**
316-C0007D-23R-2, 97 vertical	1	0.0001	6.46E-08	421	62.74	1.03E-09	1.05E-18
	2	0.00007	4.53E-08	295	43.96	1.03E-09	1.05E-18
	3	-0.0001	-6.47E-08	-514	-76.60	8.44E-10	8.61E-19
	4	-0.00007	-4.53E-08	-333	-49.63	9.12E-10	9.31E-19
					Average:	**9.54E-10**	**9.73E-19**
23R-2, 97 horizontal	1	0.0001	1.47E-07	467	127.95	1.15E-09	1.17E-18
	2	0.00007	1.03E-07	329	90.14	1.14E-09	1.16E-18
	3	-0.0001	-1.47E-07	-472	-129.32	1.14E-09	1.16E-18
	4	-0.00007	-1.03E-07	-327	-89.59	1.15E-09	1.17E-18
					Average:	**1.15E-09**	**1.17E-18**
25R-2, 66 vertical	1	0.0001	6.51E-08	516	60.28	1.08E-09	1.10E-18
	2	0.00007	4.55E-08	207	24.18	1.88E-09	1.92E-18
	3	-0.0001	-6.47E-08	-543	-63.43	1.02E-09	1.04E-18
	4	-0.00007	-4.54E-08	-389	-45.44	9.99E-10	1.02E-18
					Average:	**1.24E-09**	**1.27E-18**
25R-2, 66 horizontal	1	0.00007	8.69E-08	445	106.46	8.16E-10	8.33E-19
	2	0.00009	1.12E-07	559	133.73	8.35E-10	8.52E-19
	3	-0.00007	-8.69E-08	-473	-113.16	7.68E-10	7.84E-19
	4	-0.00009	-1.12E-07	-572	-136.84	8.16E-10	8.33E-19
					Average:	**8.09E-10**	**8.25E-19**
333-C0011D- 2H-7, 0 vertical	1	0.001	1.44E-06	660	113.21	1.27E-08	1.30E-17
	2	0.0008	1.15E-06	520	89.19	1.29E-08	1.32E-17
	3	-0.001	-1.44E-06	-630	-108.06	1.33E-08	1.36E-17
	4	-0.0008	-1.15E-06	-501	-85.93	1.34E-08	1.37E-17
					Average:	**1.31E-08**	**1.33E-17**

Core, section, interval (cm)	Test run	Volumetric flow rate (cm^3/min)	Discharge velocity (cm/s)	Head Difference (cm)	Hydraulic gradient	Hydraulic Conductivity (cm/s)	Intrinsic Permeability (m^2)
2H-7, 0 horizontal	1	0.0005	7.88E-07	218	40.60	1.94E-08	1.98E-17
	2	0.0008	1.26E-06	363	67.60	1.86E-08	1.90E-17
	3	-0.0005	-7.87E-07	-271	-50.47	1.56E-08	1.59E-17
	4	-0.0008	-1.26E-06	-402	-74.86	1.68E-08	1.71E-17
					Average:	**1.76E-08**	**1.80E-17**
19H-5, 99 vertical	1	0.0008	1.05E-06	633	97.38	1.08E-08	1.10E-17
	2	0.0005	6.57E-07	392	60.31	1.09E-08	1.11E-17
	3	-0.0008	-1.06E-06	-632	-97.23	1.09E-08	1.11E-17
	4	-0.0005	-6.58E-07	-415	-63.85	1.03E-08	1.05E-17
					Average:	**1.07E-08**	**1.09E-17**
19H-5, 99 horizontal	1	0.0008	1.19E-06	578	107.24	1.11E-08	1.13E-17
	2	0.0005	7.47E-07	353	65.49	1.14E-08	1.16E-17
	3	-0.0008	-1.20E-06	-582	-107.98	1.11E-08	1.13E-17
	4	-0.0005	-7.49E-07	-374	-69.39	1.08E-08	1.10E-17
					Average:	**1.11E-08**	**1.13E-17**
41X-6, 121 vertical	1	0.00001	1.44E-08	303	43.41	3.32E-10	3.39E-19
	2	0.00002	2.88E-08	587	84.10	3.42E-10	3.49E-19
	3	-0.00001	-1.44E-08	-251	-35.96	4.00E-10	4.08E-19
	4	-0.00002	-2.88E-08	-495	-70.92	4.06E-10	4.14E-19
					Average:	**3.70E-10**	**3.78E-19**
41X-6, 121 horizontal	1	0.00003	3.98E-08	200	63.49	6.27E-10	6.40E-19
	2	-0.00005	-6.63E-08	-304	-96.51	6.87E-10	7.01E-19
					Average:	**6.57E-10**	**6.70E-19**
49X-4, 51 vertical	1	0.00003	1.87E-08	470	66.86	2.79E-10	2.85E-19
	2	0.00001	6.21E-09	160	22.76	2.73E-10	2.79E-19
	3	-0.00003	-1.87E-08	-472	-67.14	2.78E-10	2.84E-19
	4	-0.00001	-6.23E-09	-157	-22.33	2.79E-10	2.85E-19
					Average:	**2.77E-10**	**2.83E-19**
49X-4, 51 horizontal	1	0.00005	6.26E-08	424	121.49	5.15E-10	5.26E-19
	2	0.00002	-2.50E-08	-176	-50.43	4.96E-10	5.06E-19
					Average:	**5.06E-10**	**5.16E-19**

Table A2. Critical values of the Pearson Product-moment correlation coefficient. ρ = Level of significance for two-tailed test. 0.05 = %95 confident level.

ρ	0.1	0.05	0.02	0.01	ρ	0.1	0.05	0.02	0.01
1	0.988	0.997	0.9995	0.9999	24	0.33	0.388	0.453	0.496
2	0.9	0.95	0.98	0.99	25	0.323	0.381	0.445	0.487
3	0.805	0.878	0.934	0.959	26	0.317	0.374	0.437	0.479
4	0.729	0.811	0.882	0.917	27	0.311	0.367	0.43	0.471
5	0.669	0.754	0.833	0.874	28	0.306	0.361	0.423	0.463
6	0.622	0.707	0.789	0.834	29	0.301	0.355	0.416	0.456
7	0.582	0.666	0.75	0.798	30	0.296	0.349	0.409	0.449
8	0.549	0.632	0.716	0.765	35	0.275	0.325	0.381	0.418
9	0.521	0.602	0.685	0.735	40	0.257	0.304	0.358	0.393
10	0.497	0.576	0.658	0.708	45	0.243	0.288	0.338	0.372
11	0.476	0.553	0.634	0.684	50	0.231	0.273	0.322	0.354
12	0.458	0.532	0.612	0.661	60	0.211	0.25	0.295	0.325
13	0.441	0.514	0.592	0.641	70	0.195	0.232	0.274	0.303
14	0.426	0.497	0.574	0.623	80	0.183	0.217	0.256	0.283
15	0.412	0.482	0.558	0.606	90	0.173	0.205	0.242	0.267
16	0.4	0.468	0.542	0.59	100	0.164	0.195	0.23	0.254
17	0.389	0.456	0.528	0.575					
18	0.378	0.444	0.516	0.561					
19	0.369	0.433	0.503	0.549					
20	0.36	0.423	0.492	0.537					
21	0.352	0.413	0.482	0.526					
22	0.344	0.404	0.472	0.515					
23	0.337	0.396	0.462	0.505					

REFERENCES CITED

Aidata, R. H., and Maltman, A. J., 2004, Data report: Initial permeability determinations on sediments from the Nankai Trough accretionary prism, ODP Sites 1173 and 1174, *in* Mikada, H., Moore, G. F., Taira, A., Becker, K., Moore, J. C., and Klaus, A., eds., Proceedings of the Ocean Drilling Program, Scientific Result, v. 190/196: College Station, Texas, Ocean Drilling Program, p. 1-12.

Anandarajah, A., and Kuganenthira, N., 1995, Some aspects of fabric anisotropy of soil: Geotechnique, v. 45, p. 69-81.

Ando, M., 1975, Source mechanisms and tectonics significance of historical earthquakes along the Nankai Trough, Japan: Tectonophysics, v. 27, p. 119-140.

Aoike, K., 1999, Tectonic evolution of the Izu collision zone: Research Report of the Kanagawa Prefectural Museum of Natural History, v. 9, p. 113-151.

Aplin, A. C., Matenaar, I. F., McCarty, D. K., and Van Der Pluijm, B. A., 2006, Influence of machanical compaction and clay mineral diadenesis on the microfabric and pore-scale properties of deep-water Gulf of Mexico mudstones: Clays and Clay Minerals, v. 54, no. 4, p. 500-514.

Bekins, B. A., McCaffrey, A. M., and Dreiss, S. J., 1995, Episodic and constant flow models for the origin of low-chloride waters in a modern accretionary complex: Water Resources Research, v. 31, no. 12, p. 3205-3215.

Bennett, R. H., Bryant, W. R., and Keller, G. H., 1977, Clay fabric and geotechinal properties of selected submarine sediments cores from the Mississippi Delta, Rockville, MD., U.S. Department of Commerce, National Oceanic and Atmospheric Administration, National Oceanic and Atmospheric Administration professional paper., v. 9, 86 p.:

Bennett, R. H., Fischer, K. M., Lavoie, D. L., Bryant, W. R., and Rezak, R., 1989, Porometry and fabric of marine clay and carbonate sediments:determination of permeability: Marine Geology, v. 89, p. 127-152.

Bennett, R. H., O'Brien, N. R., and Hulbert, M. H., 1991, Determinants of clay and shale microfabric signatures: Processes and mechanisms, *in* Bennett, R. H., Bryant, W. R., and Hulbert, M. H., eds., Microstructure of Fine-Grained Sediments: From Mud to Shale: New York, Springer-Verlag, p. 5-32.

Biscaye, P. E., 1965, Mineralogy and sedimentation of recent deep sea clays in the Atlantic Ocean and adjacent seas and oceans: Geological Society of America Bulletin, v. 76, p. 235-260.

Bolton, A. J., Maltman, A. J., and Clennel, M. B., 1998, The importance of overpressure timing and permeability evolution in fine-grained sediments undergoing shear: Journal of Structural Geology, v. 20, no. 8, p. 1013-1022.

Bolton, A. J., Maltman, A. J., and Fisher, Q., 2000, Anisotropic permeability and biomodal pore-size distributions of fine-grained marine sediments: Marine and Petroleum Geology, v. 17, p. 657-672.

Bourlange, S., Jonuiaux, L., and Henry, P., 2004, Data report: Permeability, compressibility, and friction coefficient measurements under confining pressure and strain, leg 190, Nankai Trough, *in* Mikada, H., Moore, G. F., Taira, A., Becker, K., Moore, J. C., and Klaus, A., eds., Proceedings of the Ocean Drilling

Program, Scientific Result, v. 190/196: College Station, Texas, Ocean Drilling Program, p. 1-16.
Brown, K. M., and Ransom, B., 1996, Porosity correction for smectite-rich sediments: impact on studies of compaction, fluid generation, and tectonic history: Geology, v. 24, p. 843-846.
Byrne, T., Maltman, A. J., Stephenson, E., Soh, W., and Knipe, R., 1993, Deformation structures and fluid flow in the toe region of the Nankai accretionary prism, *in* Hill, I., Taira, A., Firth, J., and the Leg 131 Scientists, eds., Proceedings of the Ocean Drilling Program, v. 131: College Station, TX., Ocean Drilling Program, p. 83-101.
Carson, B., and Screaton, E., 1998, Fluid flow in accretionary prisms:evidence for focused, time-variable discharge: Reviews of Geophysics, v. 36, p. 329-351.
Chamley, H., 1980, Clay sedimentation and paleoenvironment in the Shikoku Basin since the middle Miocene, *in* Klein, K., Kobayashi, K., and the Leg 58 Scientists, eds., Initial Reports of the Deep Sea Drilling Project, v. 58: Washington, DC., U.S. Government Printing Office, p. 669-678.
Chamley, H., and Cadet, J. P., 1986, Clay sedimentation and paleoenvironment in the Shikoku Basin since the middle Miocene, *in* Kagami, H., Karig, D. E., Coulbourn, W. E., and the leg 87 Scientists, eds., Initial Reports of the Deep Sea Drilling Project, v. 87: Washington, DC., U.S. Government Printing Office, p. 633-641.
Chamot-Rooke, N., Renard, V., and Le Pichon, X., 1987, Magnetic anomalies in the Shikoku basin: a new interpretation: Earth and Planet Science Letters, v. 83, p. 214-228.
Chiou, W. A., Bryant, W. R., and Bennett, R. H., 1991, Quantification of clay fabric: a simple technique, *in* Bennett, R. H., Bryant, W. R., and Hulbert, M. H., eds., Microstructure of fine-grained sediments: From mud to shale: New York, Springer-Verlag, p. 379-387.
Clennel, M. B., Dewhurst, D. N., Brown, K. M., and Westbrool, G. K., 1999, Permeability anisotropy of consolidated clays, *in* Aplin, A. C., Fleet, A. J., and Macquaker, J. H. S., eds., Muds and Mudstone:Physical and Fluid Flow Properties, v.158: London, Geological Society, London, Special Publication, p. 79-96.
Clift, P., and Vannucchi, P., 2004, Controls on tectonic accretion versus erosion in subduction zones: Implications for the origin and recycling of the continental crust: Reviews of Geophysics, v. 42, p. 1-31.
Colten-Bradley, V. A., 1987, Role of pressure in smectite dehydration-effects on geopressures and smectite to illite transformation.: The American Association of Petroleum Geologist Bulletin, v. 71, p. 1414-1427.
Cook, H. E., Johnson, P. D., Matti, J. C., and Zemmels, I., 1975a, Methods of sample preparation and X-ray diffraction data analysis, X-ray Mineralogy Laboratory, Deep Sea Drilling Project, University of California, Riverside, *in* Hayes, D. E., and Frakes, L. A., eds., Initial Reports of the Deep Sea Drilling Project, v.28: Washington, DC., U.S. Government Printing Office, p. 999-1007.
Cook, H. E., Zemmels, I., and Matti, J. C., 1975b, X-ray mineralogy data, far western Pacific, *in* Karig, D. E., Ingle, J. C., and the Leg 31 Scientists, eds., Initial Reports of the Deep Sea Drilling Project, v. 31: Washington, DC., U.S. Government

Printing Office, p. 883-895.
Dahlen, F. A., 1990, Critical taper model of fold-and-thrust belts and accretionary wedges: Annual Review of Earth and Planetary Sciences, v. 18, p. 55-99.
De Rosa, R., Zuffa, G. G., Taira, A., Leggett, J. K., 1986, Petrography of trench sands from the Nankai Trough, southwest Japan: Implications for long-distance turbidite transportation: Geological Magazine, v. 123, p. 477-486.
Dewhurst, D. N., Yang, Y., and Aplin, A. C., 1999, Permeability and fluid flow in natural mudstones, *in* Aplin, A. C., Fleet, A. J., and Macquaker, J. H. S., eds., Muds and Mudstones: Physical and Fluid-Flow Properties, v. 158: London Geological Society, London, Special Publication, p. 23-43.
Dungan, B., and Daigle, H., 2011, Data report: permeability, compressibility, stress state, and grain size of shallow sediments from Sites C0004, C0006, C0007, and C0008 of the Nankai accretionary complex, *in* Kinoshita, M., Tobin, H., Ashi, J., Kimura, G., Lallement, S., Screaton, E., Curewitz, D., Masago, H., Moe, K. T., and Scientist, t. E., eds., Proceeding of the Integrated Ocean Drilling Program, v. 314/315/316: Washington, DC., Integrated Ocean Drilling Program Management International, Inc., p. 1-11.
Expedition 316 Scientists, 2009a, Expedition 316 Site C0006, *in* Kinoshita, M., Tobin, H., Ashi, J., Kimura, G., Lallement, S., Screaton, E., Curewitz, D., Masago, H., Moe, K. T., and the Expedition 314/315/316 Scientists, eds., Proceedings of the Integrated Ocean Drilling Program, v. 314/315/316: Washington, DC., Integrated Ocean Drilling Program Management International, Inc., p. 1-29.
Expedition 316 Scientists, 2009b, Expedition 316 Site C0007, *in* Kinoshita, M., Tobin, H., Ashi, J., Kimura, G., Lallement, S., Screaton, E., Curewitz, D., Masago, H., Moe, K. T., and the Expedition 314/315/316 Scientists, eds., Proceedings of the Integrated Ocean Drilling Program, v. 314/315/316: Washington, DC., Integrated Ocean Drilling Program Management International, Inc., p. 1-110.
Expedition 316 Scientists, 2009c, Expedition 316 Site C0008, *in* Kinoshita, M., Tobin, H., Ashi, J., Kimura, G., Lallement, S., Screaton, E., Curewitz, D., Masago, H., Moe, K. T., and the Expedition 314/315/316 Scientists, eds., Proceedings of the Integrated Ocean Drilling Program, v. 314/315/316: Washington, DC., Integrated Ocean Drilling Program Management International, Inc., p. 1-107.
Expedition 316 Scientists, 2009d, Expediton 316 Site C0004, *in* Kinoshita, M., Tobin, H., Ashi, J., Kimura, G., Lallement, S., Screaton, E., Curewitz, D., Masago, H., Moe, K. T., and the Expedition 314/315/316 Scientists, eds., Proceedings of the Integrated Ocean Drilling Program, v. 314/315/316: Washington, DC., Integrated Ocean Drilling Program Management International, Inc., p. 1-107.
Expedition 316 Scientists, 2009e, Expedition 316 methods, *in* Kinoshita, M., Tobin, H., Ashi, J., Kimura, G., Lallement, S., Screaton, E., Curewitz, D., Masago, H., Moe, K. T., and the Expedition 314/315/316 Scientists, eds., Proceedings of the Integrated Ocean Drilling Program, v. 314/315/316: Washington, DC., Integrated Ocean Drilling Program Management International, Inc., p. 1-73.
Expedition 322 Scientists, 2010a, Expedition 322 Site C0011, *in* Saito, S., Underwood, M. B., Kubo, Y., and the Expedition 322 Scientists, eds., Proceedings of the Integrated Ocean Drilling Program, v. 322: Tokyo, Integrated Ocean Drilling Program Management International, Inc., p. 1-159.

Expedition 322 Scientists, 2010b, Expedition 322 Site C0012, *in* Saito, S., Underwood, M. B., Kubo, Y., and the Expedition 322 Scientists, eds., Proceedings of the Integrated Ocean Drilling Program, v. 322: Tokyo, Integrated Ocean Drilling Program Management International, Inc., p. 1-121.

Expedition 333 Scientists, 2011, NanTroSEIZE Stage 2: subduction inputs 2 and heat flow, *in* Henry, P., Kanamatsu, T., and Moe, K. T., eds., Integrated Ocean Drilling Program Preliminary Report, v. 333, Integrated Ocean Drilling Program Management International, Inc., p. 1-107.

Fagel, N., Luc, A., Chamley, H., Debrabant, P., and Jolivet, L., 1992, Clay sedimentation in the Sea of Japan since the early Miocene: influence of source-rock and hydrothermal activity: Sedimentary Geology, v. 80, no. 1-2, p. 27-40.

Fisher, A. T., and Underwood, M. B., 1995, Calibration of an X-ray diffraction method to determine relative mineral abundances in bulk powders using matrix singular value decomposition: a test from the Barbados accretionary complex, *in* Shipley, T. H., Ogawa, Y., and Blum, P., eds., Proceedings of the Ocean Drilling Program, Initial Reports, v. 156: College Station, TX., Ocean Drilling Program, p. 29-37.

Folk, R. L., and Ward, W. C., 1957, Brazos River bar, a study on the significance of grain size parameters: Journal of Sedimentary Petrology, v. 27, p. 3-27.

Friedman, G. M., 1958, Determination of sieve size distribution from thin section for sedimentary petrological studies: The Journal of Geology, v. 66, p. 349-416.

Gamage, K., and Screaton, E., 2003, Data Report: Permeabilities of Nankai Accretionary Prism Sediments, *in* Mikada, H., Moore, G. F., Taira, A., Becker, K., Moore, J. C., and Klaus, A., eds., Proceedings of the Ocean Drilling Program, Scientific Results, v. 190/196: Collage Station, TX, Ocean Drilling Program, p. 1-22.

Gamage, K., Screaton, E., Bekins, B. A., and Aiello, I., 2011, Permeability-porosity relationships of subduction zone sediments: Marine Geology, v. 279, p. 19-39.

Griffiths, J. C., 1967, Scientific Method in Analysis of Sediments, New York, NY., McGraw Hill, 508 p.

Guo, J., Likos, W. J., Underwood, M. B., Skarbek, R. M., Adamson, N., and Saffer, D. M., 2011, Data report: consolidation characteristics of sediments from Sites C0002, C0006, and C0007, IODP Expeditions 315 and 316, NanTroSEIZE Stage 1., *in* Kinoshita, M., Tobin, H., Ashi, J., Kimura, G., Lallement, S., Screaton, E., Curewitz, D., Masago, H., Moe, K. T., and the Expedition 314/315/316 Scientist, eds., Proceedings of the Integrated Ocean Drilling Program, v. 314/315/316: Washington, DC., Integrated Ocean Drilling Program Management Internationl, Inc.

Guo, J., and Underwood, M. B., 2011a, Data Report: Clay mineral assemblages from Nankai Trough and Kumano basin, IODP Expeditions 315 and 316, NanTroSEIZE Stage 1, *in* Kinoshita, M., Tobin, H., Ashi, J., Kimura, G., Lallement, S., Screaton, E., Curewitz, D., Masago, H., Moe, K. T., and the Expedition 314/315/316 Scientist, eds., Proceedings of the Integrated Ocean Drilling Program, v. 314/315/316: Washington, DC., Integrated Ocean Drilling Program Management International, Inc.

Guo, J., and Underwood, M. B., 2011b, Data report: refined method for calculating percentages of kaolinite and chlorite from X-ray diffraction data, with application to the Nankai margin of southwest Japan., *in* Kinoshita, M., Tobin, H., Ashi, J.,

Kimura, G., Lallement, S., Screaton, E., Curewitz, D., Masago, H., Moe, K. T., and the Expedition 314/315/316 Scientist, eds., Proceedings of the Integrated Ocean Drilling Program, v. 314/315/316: Washington, DC., Integrated Ocean Drilling Program Management International, Inc., p. 1-14.

Heath, G. R., and Pisias, N. G., 1979, A method for the quantitative estimation of clay minerals in North Pacific deep-sea sediments: Clays and Clay Minerals, v. 27, p. 175-184.

Hill, I. A., Taira, A, Firth, J. V., and Leg 131 Scientists, 1993, Scientific results, *in* Hill, I., Taira, A., Firth, J., and the Leg 131 Scientists, eds., Proceedings of the Ocean Drilling Program, v. 131: College Station, TX., Ocean Drilling Program, p. 331-341.

Hori, T., Kato, N., Hirahara, K., Baba, T., and Kaneda, Y., 2004, A numerical simulation of earthquake cycles along the Nankai Trough in southwest Japan: lateral veriation in frictional property due to the slab geometry control the nucleation position: Earth and Planetary Science Letters, v. 228, no. 3-4, p. 215-226.

Ichinose, G. A., Thio, H. K., Somerville, P. G., Sato, T., and Ishii, T., 2003, Rupture process of the 1944 Tonankai earthquake (M s 8.1) from the inversion of teleseismic and regional seismograms: Journal of Geophysical Research, v. 108.

Ike, T., Moore, G. F., Kuramoto, S., Park, J., Kaneda, Y., and Taira, A., 2008, Variations in sediment thickness and type along the northern Philippine Sea Plate at the Nankai Trough: Island Arc, v. 17, no. 3, p. 342-357.

Itoh, Y., and Nagasaki, Y., 1996, Crustal shortening of southwest Japan in the late Miocene: Island Arc, v. 5, p. 337-353.

Johnson, L. J., Chu, C. H., and Hussey, G. A., 1985, Quantitative clay mineral analysis using simultaneous linear equations.: Clays and Clay Minerals, v. 33, p. 107-117.

Kagami, H., Karig, D. E., Coulbourn, W. T., and the Leg 87 Scientists, 1986, Initial Reports of the Deep Sea Drilling Project, v. 87: Washington, U.S. Government Printing Office.

Kamata, H., and Kodama, K., 1999, Volcanic history and tectonics of the southwest Japan arc: Island Arc, v. 8, p. 393-403.

Karig, D. E., 1993, Reconsolidation tests and sonic velocity measurements of clay-rich sediments from the Nankai Trough., *in* Hill, I., Taira, A., Firth, J., and the Leg 131 Scientists, eds., Proceedings of the Ocean Drilling Program, v. 131: College Station, TX., Ocean Drilling Program, p. 247-260.

Kastner, M., Elderfield, H., Jenkins, W. J., Gieskes, J. M., and Gamo, T., 1993, Geochemical and isotopic evidence for fluid flow in the western Nankai subduction zone, Japan, *in* Hill, I., Taira, A., and Firth, J., eds., Proceedings of the Ocean Drilling Program, v. 131: College Station, TX, Ocean Drilling Program, p. 397-413.

Kim, J. W., Bryant, W. R., Watkins, J. S., and Tieh, T. T., 1999, Electron microscopic observation of shale diagenesis, offshore Louisiana, USA, Gulf of Mexico: Geo-Marine Letters, v. 18, no. 3, p. 234-240.

Kimura, G., Screaton, E., Curewitz, D., and the Expedition 316 Scientist, 2008, NanTroSEIZE Stage 1A: NanTroSEIZE shallow megasplay and frontal thrusts: Japanese Implementing Organization, Center for Deep Earth Exploration (CDEX), Japan Agency for Marine-Earth Science and Technology (JAMSTEC).

Kimura, G., Stern, R. J., and Yoshida, T., 2005, Reinitiation of subduction and magmatic responses in southwest Japan during Neogene time: Geological Society of America Bulletin, v. 117, p. 969-986.
Kobayashi, K., and Nakada, M., 1978, Magnetic anomalies and tectonic evolution of the Shikoku basin: Journal of Physics of the Earth, v. 26, p. 391-402.
Kopf, A., Strasser, M., Monsees, N., Underwood, M. B., and Guo, J., 2011, Data report:particle size analysis of sediments recovered during IODP Expeditions 315 and 316, Sites C0001-C0008, Nankai Trough forearc, off Japan, *in* Kinoshita, M., Tobin, H., Ashi, J., Kimura, G., Lallement, S., Screaton, E., Curewitz, D., Masago, H., Moe, K. T., and the Expedition 314/315/316 Scientist, eds., Proceedings of the Integrated Ocean Drilling Program, v. 314/315/316: Washington, DC., Integrated Ocean Drilling Program Management International, Inc., p. 1-19.
Krumbein, W. C., 1935, Thin-section mechanical analysis of indurated sediments: The Journal of Geology, v. 43, p. 482-496.
Lay, T., Kanamori, H., Ammon, C. J., Nettles, M., Ward, S. N., Aster, R. C., Beck, S. L., Brudzinski, M. R., Butler, R., DeShon, H. R., Ekstrom, G., Satake, K., and Sipkin, S., 2005, The great Sumatra-Andaman earthquake of 26 December 2004: Science, v. 308, no. 5725, p. 1127-1133.
Le Pichon, X., Henry, P., and Lallement, S., 1993, Accretion and erosion in subduction zones:The role of fluids: Annual Review of Earth and Planetary Sciences, v. 21, p. 307-338.
Ludwig, J., and Houtz, E. R., 1979, Isopach map of sediments in the Pacific Ocean basin and Marginal Sea basin: American Association of Petroleum Geologist Map Series, n. 64.
Marsaglia, K. M., Ingersoll, R. V., and Packer, B. M., 1992, Tectonic evolution of the Japanese Islands as reflected in modal compositions of Cenozoic forearc and backarc sand and sandstone: Tectonics, v. 11, no. 5, p. 1028-1044.
Martinez-Nistal, A., Veniale, F., Setti, M., and Cotecchia, F., 1991, A scanning electron microscopy image processing method for quantifying fabric orientation of clay geomaterials: Applied Clay Science, v. 14, p. 235-243.
McManus, D. A., 1991, Suggestions for authors whose manuscripts include quantitative clay mineral analysis by X-ray diffraction: Marine Geology, v. 98, p. 1-5.
Mikada, H., Becker, K., Moore, J. C., Klaus, A., and the Leg 196 Scientists, 2002, Proceedings of the Ocean Drilling Program, Initial Reports, v. 196: College Station, TX, Ocean Drilling Program.
Mitchell, J. K., 1993, Fundamentals of Soil Behavior, New York, Wiley.
Moon, C. F., and Hurst, C. W., 1984, Fabrics of muds and shales: an overview, in Stow, D. A. V., and Piper, D. J. W., eds., Fine-Grained Sediments: Deep Water Processes and Facies, v. 1984, Geological Society by Blackwell Scientific Publications, p. 579-593.
Moore, C. A., 1968, Quantitative analysis of naturally occurring multicomponent mineral systems by X-ray diffraction: Clays and Clay Minerals, v. 16, p. 325-336.
Moore, D. M., and Reynolds, R. C., Jr., 1989, X-ray Diffraction and the Identification and Analysis of Clay Minerals, Oxford, Oxford University Press.
Moore, G. F., Park, O. J., Bangs, N. L., Gullick, S. P., Tobin, H. J., Nakamura, Y., Sato,

S., Tsuji, T., Yoro, T., Tanaka, H., Uraki, S., Kido, Y., Sanada, Y., Kuramato, S., and Taira, A., 2009, Structural and seismic stratigraphic framework of the NanTroSEIZE Stage 1 transect, *in* Kinoshita, M., Tobin, H., Ashi, J., Kimura, G., Lallement, S., Screaton, E., Curewitz, D., Masago, H., Moe, K. T., and the Expedition 314/315/316 Scientists, eds., Proceedings of the Integrated Ocean Drilling Program, v. 314/315/316: Washington, DC., Integrated Ocean Drilling Program Management International, Inc., p. 1-46.

Moore, G. F., Taira, A., Klaus, A., and the Leg 190 Scientists, 2001, Proceedings of the Ocean Drilling Program, Initial Reports, v. 190: College Station, TX, Ocean Drilling Program.

Moore, J. C., 1989, Tectonics and hydrogeology of accretionary prisms: role of the décollement zone: Journal of Structural Geology, v. 11, no. 1-2, p. 95-106.

Moore, J. C., and Vrolijk, P., 1992, Fluids in accretionary prisms: Reviews of Geophysics, v. 30, p. 113-135.

Morgan, J. K., and Karig, D. E., 1993, Ductile strain in clay-rich sediments from Hole 808C:preliminary results using x-ray pole figure goniometry, *in* Taira, A., Firth, J., and Hill, I., eds., Proceedings of the Ocean Drilling Program Scientific Results, v. 131: College Station, TX, Ocean Drilling Program, p. 141-196.

Nemoto, K., Ishii, R., Daigo, R., and Asanuma, T., 1995, Sediment distribution of the Philippine Sea, in Tokuyama, H., Shcheka, S., Isezaki, N., eds., Geology and Geophysics of the Philippine Sea, Terra Scientific Publication Cooperation, Tokyo, p. 235-240.

Neuzil, C. E., 1994, How permeable are clays and shales: Water Resources Research, v. 30, p. 145-150.

Neuzil, C. E., 1995, Abnormal pressures as hydrodynamic phenomena: American Journal of Science, v. 295, p. 742-786.

Olsen, H. W., 1960, Hydraulic flow through saturated clays: Clays and Clay Minerals, v. 9, p. 131-161.

Orr, R. M., 1998, Clay mineralogy, diagenesis, and provence of sediments in the Nankai Trough, off Shikoku Island, southwest Japan [Master thesis]: Columbia, University of Missouri, 123 p.

Park, J. –O., Tsuru, T., Kodaira, S., Cummins, P. R., and Kaneda, Y., 2002, Splay fault branching along the Nankai subduction zone: Science, v. 297, p. 1157-1160.

Petschick, R., 2001, MacDiff software v. 4.2.5.

Pickering, K. T., Underwood, M. B., Taira, A., 1992, Open-ocean to trench turbidity-current flow in the Nankal Trough: Flow collapse and reflection: Geology, v. 20, p. 1099-1102.

Piper, D. J. W., von Huene, R., Duncan, J. R., 1973, Late Quaternary sedimentation in the active eastern Aleutian Trench: Geology, v. 1, p. 19-22.

Raleigh, C. B., Healy, J. H., and Bredehoeft, J. D., 1976, An experiment in earthquake control at Rangely, Colorado: Science, v. 191, p. 1230-1237.

Reuschle, T., 2011, Data report: permeability measurements under confining pressure, Expeditions 315 and 316, Nankai Trough., *in* Kinoshita, M., Tobin, H., Ashi, J., Kimura, G., Lallement, S., Screaton, E., Curewitz, D., Masago, H., Moe, K. T., and the Expedition 314/315/316 Scientist, eds., Proceedings of the Integrated Ocean Drilling Program, v. 314/315/316: Washington, DC., Integrated Ocean

Drilling Program Management Internation Inc. p. 1-17.
Rowe, K., Screaton, E., Guo, J., and Underwood, M. B., 2011, Data report: permeabilities of sediments from the Kumano Basin transect off Kii Peninsula, Japan, *in* Kinoshita, M., Tobin, H., Ashi, J., Kimura, G., Lallement, S., Screaton, E., Curewitz, D., Masago, H., Moe, K. T., and the Expedition 314/315/316 Scientist, eds., Proceedings of the Integrated Ocean Drilling Program, v. 314/315/316: Washington, DC., Integrated Ocean Drilling Program Management Internation Inc., p. 1-24.
Saffer, D. M., 2010, Hydrostratigraphy as a control on subduction zone mechanics through its effects on drainage:an example from the Nankai Margin, SW Japan: Geofluids, v. 10, p. 114-131.
Saffer, D. M., and Bekins, B. A., 2002, Hydrologic controls on the morphology and mechanics of accretionary wedges: Geology, v. 30, no. 3, p. 271-274.
Saffer, D. M., and Bekins, B. A., 2006, An evaluation of factors influencing pore pressure in accretionary complexes: Implications for taper angle and wedge mechanics: Journal of Geophysical Research, v. 111, p. 101-121.
Saffer, D. M., Guo, J., Underwood, M. B., Likos, W. J., Skarbek, R. M., Song, I., and Gildow, M., 2011, Data report:consolidation, permeability, and fabric of sediments from the Nankai continental slope, IODP Sites C0001, C0008, and C0004, *in* Kinoshita, M., Tobin, H., Ashi, J., Kimura, G., Lallement, S., Screaton, E., Curewitz, D., Masago, H., Moe, K. T., and the Expedition 314/315/316 Scientist, eds., Proceedings of the Integrated Ocean Drilling Program, v. 314/315/316: Washington, DC., Integrated Ocean Drilling Program Management International, Inc., p. 1-61.
Saffer, D. M., and Tobin, H. J., 2011, Hydrogeology and mechanics of subduction zone forearcs: Fluid flow and pore pressure: Annual Review of Earth and Planetary Sciences, v. 39, p. 157-186.
Saffer, D. M., Underwood, M. B., and McKiernan, A. W., 2008, Evaluation of factors controlling smectite transformation and fluid production in subduction zones: Application to the Nankai Trough: Island Arc, v. 17, no. 2, p. 208-230.
Schwartz, F. W., and Zhang, H., 2003, Fundamentals of Ground Water, New York, John Wiley & Sons, 592 p.
Screaton, E., Kimura, G., Curewitz, D., and the Expedition 316 Scientists, 2009, Expedition 316 Summary, *in* Kinoshita, M., Tobin, H., Ashi, J., Kimura, G., Lallement, S., Screaton, E., Curewitz, D., Masago, H., Moe, K. T., and the Expedition 316 Scientists, eds., Proceedings of the Integrated Ocean Drilling Program, v. 314/315/316: Washington, DC., Integrated Ocean Drilling Program Management International, Inc., p. 1-29.
Seno, T., 1977, The instantaneous rotation vector of the Philippine Sea Plate relative to the Eurasian Plate: Tectonophysics, v. 42, p. 209-226.
Seno, T., Stein, S., and Gripp, A. E., 1993, A model for motion of the Philippine Sea plate consisten with NUVEL-1 and geological data: Journal of Geophysical Research, v. 89, p. 941-948.
Shimamura, K., 1989, Topography and sedimentary facies of the Nankal deep sea channel, *in* Taira, A., Masuda, E., Sedimentary facies in the active plate margin: Tokyo, Terra Scientific Publication Cooperation, p. 529-556.

Simpson, D. H., 2009, Formation of accretionary prisms influenced by sediment subduction and supplied by sediments from adjacent continents: Geology, v. 38, p. 131-134.
Sintubin, M., 1994, Clay fabrics in relation to the burial history of shales: Sedimentology, v. 41, p. 1161-1169.
Shih, T. C., 1980, Magnetic lineation in the Shikoku basin, *in* Klein, G.de V., and Kobayashi, K., eds., Initial Reports of the Deep Sea Drilling Project, v. 58: Washington, DC., United States Government Printing Office, p. 783-788.
Spinelli, G. A., Mozley, P. S., Tobin, H. J., Underwood, M. B., Hoffman, N. W., Bellew, G. M., 2007, Diagenetic control of sediment strength and pore collapse in sediment approaching the Nankai Trough subduction zone: Geological Society of America Bulletin, v. 119, p. 377-390.
Spinelli, G. A., Giam balvo, E. R., and Fisher, A. T., 2004, Sediment permeability, distribution, and influence on fluxes, in oceanic basement, in Davis, E. E., Elderfield, H., eds., Hydrogeology of the Oceanic Lithosphere, Cambridge University Press, London, p. 151-188.
Strasser, M., Moore, G. F., Kimura, G., Kitamura, Y., Kopf, A. J., Lallemant, S., Park, J.-O., Screaton, E.J., Su, X., Underwood, M.B., and Zhao, X., 2009. Origin and evolution of a splay fault in the Nankai accretionary wedge: National Geosecience, v. 29, p. 648–652.
Streurer, J. F., and Underwood, M. B., 2003, Clay mineralogy of mudstones form the Nankai Trough reference Site 1173 and 1177 and frontal accretionary prism Site 1174., *in* Mikada, H., Moore, G. F., Taira, A., Becker, K., Moore, J. C., and Klaus, A., eds., Proceedings of the Ocean Drilling Program, Scientific Results, v. 190/196: College Station, TX., Ocean Drilling Program, p. 1-37.
Taira, A., and Niitsuma, N., 1986, Turbidite sedimentation in the Nankai Trough as interpreted from magnetic fabric, grain size, and detrital modal analyses, *in* Kagami, H., Karig, D. E., and Coulbourn, W. E., eds., Initial Reports of Deep Sea Drilling Project, v. 87: Washington, DC., U.S. Government Printing Office, p. 611-632.
Taira, A., 2001, Tectonic evolution of the Japanese Island arc system: Annual Review of Earth and Planetary Science, v. 29, p. 109-134.
Taira, A., Hill, I., Firth, J., and Leg 131 Scientists, eds., 1991, Site 808, *in* Taira, A., Hill, I., Firth, J., and Leg 131 Scientists, eds., Proceedings of the Ocean Drilling Program, Initial Reports, v. 131, College Station, TX, Ocean Drilling Program, p. 71-269.
Taylor, E., and Fisher, A. T., 1993, Sediment permeability at the Nankai accretionary prism, Site 808, *in* Hill, I., Taira, A., Firth, J., and the Leg 131 Scientists, eds., Proceedings of the Ocean Drilling Program, v. 131: College Station, TX., Ocean Drilling Program, p. 235-245.
Tobin, H., Kinoshita, M., Ashi, J., Lallement, S., Kimura, G., Screaton, E. J., Moe, K. T., Masago, H., Curewitz, D., and Scientists, T. E., 2009, NanTroSEIZE Stage 1 expeditions: Introduction and synthesis of key results, *in* Tobin, H., Kinoshita, M., Ashi, J., Lallement, S., Kimura, G., Screaton, E. J., Moe, K. T., Masago, H., Curewitz, D., and Scientists, T. E., eds., Proceedings of the Integrated Ocean Drilling Program, v. 314/315/316: Washington, DC, Integrated Ocean Drilling

Program Management International, Inc.
Underwood, M. B., 2007, Sediment inputs to subduction zones: Why lithostratigraphy and clay mineralogy matter, *in* Dixon, T. H., and Moore, J. C., eds., The seismogenic zone of subduction thrust faults: New York, Columbia University Press, p. 42-85.
Underwood, M. B., Basu, N., Streurer, J. F., and Udas, S., 2003, Data Report: Normalization factors for semiquantitative X-ray diffraction analysis, with application to DSDP Site 297, Shikoku Basin, *in* Mikada, H., Moore, G. F., Taira, A., Becker, K., Moore, J. C., and Klaus, A., eds., Proceedings of the Ocean Drilling Program, Scientific Results, v. 190/196: College Station, TX., Ocean Drilling Program, p. 1-28.
Underwood, M. B., and Guo, J., 2011, Data Report: Clay mineral assemblages in the Shikoku basin, NanTroSEIZE Subduction 1 inputs, the IODP Sites C0011 and C0012, *in* Saito, S., Underwood, M. B., Kubo, Y., and the Expedition 322 Scientists, eds., Proceedings of the Integrated Ocean Drilling Program, v. 322, (in press).
Underwood, M. B., Orr, R., Pickering, K., and Taira, A., 1993a, Provenance and dispersal patterns of sediments in the turbidite wedge of Nankai Trough, *in* Hill, I., Taira, A., Firth, J., and Scientists, t. L., eds., Proceedings of the Ocean Drilling Program, v. 131: College Station, TX, Ocean Drilling Program, p. 15-34.
Underwood, M. B., Pickering, K., Gieskes, J. M., Kastner, M., and Orr, R., 1993b, Sediment geochemistry, clay mineralogy, and diagenesis: a synthesis of data from Leg 131, Nankai Trough, *in* Hill, I., Taira, A., Firth, J., and the leg 131 Scientists, eds., Proceedings of the Ocean Drilling Program Scientific Results, v. 131: College Station, TX., Ocean Drilling Program, p. 343-363.
Underwood, M. B., Pickering, K., 1996, Clay-mineral provenance, sediment dispersal patterns and mudrock diagenesis in the Nankai Accretionary prism, southwest Japan: Clays and Clay Minerals, v. 44, p. 339-356.
Underwood, M. B., Saito, S., Kubo, Y., and the Expedition 322 Scientists, 2010, Expedition 322 Summary, *in* Saito, S., Underwood, M. B., Kubo, Y., and the Expedition 322 Scientists, eds., Proceedings of the Integrated Ocean Drilling Program, v. 322: Tokyo, Integrated Ocean Drilling Program, p. 1-60.
Underwood, M. B., and Streurer, J. F., 2003, Composition and sources of clay from the trench slope and shallow accretionary prism of Nankai Trough, *in* Mikada, H., Moore, G. F., Taira, A., Becker, K., Moore, J. C., and Klaus, A., eds., Proceedings of the Ocean Drilling Program, Scientific Results, v. 190/196: College Station, TX., Ocean Drilling Program, p. 1-28.
van der Plas, L., 1962, Preliminary note on the granulometric analysis of sedimentary rock: Sedimentology, v. 1, p. 145-157.
Whitehouse, U. G., Jeffrey, L. M., and Debbrecht, J. D., 1958, Differential settling tendencies of clay minerals in saline waters: Clays and Clay Minerals, v. 7, no. 1, p. 1-79.
Yang, Y., Aplin, A., 2007, Permeability and petrophysical properties of 30 natural mudstones: Journal of Geophysical Research, v. 112, p. 1-14.
Yue, L., Likos, W. J., Guo, J., and Underwood, M. B., 2012, Data report: permeability of mud(stone) samples from Site C0001, IODP Expedition 315, Nankai Trough:

NanTroSEIZE Stage 1, *in* Kinoshita, M., Tobin, H., Ashi, J., Kimura, G., Lallement, S., Screaton, E., Curewitz, D., Masago, H., Moe, K. T., and the Expedition 314/315/316 Scientist, eds., Proceedings of the Integrated Ocean Drilling Program, v. 314/315/316: Washington, DC., Integrated Ocean Drilling Program Management International, Inc., p. 1-41.

Zaniewski, K., and van der Meer, J. M., 2005, Quantification of plasmic fabric through image analysis: Catena, v. 63, p. 109-127.